NEW METHODS FOR INVESTIGATION OF SURFACE PASSIVATION LAYERS FOR CRYSTALLINE SILICON SOLAR CELLS

by

Halvard Haug

Thesis submitted in partial fulfillment
for the degree of Philosophiae Doctor

Department of Physics
Faculty of Mathematics and Natural Sciences
University of Oslo
March, 2014

Series of dissertations submitted to the
Faculty of Mathematics and Natural Sciences, University of Oslo
No. 1503

ISSN 1501-7710

Cover: Inger Sandved Anfinsen.
Printed in Norway: AIT Oslo AS.

Produced in co-operation with Akademika Publishing.
The thesis is produced by Akademika Publishing merely in connection with the thesis defence. Kindly direct all inquiries regarding the thesis to the copyright holder or the unit which grants the doctorate.

When there is a huge solar energy spill, it's just called a "nice day".

(Billboard from VoteSolar.org)

ABSTRACT

One of the main challenges of the c-Si PV industry is the implementation of high quality surface passivation layers. Effective surface passivation is needed in order to avoid large efficiency losses when moving towards thinner silicon wafers and to utilize the full potential of high quality Si material. To obtain a fundamental understanding of the surface recombination mechanisms and their impact on device performance, precise characterization methods and suitable physical models are of high importance.

The main result of this work is the development of a new method for analyzing surface recombination for passivated Si substrates under varying surface band bending conditions: A photoluminescence imaging setup is used to measure the effective minority carrier lifetime of passivated Si wafers while applying an external bias to a metal electrode deposited onto the rear side passivation layer. The experimental measurements have been analyzed using an extended Shockley Read-Hall model with added recombination in the space charge region. This approach is shown to give valuable information about the passivation mechanisms. The measured data can be used to independently determine the fixed charge density under illumination (field-effect passivation) and the surface recombination velocity parameters for electrons and holes (chemical passivation) for a wide range of dielectric passivation layers. The results are in good agreement with both capacitance-voltage measurements and lifetime measurements after deposition of corona charges on the sample surface.

A second major contribution from this work is the development of a modified version of the widely used simulation tool PC1D which runs from a command line, thus allowing for scripted simulations. This modified version of the program has also been used as a basis for a new user interface, which allows for improved visualization, multivariable analysis, optimization, fitting to experimental data and implementation of additional models.

Through this work, several passivation processes have been developed and optimized, and excellent passivation quality has been demonstrated for a stack of a-Si:H and a-SiN_x:H deposited by plasma enhanced chemical vapor deposition. Selected passivation layers have also been demonstrated as rear side passivation in a co-planar solar cell test structure with local rear contacts.

ACKNOWLEDGEMENTS

First and foremost I would like to thank my supervisors, Erik Stensrud Marstein, Ørnulf Nordseth and Edouard Monakhov. Erik, you have been a great main supervisor. Thank you for bringing me into the exciting field of silicon solar cells and for many good scientific discussions over the last years. You really have a gift for engaging people and for reminding us all about the importance of what we are trying to accomplish. I always leave your office with high spirits.

Ørnulf, I very much appreciate your excellent help over the last years. Thank you for teaching me about all kinds of equipment, supplying me with wafers, fixing instruments when I break them and giving me precise and good feedback on my writing. Your patience and cut-to-the-chase attitude have helped me a lot, and I would have needed to work a lot harder to accomplish this without you.

Edouard, you are a great resource with deep knowledge in anything related to semiconductors and characterization, and I probably should have used your knowledge even more. Even though we work at slightly different locations, I feel that our collaboration has been good, and I hope to continue this in the future.

I feel very privileged to have had the opportunity to work with all the smart, resourceful and generally nice people in the solar energy group at IFE, many of which I now consider to be my friends. I want to thank each and every one of you for helping and inspiring me multiple times during my work with this PhD. I am particularly grateful to Jo Gjessing for helping me with anything optics related, Marie Syre Wiig and Chang Chuan You for your processing skills, Josefine Selj for help with ellipsometry and Birger Retterstøl Olaisen for teaching me C++.

Most of my time at IFE has been spent with two different, yet both excellent, office roommates. I therefore want to thank Hallvard Angelskår and Tine Uberg Nærland for brightening up my daily life, helping me out with all kinds of things and for driving me home to Oslo countless times.

A special thanks goes to Jostein Thorstensen for a lot of fruitful collaboration in the lab, great scientific (or just silly) discussions and for valuable help proof-reading my thesis.

Finally, I want to thank my wonderful wife, sweetheart and best friend Kristine. Thanks for all your support at home, and for repeatedly hitting me over the head with different pieces of clothing each time I stopped writing on my dissertation. This would probably be possible without you, but I would have needed a lot more time. Thank you.

TABLE OF CONTENTS

CHAPTER 1
INTRODUCTION

Solar energy is the ultimate source of power. It is freely available over the entire globe and so abundant that the amount of solar radiation the earth receives in just 1 hour is enough to cover the entire annual human energy consumption. The most elegant way of utilizing the energy from the sun is the photovoltaic (PV) effect; photovoltaic solar cells can convert sunlight directly into electricity. For a long time, electricity production from photovoltaic solar cells was limited to space applications, small off-grid locations and low-power electronic devices due to high cost. The PV industry has however gone through a considerable growth over the last decade, and PV is currently the fastest growing renewable energy source, with an average growth rate of above 40 % per year between 2000 and 2012 [1]. It is therefore safe to say that the PV industry is now on its way to become a noticeable and significant player in the global energy market.

The technology which currently gives the lowest solar electricity cost, measured in dollars per watt at peak production ($\$/W_p$), is based on crystalline Si (c-Si) wafers. c-Si solar modules therefore dominate the PV market (currently with a share of 85-90 % [2]), and will be the most important solar cell technology in years to come. Figure 1.1 shows the learning curve for the c-Si PV industry from 1976 to 2012. In 2012, the world's total installed PV capacity surpassed 100 GW, with over 31 GW installed in 2012 alone. This large increase in production volume is linked to a very large price reduction, with the learning curve showing a 21 % reduction in module prices per doubling of cumulative production. Until now this has been made possible by large and focused research effort and, more importantly, long-term government incentives in key markets.

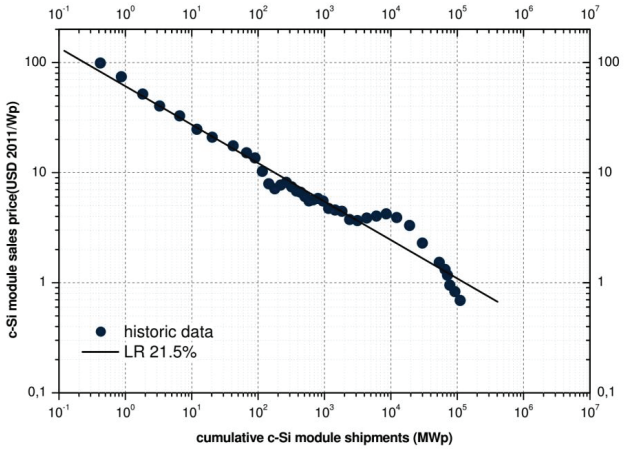

Figure 1.1. Learning curve for the c-Si PV industry, showing module prices as a function of cumulative PV module shipments. From ITRPV report 2013 [3]. (Copyright 2012-, © Semiconductor Equipment and Materials International. All rights reserved.)

The trend in price reductions in terms of $\$/W_p$, however, has to be continued as incentives are continuously being reduced. The two major prerequisites for a further increase in PV growth are increased solar cell efficiency and reduced production cost. The Si wafer accounts for approximately 60% of the cell cost today [3], and reduction of the wafer thickness is therefore necessary for further cost reduction. Figure 1.2 shows the predicted trend for Si wafer thickness in industrial scale production, which is expected to be reduced to 120 µm by 2020. This reduction in wafer thickness must be accomplished while simultaneously maintaining, and preferably increasing, cell efficiency.

One of the most important reasons for efficiency loss in solar cells is the incomplete collection of excited electrons within the cell, a process referred to as carrier recombination. A large part of this recombination occurs at the wafer surfaces (typically quantified by the surface recombination velocity (SRV)), and this source of efficiency loss becomes more significant as the wafer thickness is decreased. Figure 3 shows a color map of the solar cell efficiency as a function of wafer thickness and rear SRV. As seen from the figure, high solar cell efficiencies are possible for thinner wafers, but with stronger requirements on the surface quality.

Minimization of the surface recombination losses is known as surface passivation. Even though different passivation schemes has been used in laboratory scale solar cells for many years, (e.g. for the 25 % record efficiency obtained by the PERL cell in the 1990's [4]), rear side surface passivation layers has only been implemented in a few high-efficiency cell concepts in industrial production. In the latest years however, many large companies have

demonstrated high efficiency cells incorporating rear side passivation layers, with reported conversion efficiencies commonly exceeding 20%. There is currently a large research activity in this field, and the development of high quality and industrially relevant passivation processes is one of the most important technological challenges that needs to be addressed in the solar cell industry today.

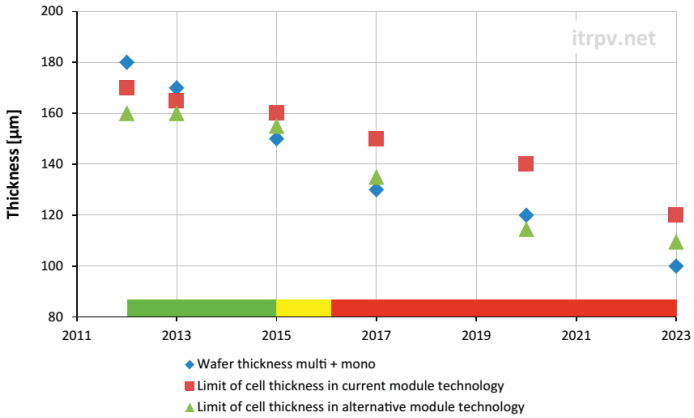

Figure 1.2. Predicted trend for minimum as-cut wafer thickness in mass production of solar cells. From International Technology Roadmap of PV, 2012 [3]. (Copyright 2012-, © Semiconductor Equipment and Materials International. All rights reserved.)

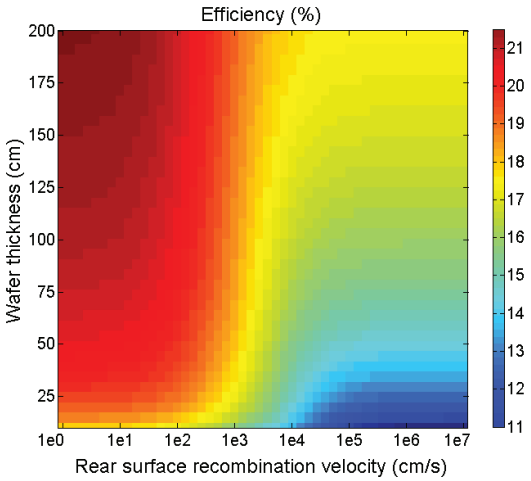

Figure 1.3. Color map showing the conversion efficiency of a Si solar cell as a function of the rear side surface recombination velocity (x-axis) and the wafer thickness (y-axis). The image consist of 2500 PC1D simulations, created using the PC1D for Matlab program which has been developed in this work (see Paper IV for details).

1.1 MOTIVATION AND SCOPE

The external motivation for this work can be summarized from the above: The world needs clean energy, and Si solar cells have the potential of making this possible. With the ongoing reduction of wafer thickness, reduction of surface recombination is an important technological challenge that has to be solved. It was however not straightforward finding out how to narrow down and focus my effort within this field. How could I make a valuable scientific and technological contribution?

When working with this PhD, I quickly discovered that surface passivation is not a field of research that is very well-defined or easily reproduced. The passivation quality is highly process dependent and is influenced by many factors including the type of wafer, cleanliness of chemical baths, timing, handling, etc. Even when all these factors are the same, passivation results reported in the literature are not generally transferable between deposition systems, even for groups using similar equipment

Numerous studies have been published in the last years on the surface passivation quality of passivation layers for various deposition conditions. I therefore wanted to go one step further from comparing our process optimization to that of others. It seemed to me that the most fruitful road ahead was to find a precise and practical way of obtaining a fundamental understanding of any specific passivation layer in question. If I could contribute to our understanding of passivation layers in terms of a few key parameters, this knowledge would be transferable to other research groups, like good research should be. For this reason my work gradually turned towards characterization and development of new characterization methods. The first main topic of this thesis is characterization and development of new characterization methods for passivation layers on c-Si.

For the same reason I have also spent much time doing computer simulations, trying to fit different models to my experimental data. These simulations constitute the second main topic of this thesis. Writing my own implementation of existing physical models and working on the development of good simulation tools, forced me to think about the physical processes behind surface recombination. This part of the thesis can also easily be picked up by other researchers. I hope that I in this way have succeeded in making a small contribution to the renewable energy future and to the continuous growth of PV technology.

1.2 STRUCTURE OF THE THESIS

This thesis is written as a collection of papers, which are appended at the end of the thesis. The purpose of the main text is to provide the reader with the necessary theoretical background and experimental details for the work, and to link the individual papers together. Most of the scientific results are already presented in the papers and will not be repeated to any length in the main text.

The thesis is divided into 7 chapters. In Chapter 1 (the present chapter) the work is placed into a broader context, and a short motivation for the work is given. The chapter ends with a summary of the papers, including a specification of my contribution to each one.

Chapter 2 is meant to provide the reader with the theoretical background necessary to follow the discussion in later chapters. The chapter contains theory of bulk and surface recombination and definition of important concepts like the surface recombination velocity and the effective lifetime. The last section of the chapter gives a brief review of different passivation materials used for Si solar cells.

Chapter 3 describes the simulations and the implementation of the physical models and equations described in Chapter 2, and presents simulation results which serve to illustrate the different aspects of surface recombination. It also contains a description of the command line version of PC1D and a new user interface developed within this work and presents simulations of subsurface recombination using this software.

Chapter 4 describes the different techniques used for sample processing and characterization in this work. The last section of the chapter presents PECVD processing parameters for different materials and measured key properties of these layers.

Chapter 5 introduces the new characterization technique developed in this work, where a metal electrode is used to modulate the rear side SRV, which is measured in a photoluminescence imaging setup (PL-V). Advantages and limitations of the method and various experimental considerations are discussed. The chapter ends with a selection of results measured on different passivation materials together with an interpretation of these results using the model described in Chapter 3.

Chapter 6 presents suggestions for further work and some preliminary results. The passivation layers and stacks described in Chapter 4 are implemented into a co-planar solar cell test structure, and selected solar cell results are presented, illustrating the influence of the rear side SRV on the measured efficiency.

In Chapter 7 concluding remarks on the main results and a brief summary of the thesis as a whole is given.

1.3 SUMMARY OF PAPERS

This section presents a summary of the included papers. The papers are attached in chronological order at the end of the thesis.

PAPER I

H. Haug, Ø. Nordseth, E. V. Monakhov, and E. S. Marstein, "Photoluminescence imaging under applied bias for characterization of Si surface passivation layers," Sol. Energy Mater. Sol. Cells, vol. 106, pp. 60–65, Jun. 2012.

In this paper we for the first time present the photoluminescence imaging under applied bias (PL-V) method for characterization of dielectric surface passivation layers. PL–V measurements were performed on p-type and n-type Si wafers passivated by PECVD a-SiN_x:H layers, and the results were interpreted both by using the extended SRH model and PC1D simulations. From this analysis we could independently extract the important parameters S_{n0}, S_{p0} and Q_f. The best-fit Q_f values under illumination were found to be in good agreement with values obtained by dark C–V measurements.

This paper was primarily carried out by the candidate alone, including sample processing, characterization and analysis. The paper was written by the candidate, but with several important remarks from all the co-authors.

The manuscript was submitted as a conference contribution to the 2nd International Conference on Crystalline Silicon Photovoltaics (SiliconPV) in Leuven, and was presented by the candidate as an oral presentation. Being part of the 20 best papers of the conference (ranked #7), the final version of the paper was published as a journal article in Solar Energy Materials and Solar Cells.

PAPER II

H. Haug, S. Olibet, O. Nordseth, and E. Stensrud Marstein, "Modulating the field-effect passivation at the SiO_2/c-Si interface: Analysis and verification of the photoluminescence imaging under applied bias method," J. Appl. Phys., vol. 114, no. 17, p. 174502, Nov. 2013.

In this paper we performed an in-depth analysis of the PL-V method published in Paper I, discussing various aspects of the technique and possible errors in the determination of the rear SRV. PL-V measurements of thermally oxidized Si wafers were verified against corresponding results from QSS-μPCD measurements after depositing corona charges. We found an excellent agreement between the two techniques and also with C-V measurements

of the fixed charge density. The PL-V method has thus been shown to be a powerful tool for quantitative, fundamental investigations of c-Si passivation layers.

The experimental work, simulations and writing of the paper was primarily carried out by the candidate, with the exception of the corona charging and QSS-μPCD experiments and the corresponding description in the paper, which was done by Dr. Sara Olibet at ISC Konstanz. Important comments and manuscript feedback were supplied by all co-authors.

PAPER III

H. Haug, O. Nordseth, E. Monakhov, and E. S. Marstein, "Investigation of Carrier Recombination at the SiO2/c-Si Interface by Photoluminescence Imaging Under Applied Bias," IEEE Journal of Photovoltaics., vol. 4, no. 1, pp. 374–379, 2014.

In this paper we used the PL-V method for more in-depth measurements of the recombination at the SiO_2/c-Si interface under various band bending conditions. Both the effect of substrate doping polarity and post-oxidation forming gas anneal (FGA) was investigated. Again the measured data were interpreted in the framework of the extended Shockley-Read-Hall theory. The extracted Q_f values were found to decrease from 7×10^{11} cm^{-2} to 4×10^{11} cm^{-2} after the FGA, whereas the S_{0n} and S_{0p} parameters decreased for both substrate types, causing a total decrease in the SRV. To correctly model the experimental results we found that it was necessary to add an additional contribution to the effective SRV.

The work was primarily carried out by the candidate alone. The paper was written by the candidate, but with several important remarks from all the co-authors.

The abstract for this paper was submitted as a conference contribution to the 39th IEEE Photovoltaic Specialists Conference in Tampa, and was presented by the candidate as an oral presentation. It was also selected as one of the contributions worthy of a direct publication as a journal article in the IEEE Journal of Photovoltaics.

PAPER IV

H. Haug, S. Helland, Ø. Nordseth, E. V. Monakhov, and E. S. Marstein, "Analysis of a-SiN_x:H passivated Si surfaces based on injection level dependent lifetime and capacitance/conductance-voltage measurements," in Proceedings of the 26th European Photovoltaic Solar Energy Conference and Exhibition, Hamburg, Germany 2011, pp. 1524–1529

In this first paper we published a study of our PECVD a-SiN_x:H process, investigating how the surface passivation quality, composition and optical properties of a-SiN_x:H layers are affected by the gas flow ratio during deposition. Due to leakage currents and hysteresis

effects, it is inherently difficult to analyze Si-rich a-SiN_x:H passivation layers using electrical characterization. We demonstrated how analysis of the injection level-dependent effective SRV may be employed as a valuable, complementary tool for interpreting trends in the surface recombination mechanisms.

The paper was written by the candidate, but with important remarks from the other co-authors. Experiment planning, sample processing, and analysis of the carrier lifetime data were also primarily carried out by the candidate, whereas the electrical characterization and analysis were performed by M.Sc. student Susanne Helland.

The paper was presented by the candidate as a poster at the 26th European Photovoltaic Solar Energy Conference (EUPVSEC) in Hamburg.

PAPER V

H. Haug, J. H. Selj, Ø. Nordseth, and E. S. Marstein, "Optimization of a-SiO_x/a-SiN_x double layer antireflection coatings for silicon solar cells," in Proceedings of the 27th European Photovoltaic Solar Energy Conference and Exhibition, Frankfurt, Germany, 2012, pp. 1376–1378.

In this paper we performed an optimization of single- and double layer ARCs for silicon solar cells. The optical properties of various PECVD a-SiN_x:H and a-SiO_xN_y:H monolayers were measured by spectroscopic ellipsometry. Double layer ARCs were then designed by optimizing the thickness and composition of the layers with respect to the photogenerated current. We found that the relative photocurrent improvement when changing from a single layer ARC to a double layer ARC is relatively low for moderately absorbing layers. The improvement however would be significantly increased by a reduction of the extinction coefficient in the high-index layers.

This work was primarily carried out by the candidate alone, with the exception of analysis of ellipsometric data, which were performed by Dr. Josefine Selj. The manuscript was written by the candidate, but with several important remarks from all the co-authors.

The paper was presented by the candidate as a poster at the 27th European Photovoltaic Solar Energy Conference (EUPVSEC) in Frankfurt.

PAPER VI

H. Haug, B. R. Olaisen, Ø. Nordseth, and E. S. Marstein, "A Graphical User Interface for Multivariable Analysis of Silicon Solar Cells Using Scripted PC1D Simulations," Energy Procedia, vol. 38, pp. 72–79, 2013.

In this paper we presented a modification of the commonly used simulation program PC1D which can be run from a command line. We also presented a new graphical user interface for the program, which includes many new features for multivariable analysis, advanced plotting, optimization, fitting to experimental data and implementing additional models and parameters not available in the original PC1D program. Several simulation examples were presented to illustrate the capabilities of the new program.

The command line version of PC1D was developed by Birger R. Olaisen, and the upgraded user interface was developed by the candidate. The simulations and writing of the manuscript was performed by the candidate, with important remarks from the co-authors.

The paper was presented by the candidate as an oral presentation at the 3rd International Conference on Crystalline Silicon Photovoltaics (SiliconPV) in Hamelin.

RELEVANT CO-AUTHORSHIPS

- *T. U. Nærland, H. Haug, H. Angelskår, R. Søndenå, E. S. Marstein, and L. Arnberg, "Studying Light-Induced Degradation by Lifetime Decay Analysis: Excellent Fit to Solution of Simple Second-Order Rate Equation," IEEE J. Photovoltaics, vol. 3, no. 4, pp. 1265–1270, Oct. 2013.*

- *F. Kløw, H. Haug, and S. E. Foss, "Surface Recombination Velocity Measurements of Metallized Surfaces by Photoluminescence Imaging," Energy Procedia, vol. 43, pp. 18–26, 2013.*

- *E. S. Marstein, H. Haug, T. U. Nærland, H. Angelskår, and R. Søndenå, "Advanced photoluminescence imaging-based characterization methods," in Proceedings of the 28th European Photovoltaic Solar Energy Conference and Exhibition, Paris, France, 2013, pp. 1618–1621.*

- *E. S. Marstein, J. H. Selj, J. Gjessing, H. Haug, and A. Sudbø, "Light management in thin crystalline silicon solar cells.," in Proceedings of the 27th European Photovoltaic Solar Energy Conference and Exhibition, Franfkurt, Germany, 2012, pp. 2049–2052.*

OTHER CO-AUTHORSHIPS PUBLISHED IN THE DURATION OF THE THESIS

- *K. M. Johansen, H. Haug, E. Lund, E. V. Monakhov, and B. G. Svensson, "Thermal stability of the OH–Li complex in hydrothermally grown single crystalline ZnO," Appl. Phys. Lett., vol. 97, no. 21, p. 211907, 2010.*

- *K. M. Johansen, H. Haug, Ø. Prytz, P. T. Neuvonen, K. E. Knutsen, L. Vines, E. V Monakhov, A. Y. Kuznetsov, and B. G. Svensson, "Li and OH-Li Complexes in Hydrothermally Grown Single-Crystalline ZnO," J. Electron. Mater., vol. 40, no. 4, pp. 429–432 LA – English, 2011.*

CHAPTER 2

CARRIER RECOMBINATION IN CRYSTALLINE SILICON

Carrier recombination is one of the major factors limiting solar cell efficiency, as generated electron-hole pairs may recombine before they can contribute to the collected current. In this chapter a general introduction to carrier recombination mechanisms in semiconductors is presented, to provide the reader with the necessary theoretical background for the measurements, simulations and discussions of the later chapters. Most of the equations presented here are previously described in several good textbooks on the topic [5] [6] [7], and interested readers are referred to these for more information.

Carrier recombination may be due to several different physical processes. The main focus of this thesis will be on recombination at the surfaces of the semiconductor. Experimentally, it is normally only the combined contributions from all of these processes that can be measured, including both surface and bulk recombination. A good understanding of recombination both in the bulk and at the surfaces of the material is therefore required.

2.1 INTRODUCTION TO CARRIER RECOMBINATION

When a semiconductor is exposed to light with photon energy larger than the band gap energy, excited charge carriers are created in the material. This creation of electron-hole pairs is referred to as *generation*. For the system to return to thermal equilibrium the reverse process must also occur, where a free electron in the conduction band of the semiconductor combines with a hole and the energy is released, in the form of photons or phonons. This

process is called *recombination*. Experimentally, the recombination processes are measured as the recombination lifetime τ, which is defined by

$$\tau \equiv \frac{\Delta n}{U}, \tag{2.1}$$

where Δn is the excess carrier concentration and U is the recombination rate per volume. Each recombination process can be described with a characteristic recombination rate U and a lifetime τ.

2.2 BULK RECOMBINATION MECHANISMS

2.2.1 INTRINSIC RECOMBINATION

Some of the recombination mechanisms in a semiconductor are *intrinsic*, which means that they are inherent to the existence of separated energy bands in the material.

2.2.1.1 Radiative recombination

Radiative recombination is the reverse process to optical generation, where an electron-hole pair is directly annihilated, releasing the excess energy as a photon with an energy close to the band gap of the material. The radiative recombination rate is determined by the deviation of the product of the electron and hole concentration from electron hole product at thermal equilibrium, $n_0 p_0 = n_i^2$

$$U_{rad} = B_{rad}\left(np - n_i^2\right). \tag{2.2}$$

where n_i is the intrinsic carrier concentration at thermal equilibrium. The constant of proportionality B_{rad} is a material-specific parameter called the *radiative recombination coefficient*. Silicon is an indirect band gap semiconductor, and the probability for direct band-to-band transitions is therefore low compared to direct band gap semiconductors. The rate of radiative recombination in Si is generally considered to be small or negligible compared to other recombination mechanisms. For Si, B_{rad} has a value of 9.5×10^{-15} cm^3s^{-1} at room temperature [8]. For comparison, B is over three orders of magnitude larger in the direct semiconductor GaAs, with $B_{rad} = 2 \times 10^{-11}$ cm^3s^{-1} [9].

To obtain a further understanding of the different recombination processes, it is useful to study a few limiting cases. Throughout this chapter we will consider a p-type sample for this purpose, but the equations are equally valid for n-type by changing the carrier and doping types. Firstly, we can normally assume that the excess minority carrier density Δn is much larger than n_0, and that the last term in the parenthesis in Eq. (2.2) may be omitted. The

electron and hole concentrations can then also be safely approximated as $n = \Delta n$ and $p = N_A + \Delta n$. Low injection conditions are defined as the limiting case when $\Delta n \ll N_A$, giving the carrier concentrations as $n = \Delta n$ and $p = N_A$. On the other hand, high injection conditions refer to the situation when $\Delta n \gg N_A$, so that $n = p = \Delta n$. For low and high injection conditions, the radiative recombination lifetime $\tau_{rad} = \Delta n / U_{rad}$ simplifies to

$$\tau_{rad,li} = \frac{1}{B_{rad} N_A} \quad \text{and} \quad \tau_{rad,hi} = \frac{1}{B_{rad} \Delta n}, \tag{2.3}$$

respectively. In both cases τ_{rad} scales with the inverse of the majority carrier concentration.

As Si is an indirect band gap material, the contribution from radiative recombination is normally low compared to the other recombination mechanisms. It is however relevant for lifetime measurements based on photoluminescence, as shall be described in section 4.2.3.

2.2.1.2 Auger recombination

Auger recombination can be described by a three-particle interaction, where an electron and a hole recombine, transferring the excess energy to a conduction band electron (*eeh* process) or a hole in the valence band (*ehh* process). As for radiative recombination, the recombination rate for Auger recombination is given as the product of the concentrations of the involved carriers:

$$U_{Aug} = C_n\left(n^2 p - n_i^2 n_0\right) + C_p\left(n p^2 - p_0 n_i^2\right) \approx C_n n^2 p + C_p n p^2, \tag{2.4}$$

where C_n and C_p are the Auger coefficients. The simplified expressions for the Auger lifetime of a p-type sample becomes

$$\tau_{Aug,li} = \frac{1}{C_p N_A^2} \quad \text{and} \quad \tau_{Aug,hi} = \frac{1}{\left(C_n + C_p\right)\Delta n^2} \tag{2.5}$$

for low and high injection conditions, respectively. Note that the Auger lifetime scales with the inverse of the majority carrier concentration *squared*. Auger recombination thus becomes the dominant recombination mechanism in Si for very high injection levels or in heavily doped regions. The latter is commonly observed in the emitter of Si solar cells.

Experimentally, the observed Auger lifetime is lower than that predicted from Eq. (2.4), particularly for low injection conditions. This has been attributed to columbic interaction of the charge carriers, which causes an enhancement of the recombination rate. Several models have been proposed to correct for this, thus obtaining a better fit with experimental data. In this work we have used the model of Kerr and Cuevas [10], which has

been determined by empirically fitting the model to an extensive data set. The Auger recombination lifetime is then given by

$$\tau_{Aug} = \frac{\Delta n}{np\left(1.8 \times 10^{-24} n_0^{0.65} + 6 \times 10^{-25} p_0^{0.65} + 3 \times 10^{-27} \Delta n^{0.8}\right)}. \quad (2.6)$$

In the last years, progress in surface and material quality and improved characterization techniques have led to an improved determination of the Auger recombination rate. The latest and most precise Auger parameterization was published by Richter et al in 2012 [11]. However, the new model does not significantly alter the results for the doping and injection levels relevant for this work, and the model of Kerr and Cuevas has therefore been kept for the sake of consistency.

2.2.2 *RECOMBINATION VIA DEFECTS*

The intrinsic recombination mechanisms described above are caused by band-to-band transitions. They are independent of the material quality and can thus be regarded as an upper limit for the lifetime that can be measured in the material. In actual Si crystals however, a certain concentration of defects or imperfections will always be present. These defects may be extended defects like dislocations or stacking faults, intrinsic point defects or extrinsic point defects (impurities), which may all produce discrete energy levels within the band gap. These levels may greatly increase the recombination rate through a two-step process whereby an electron from the conduction band first relaxes to the defect level and then relaxes to the valence band where it annihilates a hole. Defect energy levels in the central part of the band gap typically have similar probability for capturing electrons from the conduction band and holes from the valence band holes and are typically referred to as *recombination centers*. If the defect level is close to one of the band edges the probability for capture and re-emission is normally much larger for one type of charge carrier. Such energy levels are commonly referred to as electron- or hole *traps*. The dynamics of the recombination process via defect states in the band gap was first investigated by Shockley and Read [12] and in parallel by Hall [13], and the recombination process is therefore referred to as *Shockley-Read Hall* (SRH) recombination. According to SRH theory, the recombination rate caused by a defect with concentration N_t with a single energy level E_t is given by

$$U_{SRH} = \frac{np - n_i^2}{\tau_{p0}(n + n_1) + \tau_{n0}(p + p_1)}, \quad (2.7)$$

where τ_{n0} and τ_{p0} are the electron and hole capture time constants, defined as

$$\tau_{n0} = \frac{1}{\sigma_n N_t v_{th}}, \qquad \tau_{p0} = \frac{1}{\sigma_p N_t v_{th}}. \tag{2.8}$$

Here, σ_n and σ_p are the capture cross sections for electrons and holes, respectively, and v_{th} is the carrier thermal velocity ($v_{th} = 10^7$ cm/s in Si at 300 K [2, p. 19]). n_1 and p_1 are statistical factors defined by what the equilibrium electron and hole concentrations would be if the Fermi level of the material was at the defect energy level:

$$n_1 = n_i \exp\left(\frac{E_t - E_i}{k_B T}\right), \qquad p_1 = n_i \exp\left(\frac{-(E_t - E_i)}{k_B T}\right), \tag{2.9}$$

By combining Eqs. (2.1) and (2.7), the SRH recombination lifetime can be written as

$$\tau_{SRH} = \frac{\tau_{n0}(p_0 + p_1 + \Delta n) + \tau_{p0}(n_0 + n_1 + \Delta n)}{n_0 + p_0 + \Delta n}. \tag{2.10}$$

For low injection conditions and deep defect levels ($n_1 \ll n$, $p_1 \ll p$), Eq. (2.10) can be simplified to $\tau_{SRH} = \tau_{n0}$ for p-type and $\tau_{SRH} = \tau_{p0}$ for n-type samples. For high injection conditions the SRH lifetime again becomes independent of the injection level, with $\tau_{SRH} = \tau_{n0} + \tau_{p0}$.

2.3 SURFACE RECOMBINATION

Surface recombination at Si surfaces is a central part of the thesis, and we will therefore go more thoroughly into the theoretical foundations of this topic. Much of the first parts of this section is based on the excellent textbook by Aberle [6] and references therein.

2.3.1 BASIC CONCEPTS AND DEFINITIONS

The surface of a semiconductor sample terminates the periodicity of the crystal lattice, introducing localized states at the surface. These surface defect states may work as active recombination centers in the same way as the bulk defect states discussed above. The surface defect states may be dangling bonds caused by the large number of partially bonded Si atoms at the surface or they can be caused by local stress in the crystal lattice created as the surface reorganizes to the lowest energy configuration. These types of defect states are present even in a pure, perfect crystal, and are therefore called *intrinsic states*.

The density of dangling bonds at the surface may be reduced by forming chemical bonds with other atoms. These bonds may however also act as effective recombination centers. Extrinsic states are surface states caused by bonds to foreign atoms, which can be present either as single adatoms or as a more or less continuous surface layer. When a bare Si surface is exposed to air, it will rapidly react with the oxygen molecules in the atmosphere, forming a 1-2 nm thick layer of so-called native oxide. This thin oxide layer is however still highly recombination active. A better way of reducing the density of recombination active surface states is to create a controlled interface between the Si crystal and a surface passivation layer. The defect states formed between the two materials are then most precisely described as interface states. However, since the passivation layer thickness is small (typically in the order of tens of nanometers) and the generation and recombination of carriers outside of the semiconductor usually can be neglected, the terms *interface* and *surface* are often used interchangeably when speaking of defect states and recombination. Several examples of common passivation layers used in Si solar cells are given in section 2.5.2 below.

The recombination at the surface can be treated with the same SRH dynamics described in section 2.2.2, only this time formulated in terms of the recombination rate per surface *area*, instead of per surface volume. The most important difference between bulk and surface recombination is that the recombination active defect states at the surface are not restricted to discrete energy levels, but are distributed continuously over the entire band gap. The single defect level(s) must therefore be replaced by a distribution, the interface state density per energy interval $D_{it}(E)$, which is normally given in units of $\mathrm{cm}^{-2}/\mathrm{eV}$. In early work by Grove and Fitzgerald [14] [15] the surface recombination rate was for the first time described by an extended SRH formalism. The total surface recombination rate is found by integrating the SRH recombination rate over the band gap:

$$U_s = \left(n_s p_s - n_i^2\right) v_{th} \int_{E_v}^{E_c} \frac{D_{it}(E)}{\frac{n_s + n_1(E)}{\sigma_p(E)} + \frac{p_s + p_1(E)}{\sigma_n(E)}} dE, \tag{2.11}$$

where n_s and p_s are the electron and hole concentrations at the surface. Since the surface recombination rate is defined per unit area, it does not make sense to define a surface recombination lifetime on the form of Eq. (2.1). Instead we use a *surface recombination velocity* (SRV), defined as the rate of surface recombination divided by the excess carrier concentration at the surface Δn_s. The inverse of the SRV is thus on the same form as Eq. (2.1):

$$\frac{1}{S} = \frac{\Delta n_s}{U_s}. \tag{2.12}$$

Since the SRV is defined in the inverse manner of the recombination lifetime, a high SRVs corresponds to a high recombination activity at the surface. Because U_s has units of cm²/s, the SRV is measured in units of cm/s.

A common simplification of Eq. (2.11) is to replace the interface distribution with a single, effective defect level with a concentration per area given by N_{it}. The rate of surface recombination U_S is can then be simplified to:

$$U_s = \frac{S_{n0}S_{p0}\left(n_s p_s - n_i^2\right)}{S_{n0}(n_s + n_1) + S_{p0}(p_s + p_1)}\ , \tag{2.13}$$

where S_{n0} and S_{p0} are the effective surface recombination parameters, defined as

$$S_{n0} = \sigma_n N_{it} v_{th} \quad \text{and} \quad S_{p0} = \sigma_p N_{it} v_{th}. \tag{2.14}$$

2.3.2 *FLAT BAND CONDITIONS*

The simplest way of describing the recombination at a semiconductor surface is when there are no electric fields present near the surface. The band structure is then similar to that found in the bulk of the material, so that n_s and p_s equals n and p, respectively. The SRV is then given by

$$S = (n_0 + p_0 + \Delta n) v_{th} \int_{E_v}^{E_c} \frac{D_{it}(E)}{\frac{n_0 + \Delta n + n_1(E)}{\sigma_p(E)} + \frac{p_0 + \Delta n + p_1(E)}{\sigma_n(E)}} dE. \tag{2.15}$$

To better understand this expression it is useful to study some limiting cases. If we consider a p-type sample under low injection conditions ($N_A \gg \Delta n$) and deep defect levels ($n \gg n_1, p \gg p_1$), Eq. (2.15) simplifies to $S_{li} = v_{th} \int_{E_v}^{E_c} D_{it}(E)\sigma_n(E)dE$. If we consider only a single defect level, the SRV is simply reduced to the effective SRV parameter for minority carriers (in this case electrons): $S_{li} = v_{th} N_{it} \sigma_n = S_{n0}$.

For high injection conditions the SRV again is independent of Δn. Still considering a p-type sample and a single defect level, the high injection SRV is given by:

$$S_{hi} = \frac{S_{p0}}{1 + \frac{S_{p0}}{S_{n0}}}. \tag{2.16}$$

From this we can observe that S_{hi} always is smaller than S_{li}, and that the difference is determined by the ratio between the effective SRV parameters for majority and minority carriers S_{p0}/S_{n0}, which again is given by the ratio of the capture cross sections σ_p/σ_n. For equal capture cross sections $S_{hi} = S_{li}/2$. This can be understood in the following manner: At low injection conditions the total recombination rate at the surface is limited by the capture of minority carriers only, as the majority carriers are in great excess. At high injection the concentration of both carrier types limit the recombination rate. Since the SRV is defined as the recombination rate divided by the excess carrier concentration the SRV is reduced. A further discussion on $S(\Delta n)$ curves will be presented in section 3.1.2.

2.3.3 *SURFACE BAND BENDING*

Electrical charges are often present at or close to the silicon surface, for instance in the form of charged ions, fixed charges in a dielectric surface layer or in a metal electrode placed on top of the dielectric layer. These charges create an electric field in the region close to the surface, and the surface concentration of electrons and holes n_s and p_s may thus differ significantly from the electron and hole concentrations in the bulk of the material. It is however still useful to relate the SRV to the injection level in the bulk, in order to describe the total flow of carriers towards the surface. The *effective* surface recombination velocity associated with recombination at the interface states S_{it} is therefore defined as

$$S_{it} = \frac{U_s}{\Delta n(x = d_{sc})}, \tag{2.17}$$

where $\Delta n(x = d_{sc})$ is the injection level at the edge of the surface space charge region.

Furthermore, because of the changed carrier concentrations at the surface, the simplified picture described above is not sufficient to describe the surface recombination, as the SRV is a function of n_s and p_s in addition to the electrical properties of the surface defects $(D_{it}(E), \sigma_n(E), \sigma_p(E))$. In order to calculate the effective SRV under these conditions it is first necessary to calculate n_s and p_s. In the neutral (field free) bulk of a semiconductor sample under illumination, the concentration of charge carriers n_b and p_b is given by

$$n_b = n_0 + \Delta n = n_i \mathrm{e}^{-\beta\phi_n}, \quad p_b = p_0 + \Delta n = n_i \mathrm{e}^{\beta\phi_p}, \tag{2.18}$$

where ϕ_n and ϕ_p are the quasi-Fermi levels for electrons and holes, respectively, and $\beta \equiv q/k_B T$. In low injection conditions, where $n_b = \Delta n$ and $p_b = N_A$ (for p-type material), the separation of the quasi-Fermi levels $V_b = \phi_p - \phi_n$ is related to the injection level Δn by the expression

$$\Delta n = \frac{n_i^2}{N_A}\left(e^{\beta V_b} - 1\right) \tag{2.19}$$

Under the influence of an additional electrical potential $\psi(x)$, the carrier concentrations are given by

$$n(x) = n_b \mathrm{e}^{\beta\psi(x)}, \quad p(x) = p_b \mathrm{e}^{-\beta\psi(x)}, \tag{2.20}$$

By inserting the *surface potential* ψ_s in the general expression above we can calculate n_s and p_s as

$$n_s = n_b \mathrm{e}^{\beta\psi_s(x)}, \quad p_s = p_b \mathrm{e}^{-\beta\psi_s}. \tag{2.21}$$

Calculation of the effective SRV with surface band bending is thus reduced to determining the value of the surface potential. The exact solution can be found by solving the continuity equations for electrons and holes as well as the Poisson equation for a given set of boundary conditions. These equations are however not generally possible to solve analytically. In this work we have used a simpler, numerical approach suggested by Girisch et al. [16] to find ψ_s.

2.3.3.1 The Girisch model

Girisch et al. [16] showed that a good approximate solution of the surface band bending problem can be found if one assumes constant quasi-Fermi levels throughout the surface space charge region. This is normally a good approximation for Si solar cell passivation experiments [17]. The Girisch model can be used to numerically calculate the surface potential (and thus the SRV) both as a function of the injection level and the surface charge density. The model has successfully been used in several publications in the past to simulate the SRV at the interface between Si and various passivation materials, like SiO_2 [18], [19], a-SiN_x:H [20], a-Si:H [21], Al_2O_3 [22] and different stack systems [23]. A good description can also be found in refs. [6] and [17]

The starting point of the calculation is an assumption of charge neutrality within the sample:

$$Q_g + Q_f + Q_{it} + Q_{sc} = 0. \tag{2.22}$$

Here, Q_g is the charge in a gate electrode deposited on top of the dielectric (if such an electrode exists), Q_f is the fixed dielectric charge density, Q_{it} is the charge associated with charged defect states at the interface and Q_{sc} is the induced charge in the space charge region of the semiconductor. A typical spatial distribution of these charges is shown schematically in Figure 2.1.

The insulator fixed charge density Q_f is a constant property of the dielectric passivation layer, and can be measured for instance by capacitance-voltage measurements of a metal-insulator-semiconductor (MIS) structure. The gate charge Q_g is given by

$$Q_g = \frac{\epsilon_0 \epsilon_i}{d_i q}\left(V_g + \Delta\phi_{ms} - \psi_s\right) - \frac{Q_f d_f}{2d_i} \tag{2.23}$$

where ϵ_0 is the free space permittivity, ϵ_i is the relative permittivity of the insulator, V_g is the applied voltage, d_i is the insulator thickness, d_f is the thickness of the region containing fixed charges and $\Delta\phi_{ms}$ is the metal-semiconductor work function difference. Note that the expression $\epsilon_0\epsilon_i/d_i$ corresponds to the insulator capacitance per unit area.

In Eq. (2.23) a constant charge distribution has been assumed between the interface and $x = d_f$ (see Figure 2.1). If all the fixed charges are placed at $x = d_f$ the number 2 in the denominator may be omitted. Throughout most of this work, we have assumed that the fixed charges are placed at the interface, so that the last term in Eq. (2.23) is zero.

$\Delta\phi_{ms}$ can be calculated from the metal work function F_m and the electron affinity of Si χ_{Si} as [7]

$$\begin{aligned} \Delta\phi_{ms} &= F_m - \chi_{Si} - \frac{E_g}{2} - \frac{k_B T}{q}\ln\left(\frac{N_A}{n_i}\right) \quad \text{(p-type)}, \\ \Delta\phi_{ms} &= F_m - \chi_{Si} - \frac{E_g}{2} + \frac{k_B T}{q}\ln\left(\frac{N_D}{n_i}\right) \quad \text{(n-type)}. \end{aligned} \tag{2.24}$$

Al electrodes have been used for all the measurements presented in this work. By inserting $F_m = 4.1$ eV for Al and $\chi_{Si} = 4.05$ eV we get $\Delta\phi_{ms} = 0.0853 - 0.0259 \times \ln(N_A)$ and $\Delta\phi_{ms} = -1.105 + 0.0259 \times \ln(N_D)$ for p-type and n-type, respectively. (For a substrate resistivity of 2.8 Ωcm, $\Delta\phi_{ms}$ becomes -0.84 V and -0.20 V for p-type and n-type wafers, respectively.)

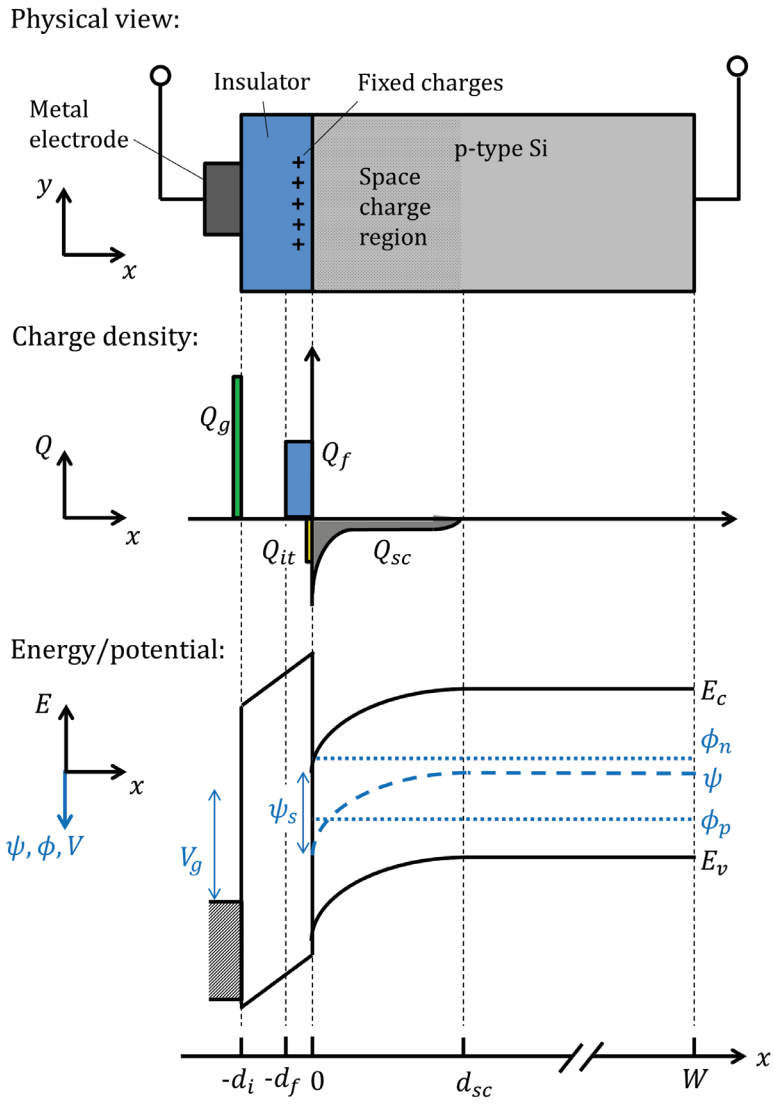

Figure 2.1. Top: Schematic illustration of a metal-insulator-semiconductor (MIS) structure on p-type Si. Middle: Charge distribution, illustrating the charge balance of the system described by Eq. (2.22). Bottom: Energy band diagram and potentials. A constant positive charge density between $x = 0$ and $x = -d_f$ and a positive gate voltage V_g has been assumed.

The charge associated with the interface states Q_{it} depends on the distribution of donor- and acceptor-like interface states $D_{it,d}$ and $D_{it,a}$ throughout the band gap:

$$Q_{it} = q \int_{E_c}^{E_v} \left[D_{it,d}(E) f_d(E) - D_{it,a}(E) f_a(E) \right] dE, \tag{2.25}$$

where f_a is the electron occupancy function for acceptor states and f_d is the hole occupancy function for donor states. For steady-state conditions, the rate of capture minus emission must be zero for each trap. This leads to the following expressions for f_a and f_d:

$$f_a(E) = \frac{\sigma_n n_s + \sigma_p p_1}{\sigma_n (n_s + n_1) + \sigma_p (p_s + p_1)}, \quad f_d(E) = \frac{\sigma_n n_1 + \sigma_p p_s}{\sigma_n (n_s + n_1) + \sigma_p (p_s + p_1)}. \tag{2.26}$$

The last term in the charge neutrality in Eq. (2.22) is the induced charge in the semiconductor space charge region below the surface. If flat quasi-Fermi levels are assumed, an analytical expression for Q_{sc} as a function of ψ_s can be found by solving the one-dimensional Poisson equation:

$$\frac{d^2\psi}{dx^2} = -\frac{\rho(x)}{\epsilon_0 \epsilon_s} = \frac{q(p(x) + N_A - n(x) - N_D)}{\epsilon_0 \epsilon_s}, \tag{2.27}$$

where $\rho(x)$ is the total charge density. By inserting the expression for $n(x)$ and $p(x)$ from Eqs. (2.20) into Eq. (2.27) and solving for the total charge [14], the induced charge in the semiconductor space charge region Q_{sc} can be found as a function of ψ_s as

$$Q_{sc} = \mp \sqrt{\frac{2 n_i \epsilon_0 \epsilon_s}{q\beta} \left(e^{\beta(\phi_p - \psi_s)} - e^{\beta \phi_p} + e^{\beta(\psi_s - \phi_n)} - e^{-\beta \phi_n} + \beta \psi_s \frac{N_A - N_D}{n_i} \right)}. \tag{2.28}$$

The upper sign in Eq. (2.28) refers to $\psi_s > 0$ and the lower sign to $\psi_s < 0$. The quasi-Fermi levels for electrons and holes ϕ_n and ϕ_p in the bulk can be calculated using (2.18) as long as both N_A (or N_D) and Δn are known.

Based on these expressions, ψ_s can be calculated by solving the set of equations given by Eqs. (2.22), (2.23), (2.25) and (2.28). The practical implementation in the simulations will be presented in section 3.1.

2.3.4 *OTHER SURFACE-RELATED RECOMBINATION MECHANISMS*

In order to correctly describe the experimentally observed injection level- and dependence and the effect of surface potential on the SRV, Glunz et al. [19] proposed an

extension to the standard extended SRH model described above. The first extension is the inclusion of shunt currents through the space charge region. By also considering quantum effects, there will be a certain probability for tunneling of charge carriers through the potential barrier, where they can recombine at highly recombinative spots at the surface. This recombination mechanisms can be described as a loss current through a shunt conductor with resistance R_{sh}. For p-type material the corresponding SRV can be described as

$$S_{R_{sh}} = \frac{V_b/R_{sh}}{qn_0(e^{\beta V_b}-1)} \approx \frac{1}{q\beta R_{sh}\Delta n}\ln\left(\frac{\Delta n}{n_0}+1\right), \tag{2.29}$$

where $V_b = \phi_p - \phi_n$ is the separation of the Fermi levels in the bulk. The simplified expression to the right is calculated using Eq. (2.20), which is valid under low injection conditions.

Glunz et al. also included a SRV contribution from carrier recombination in the space charge region below the surface. Defects that are present in a subsurface damage region (SDR) can act as highly effective recombination centers, particularly under inversion conditions, as a large recombination rate is expected at the crossover point where the electron and hole concentrations are of similar magnitude. Similarly to the space charge recombination in a diffused junction, the recombination current can be modeled as a loss current through a diode with ideality factor 2. Later, Dauwe [17] performed analytical calculations of the space charge recombination, and concluded that the ideality factor m usually is less than 2, and typically lies in the range between 1.5 and 1.8, depending on the properties of the subsurface defects and the injection level. For p-type material the expression for the SRV associated to the recombination in the space charge region then becomes

$$S_{SDR} = \frac{J_{02}}{q\Delta n}\left(e^{\frac{qV_b}{mk_BT}}-1\right) \approx \frac{J_{02}}{q\Delta n}\left(\left(\frac{\Delta n}{n_0}+1\right)^{1/m}-1\right), \tag{2.30}$$

where J_{02} is the saturation current density. Again Eq. (2.20) has been used when going from the second to the third term.

If these additional recombination mechanisms are included, the total effective SRV can be calculated as the sum of the different contributions

$$S_{eff} = S_{it} + S_{R_p} + S_{SDR}. \tag{2.31}$$

The SDR recombination was also recently studied by Steingrube et al. [24], who used the model to describe an extensive set of experimental data. They calculated the SRV contributions to the SRV as

$$S_{SDR} = \frac{\int U_{SRH}(x)dx}{\Delta n(x = d_{sc})}, \tag{2.32}$$

using a simplified expression for Q_{Si} (Eq. (2.28)) to calculate the carrier concentrations below the surface together with an exponential function for the SRH recombination parameters $\tau_{n0,SDR}$ and $\tau_{p0,SDR}$ in the SDR. The impact of these additional SRV contributions will be discussed in sections 3.2.2 and 5.2.5, as well as in Papers II and III.

2.4 EFFECTIVE CARRIER LIFETIME

The different recombination mechanisms in the bulk (section 2.2) and at the surface (section 2.3) will typically occur simultaneously within a semiconductor sample. The effective carrier lifetime τ_{eff}, which typically is the parameter that can be determined experimentally, is therefore a combination of all the different recombination mechanisms. Some of these mechanisms are more important than others, so that those processes with the highest recombination will dominate the measured value of τ_{eff}.

The total bulk recombination rate is found by adding the recombination rates for the different mechanisms described in section 2.2: $U_b = U_{rad} + U_{Aug} + U_{SRH}$. Since the recombination lifetime is inversely proportional to the recombination rate, the total bulk lifetime τ_b can be found by inversely adding the different lifetime contributions:

$$\frac{1}{\tau_b} = \frac{1}{\tau_{rad}} + \frac{1}{\tau_{Aug}} + \frac{1}{\tau_{SRH}}. \tag{2.33}$$

(Note that the expression for τ_{SRH} described above is valid for a single defect level. In an actual Si crystal, the SRH recombination will be a combination of many different defects. τ_{SRH} is therefore most precisely described as

$$\frac{1}{\tau_{SRH}} = \sum_{i}^{N} \frac{1}{\tau_{SRH,i}}, \tag{2.34}$$

where $\tau_{SRH,i}$ is the recombination lifetime arising from a single defect level.)

The different contributions to the bulk lifetime are shown schematically in Figure 2.2. Note that because of the inverse addition of lifetime contributions the total bulk lifetime is dominated by the recombination process with the lowest recombination lifetime at a given injection level.

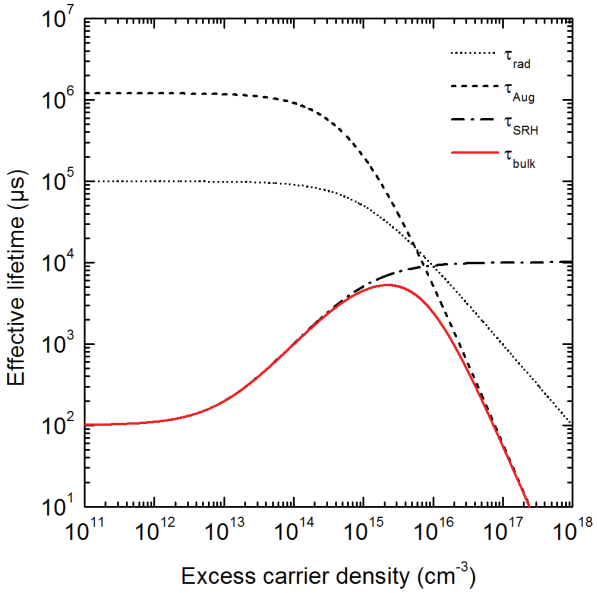

Figure 2.2. Effective lifetime as a function of injection level Δn for the different bulk recombination mechansims described above. The total effective lifetime is shown as a solid, red line. ($\tau_{n0} = 100$ µs, $\tau_{p0} = 10000$ µs and $N_A = 1 \times 10^{15}$ cm^{-3}).

By solving the second order differential equations describing the carrier decay within the sample, it is possible to find an analytical expression for the effect of surface and bulk recombination on the effective lifetime. For the general case, where the SRV at the two sample surfaces S_f and S_r can have different values, the solution is given by

$$\frac{1}{\tau_{eff}} = \frac{1}{\tau_b} + \alpha_0^2 D, \tag{2.35}$$

where D is the diffusion coefficient and α_0 is the smallest eigenvalue solution of the following equation[1]:

[1] At low injection the minority carrier diffusivity should thus be used for D. At high injection, on the other hand, diffusion of both carriers is necessary, and D should therefore be the ambipolar diffusion coefficient D_a [25].

$$\tan(\alpha_0 W) = \frac{S_f + S_r}{\alpha_0 D - \frac{S_f S_r}{\alpha_0 D}}\ , \tag{2.36}$$

where W is the sample thickness [25]. Eq. (2.36) is a transcendental equation and must therefore be solved numerically. This calculation has been performed using Matlab for all the experimental and simulated data presented in this thesis and in the attached papers. It is however still instructive to consider a few of the commonly used approximate solutions: If the sample is symmetrically passivated ($S_f = S_r = S$) and S is small, the tangent function in Eq. (2.36) can be linearly approximated, and the effective lifetime is simply given by

$$\frac{1}{\tau_{eff}} = \frac{1}{\tau_b} + \frac{2S}{W}. \tag{2.37}$$

This expression is correct within a 4% error for $S < D/4W$ [25]. On the other hand, for symmetrically passivated samples with very large S, the effective lifetime is solely determined by diffusion of carriers towards the surface, and the solution can be approximated as

$$\frac{1}{\tau_{eff}} = \frac{1}{\tau_b} + D\left(\frac{\pi}{W}\right)^2. \tag{2.38}$$

Interestingly, by simply adding the two expressions for the surface recombination in Eqs. (2.37) and (2.38), we obtain a simple expression that is correct within an error of 5% for the entire range of S [25].

$$\frac{1}{\tau_{eff}} = \frac{1}{\tau_b} + \frac{2S}{W} + D\left(\frac{\pi}{W}\right)^2. \tag{2.39}$$

2.5 SURFACE PASSIVATION

Surface passivation is the act of reducing the SRV at the wafer surface, thereby increasing the effective lifetime of the wafer. In this section, the two main strategies surface passivation will be introduced, followed by a brief review of some commonly used materials.

2.5.1 SURFACE PASSIVATION STRATEGIES

By examining the equation for SRH recombination at the surface in Eq. (2.11), two fundamentally different strategies for reducing the SRV can be identified: Either the density

and recombination activity of the interface states can be reduced, or the concentration of one of the charge carriers at the interface can be reduced. In practice, both of these approaches are often combined to achieve sufficiently low SRVs.

2.5.1.1 Reduction of the density of interface states

According to Eq. (2.11) the SRV is directly proportional to the density of interface states D_{it}. The process of reducing D_{it} is often referred to as *chemical passivation.* A bare (100)-oriented Si surface consists of approximately 7×10^{14} surface atoms per cm^2, and interface state densities N_{it} are measured to be in the order of 1×10^{13} cm^{-2} on non-passivated surfaces [3, p. 78]. This number can however be drastically reduced by deposition or growth of an appropriate surface passivation layer. The traditional method for passivating Si surfaces is thermal oxidation at high temperature (~1000 ℃) [26]. This process is capable of providing surface state densities as low as $\sim 10^9$ cm^{-2} [27], a reduction of 4 orders of magnitude.

Another method for reducing the number of interface states is to strip off the native oxide layer in an HF solution, creating a clean, hydrogen-terminated surface. By keeping the sample immersed in HF or certain other liquids like an iodine/ethanol solution the SRV can be extremely low because of the very low D_{it} [28]. This method is sometimes used for measurements of the bulk lifetime of Si wafers, but is impractical and often difficult to use in a safe manner. A better solution is to use a dip in HF as the first process step, before using a thin film deposition method to create a layer of a different material on the surface, creating bonds to the surface Si atoms. The by far most common example of this for solar cell applications is the use of plasma enhanced chemical vapor deposition (PECVD) for deposition of layers of amorphous, hydrogenated silicon (a-Si:H) or silicon nitride (a-SiN_x:H). These layers typically contain a large concentration of hydrogen, which can diffuse to the surface and bind to dangling bonds, thus reducing D_{it}. Further details on the wafer cleaning and the PECVD process is presented in sections 4.1.1 and 4.1.2, and a more detailed overview of PECVD passivation materials is given in section 2.5.2.

2.5.1.2 Reducing the surface concentration of charge carriers

A SRH recombination event requires the simultaneous presence of an electron and a hole, and the rate of recombination will therefore be limited by the charge carrier with lowest concentration (given equal capture cross sections). By reducing the concentration of one type of charge carriers at the surface by means of an electric field the SRV may therefore be significantly reduced. This “built-in” electric field may be created by a doping profile below the surface, or by implementing electrical charges in a dielectric layer on the surface or in a gate electrode. In Si solar cells a high-low (same polarity) diffused doping profile is often used to reduce the recombination losses at the rear of the solar cell. This doping profile is typically

created by in-diffusion of Al from the metal contacts into the p-type base material, and is traditionally referred to as a *back surface field* (BSF) [29]. The p-n junction itself will also provide passivation of the surface, in addition to separate the light-induced charge carriers (a non-contacted junction used only for passivation purposes is called a *floating junction*).

This thesis has primarily been focused on passivation of non-diffused surfaces. *Field-effect passivation* is the use of charges to change the surface potential and thus the surface concentration of electrons and holes, as described in section 2.3.3.1. Many types of dielectric passivation layers have implemented stable charges at or near the Si/dielectric interface, leading to different behaviors for the SRV. Several examples of the effect of such charges on the passivation properties are presented in section 2.5.2 below. A large part of this work concerns experiments where the field-effect passivation can be controlled and manipulated, either by the use of removable surface charges or induced charges in a gate electrode. Simulations of the effect of variable field-effect passivation on the SRV are presented in Chapter 3, and experimental methods and results are described in Chapter 5.

2.5.2 MATERIALS FOR SURFACE PASSIVATION OF CRYSTALLINE SILICON

The most common materials for surface passivation in the c-Si PV industry are a-SiN_x:H, a-Si:H, SiO_2, and lately also Al_2O_3. The literature on the subject is vast, and a full overview of the process development and passivation results is beyond the scope of this thesis. Interested readers are referred to one of the latest review papers on the subject [30], [31], [22], [32] and references therein. The deposition parameters and selected properties of the different surface passivation materials used in this work are given in section 4.5.

2.5.2.1 Silicon nitride

Silicon nitride is a dielectric material that has been successfully incorporated in a large variety of electronic devices. Silicon nitride layers for solar cell applications are almost universally processed by PECVD (described in section 4.1.2), because it enables the fabrication of thin films at low temperature with a high deposition rate, which both are important prerequisites for large scale, high throughput production. The method uses hydrogen-containing precursors like SiH_4 and NH_3, and produces amorphous, non-stoichiometric films with up to 40 atomic % of H. The material is therefore best referred to as a-SiN_x:H, where x denotes the nitrogen/silicon atomic ratio [4]. a-SiN_x:H is the most important thin film dielectric in c-Si solar cell production, mainly because of the following important properties:

- Suitable optical properties to serve as an antireflection coating, with tunable refractive index from approximately $n = 1.8$ and upwards.
- A large positive fixed charge density suitable for passivation of the commonly used n-type emitters.
- Good chemical and thermal stability.
- A large hydrogen concentration. Hydrogen released during the high temperature contact firing process plays an important role in passivating both the interface and bulk defects in multicrystalline material [33].

Much work has been published on the surface passivation quality of a-SiN_x:H layers as a function of processing conditions [34],[35],[36],[37],[38]. The results are however not generally transferable between different deposition systems and the process must typically be optimized separately for each lab. One general trend that can be observed from the literature is that the optimal passivation is normally achieved for Si-rich layers. These films have a high refractive index, a moderate charge density, but a high degree of chemical passivation (these properties tends towards those of a-Si:H). N-rich a-SiN_x:H layers are however more chemically and thermally stable, and typically contain a large density of positive fixed charges (in the order of 10^{12} cm^{-2}), giving a stronger field-effect passivation [39]. This trend was also observed for the experiments presented in Paper IV.

The fixed charges in a-SiN_x:H layers has been attributed to the so-called K-centers, which are located within the first 20 nm from the interface and consist of a Si dangling bond backbonded by three N atoms [40]. The charge state of these centers can be changed by interaction with conduction band electrons in the underlying Si wafer, an effect that is most commonly observed as a large hysteresis effect in C-V measurements [41],[42], (see Paper II and IV for details).

a-SiN_x:H layers can also be used for surface passivation of p-type material, where the positive Q_f results in an inversion layer below the surface. Record low effective SRV of 4 cm/s has been obtained on 1 Ωcm p-type Si wafers passivated by remote PECVD or high-frequency direct PECVD [43]. Implementing such an inversion-type passivation layer on the rear side of p-type Si solar cells may however lead to a detrimental effect called parasitic shunting, caused by a the recombination between holes flowing towards the rear contact and electrons in the inversion layer [44].

2.5.2.2 Amorphous silicon

In contrast to the other materials described in this section, amorphous Si (a-Si:H) is not a dielectric, but has semiconducting properties. It is also traditionally deposited using low temperature (200-300 ℃) PECVD. a-Si:H can be doped both p-type and n-type by adding B- and P-containing precursors like B_2H_6 and PH_3 in the process gases, and has therefore been

used for thin film solar cell applications for many years. Films of a-Si:H can also be used together with c-Si to make heterojunction solar cells, with high cell efficiencies up to 24.7 % demonstrated in production [45]. The main reason for this high efficiency is a large V_{oc} (>700 mV), caused by the excellent chemical passivation of the Si surface by both undoped and doped a-Si:H layers. In heterojunction solar cells a-Si:H layers also provide a good passivation of the metal contacts [32].

The main reason for not using a-Si:H for conventional (screen-printed) c-Si solar cells is the large absorption coefficient (limiting its application on the front side of the cell) and the low thermal stability, meaning that it cannot withstand high temperature processes like contact firing [46].

a-Si:H does not contain any significant fixed charge density and does therefore not provide any field-effect passivation. This also means that the resulting SRV is only normally only weakly dependent on the injection level.

2.5.2.3 Thermal silicon oxide

When a Si surface is oxidized, the SiO_2 layer grows into the Si material, meaning that the SiO_2/c-Si interface is formed in a clean region within the original wafer. Because of this fact, thermal oxidation can be used to create a high quality interface with a very low concentration of defects. The high quality of this interface and the excellent dielectric properties of thermal SiO_2 layers are both important prerequisites for the tremendous development of the microelectronics industry over the last 60 years.

Thermally grown SiO_2 was for a long time the state of the art in surface passivation of c-Si solar cells. The passivation properties of the c-Si/SiO_2 interface mainly arise from a high degree of chemical passivation, with a reported density of interface states D_{it} as low as 10^9 $cm^{-2}eV^{-1}$ [47]. Thermal SiO_2 layers may also give a moderate field-effect passivation, caused by positive fixed charges located at the interface, with a typical density in the range $1 - 5 \times 10^{11}$ cm^{-3} [23]. SRV values below 10 cm/s are commonly reported, particularly after a hydrogenation of the interface by e.g. a forming gas anneal [26] [48]. It is therefore not a coincidence that it was this passivation process that was used for the PERL cell made at UNSW, which has the still standing efficiency record for a single junction Si solar cell [45].

However, the high temperatures (~900-1100 °C), and long processing times involved in thermal oxidation can be detrimental for the solar cell device. Specifically, the metal contacts cannot be deposited prior to a high-temperature step as this would degrade the lifetime of the induced carriers and cause the metal to penetrate through the emitter, destroying the pn-junction. Contacting after the high-temperature step usually requires local opening of the oxide, introducing additional processing costs. For a long time the application of thermal oxidation in solar cell processing was therefore limited to lab-scale experiments.

This has partly changed with the recent more widespread of passivated emitter and rear cells (PERC) in industrial production, and thin SiO_2 films have recently also been demonstrated in industrial pilot production [49].

2.5.2.4 Aluminum oxide

Excellent passivation have been demonstrated for Al_2O_3 layers using different deposition methods, including atomic layer deposition (ALD) [50],[51],[52],[53], PECVD [54], atmospheric pressure CVD (APCVD) [55] and sputtering [56]. The degree of stoichiometry typically depends on the deposition system, but the short form Al_2O_3 is used throughout this text for simplicity. The largest difference between Al_2O_3 and the more traditional dielectric layers like a-SiN_x:H is that Al_2O_3 contains a large *negative* charge density [57]. Because of this, p-type substrates passivated by Al_2O_3 have a strong field-effect passivation, with *accumulated* surfaces. This is an important advantage over the inversion layer passivation obtained with positive charges, because the subsurface recombination in the inversion layer is avoided. As described in section 2.3.4, a pronounced injection level dependence of the SRV is normally observed for inverted surfaces at low injection conditions, which has been attributed to recombination in the space charge region below the surface. This injection level dependence is detrimental for solar cells, which typically operate under varying light intensity. In addition to this, the use of an Al_2O_3 passivation scheme also prevents any parasitic shunting of p-type PERC silicon solar cells [58]. The negative charge density of Al_2O_3 also provides the current state of the art passivation on diffused p+-layers like the Al back surface field and B emitters on n-type cells [59]. Because of this, surface passivation by Al_2O_3 is widely considered as the most important advancement in surface passivation of silicon solar cells in recent years.

2.5.2.5 Stacks

In addition to the single layers described above, it is also possible to use stack systems where the properties of the individual layers are combined to achieve improved properties. As an example, the high quality interface of a thin layer of thermal SiO_2 has been successfully combined with the field effect passivation of fixed charges in a-SiN_x:H and Al_2O_3 [23], [60]. Other examples of common stack systems include PECVD silicon oxide and silicon nitride (a-SiO_x:H/a-SiN_x:H) [61],[62], PECVD amorphous silicon and silicon nitride (a-Si:H/a-SiN_x:H) [63], [64],[46], PECVD amorphous silicon and silicon oxide (a-Si:H/a-SiO_x:H) [65], aluminum oxide and PECVD silicon nitride (Al_2O_3/a-SiN_x:H) [66] and aluminum oxide and PECVD silicon oxide (Al_2O_3/a-SiO_x:H) [67].

CHAPTER 3

SIMULATION OF THE SURFACE RECOMBINATION

Computer simulations of the surface recombination velocity (SRV) has been an important tool in this work, both to increase our general understanding of the recombination mechanisms and for interpretation of experimental data. In this chapter, these simulations are described in more detail compared to the treatment in the papers, and the chapter thus serves as an extension to the findings of the articles. The chapter also briefly describes a modification to the simulation program PC1D which was developed and used during the course of this thesis.

The chapter is structured as follows: In section 3.1.1 the practical implementation of the Girisch model introduced in section 2.3.3.1 is described, and in section 3.1.2 the model is used to investigate different aspects of the SRV under surface band bending. Section 3.2 deals with the command line PC1D program and its uses for scripted simulations. In section 3.2.2 the cmd-PC1D program is used to investigate the effect of subsurface defect states.

3.1 SIMULATIONS USING THE GIRISCH MODEL

The Girisch model [16] (section 2.3.3.1) has been used extensively throughout this thesis to analyze experimental measurements of the SRV as a function of injection level (Paper IV) and the surface potential (Papers I, II, and III, and section 5.2.5).

3.1.1 MODEL IMPLEMENTATION

In order to investigate the influence of the various microstructural parameters like Q_f, $D_{it}(E)$ and $\sigma_n(E)/\sigma_p(E)$ on the SRV we have performed simulations using the Girisch model for surface recombination described in section 2.3.3.1. The main part of the simulation is the calculation of the surface potential ψ_s. To determine ψ_s we have followed the approach suggested in the original paper by Girisch et al. [16] and later refined by Aberle et. al. [18]: The different charges throughout the structure (Figure 2.1b) were calculated using Eqs. (2.23), (2.25) and (2.28) for varying values of ψ_s. Using the charge balance in Eq. (2.22), the correct value for ψ_s can then be found from the requirement that the sum $Q_g + Q_f + Q_{it} + Q_{sc}$ should be below a given threshold value. This process is illustrated in Figure 3.1, which shows the different charges as a function of ψ_s, as well as the sum of all charges in the system Q_{tot}. Note that dashed lines are used to indicate negative charge densities on the logarithmic scale. The correct ψ_s is marked at the point where Q_{tot} goes to zero.

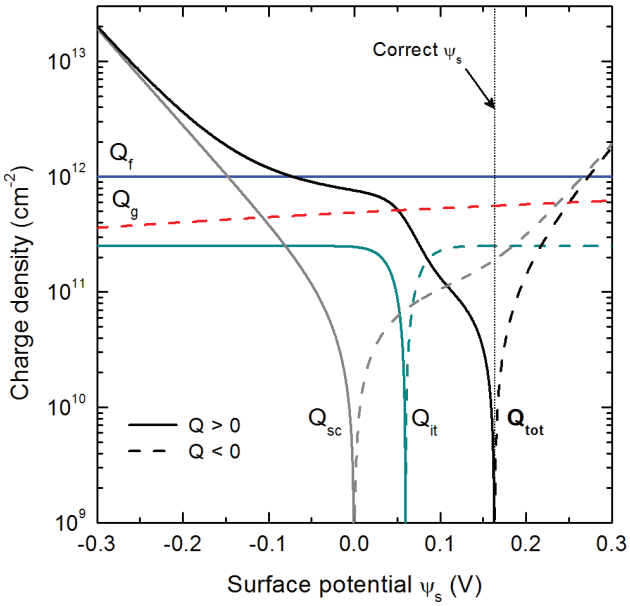

Figure 3.1. Illustration of the different contributions to the charge neutrality in Eq. (2.22) as a function of surface potential for a particular set of conditions. Negative charge density is shown as dashed lines, as it is not possible to present negative data on the vertical log scale. Parameters used for the calculations: $\Delta n = 1 \times 10^{14}$ cm^{-3}, $V_g = -1$ V, $Q_f = 1 \times 10^{12}$ cm^{-2}, $d_i = 100$ nm, $N_A = 5 \times 10^{15}$ cm^{-3}.

From the (given) injection level and the calculated value of ψ_s, n_s and p_s can now easily be calculated using Eqs. (2.18) and (2.21). The surface recombination rate and the surface recombination velocity are then obtained from Eqs. (2.11) and (2.17). Finally, the effective lifetime can be calculated if desired using Eqs. (2.35) and (2.36).

The simulations were performed using Matlab, and the flowchart for the simulation is shown in Figure 3.2. The parameters that were used as input to the model are shown in the first column of the figure.

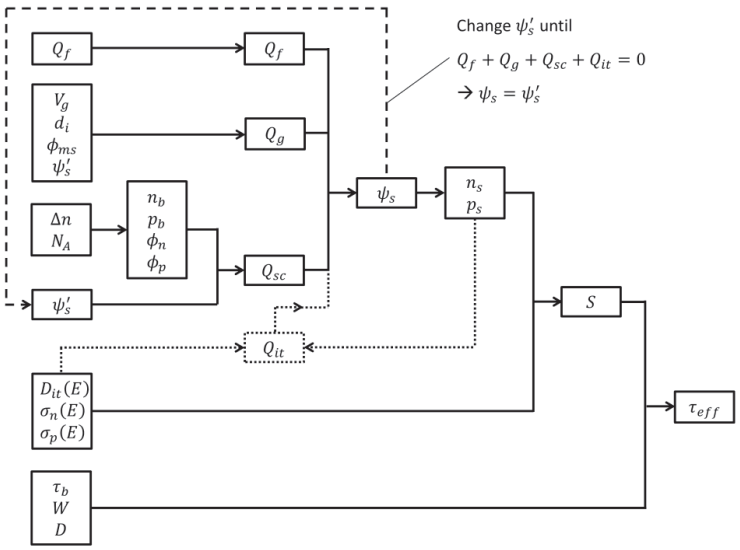

Figure 3.2. Flowchart for the simulation of the SRV and the effective lifetime using the Girisch model. For the simulation shown in the chart we have assumed a p-type sample, that all the fixed insulator charges are located at the interface ($d_f = 0$) and that the interface state charge density Q_{it} can be neglected in the charge balance. See List of symbols on page 106 for parameter definitions.

3.1.2 GENERAL FEATURES OF THE SRV

In this section the Girisch model is used to investigate different aspects of the SRV under surface band bending. The impact of important parameters like Δn, Q_f, V_g, $D_{it}(E)$, σ_n/σ_p on the effective SRV is discussed in order to provide a further understanding of the recombination mechanisms and to illustrate the behavior of the model used for fitting of the experimental data. Related simulations have also previously been performed in Refs. [26] and [17].

3.1.2.1 Impact of energy distribution of interface states

From Eq. (2.11) it can be seen that U_s and S are proportional to D_{it}. The impact of the energy distribution of the interface state density $D_{it}(E)$ is however not straightforward to predict. Figure 3.3 (a) shows the SRV as a function of Δn for six different D_{it} distributions, shown in Figure 3.3 (b), calculated using the Girisch model described in section 2.3.3.1. The distributions have been scaled to give the same SRV of $S = 100$ cm/s at low injection conditions. The total number of interface states is largest for the distributions that have most of the defects close to the band edges, illustrating that the recombination efficiency is largest for defects in the middle of the band gap. From Figure 3.3 (a) it can also be seen that the different distributions have similar behavior for $\Delta n < N_A$, while the slope of the different curves are very different at high injection conditions. For several of the simulations performed in this work the $D_{it}(E)$ distribution was not known. If we make an assumption of e.g. only midgap states or a constant distribution throughout the band gap, we will only make a small error if the injection level is low, while we should be more careful for high injection levels. This is particularly relevant for the simulations of the SRV as a function of gate voltage V_g which is used for analysis of the PL-V measurements presented in section 5.2.5.

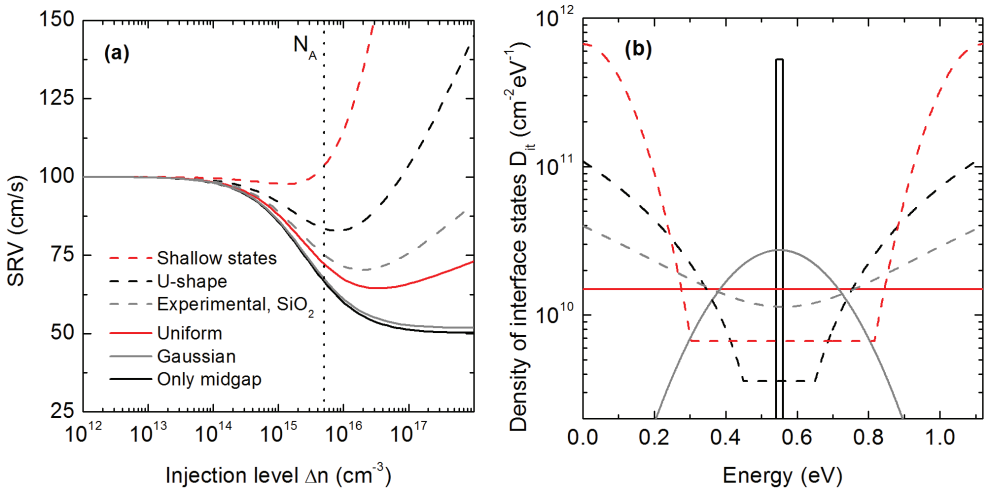

Figure 3.3. Calculated effective SRV as a function of injection level (a) for different interface state distributions $D_{it}(E)$ (b). (The legend in (a) applies to both subfigures). Parameters used for the simulation: $N_A = 5 \times 10^{15}$ cm^{-3}, $Q_f = 0$ cm^{-2}, $\sigma_n = \sigma_p = 10^{-15}$ cm^2, $Q_{it} = 0$.

3.1.2.2 Impact of the surface potential

Figure 3.4 (a) shows the effective SRV as a function of injection level for a p-type sample with different fixed insulator charge densities Q_f, again calculated using the Girisch model (section 2.3.3.1). For the highest injection levels the surface potential goes to zero, regardless of the charge concentration, and the SRV is thus similar for all values of Q_f. At low injection conditions the SRV however depends strongly on the fixed charge density. This behavior is even more clearly understood from Figure 3.4 (b), which shows the SRV as a function of Q_f at different injection levels.

The effect of varying Q_f can be replicated experimentally by depositing corona charges on top of the dielectric layer (section 5.1.2), or by applying a voltage V_g (section 5.1.1 and 5.2). The corresponding voltage for a given film is shown on the top axis of Figure 3.4 (b).

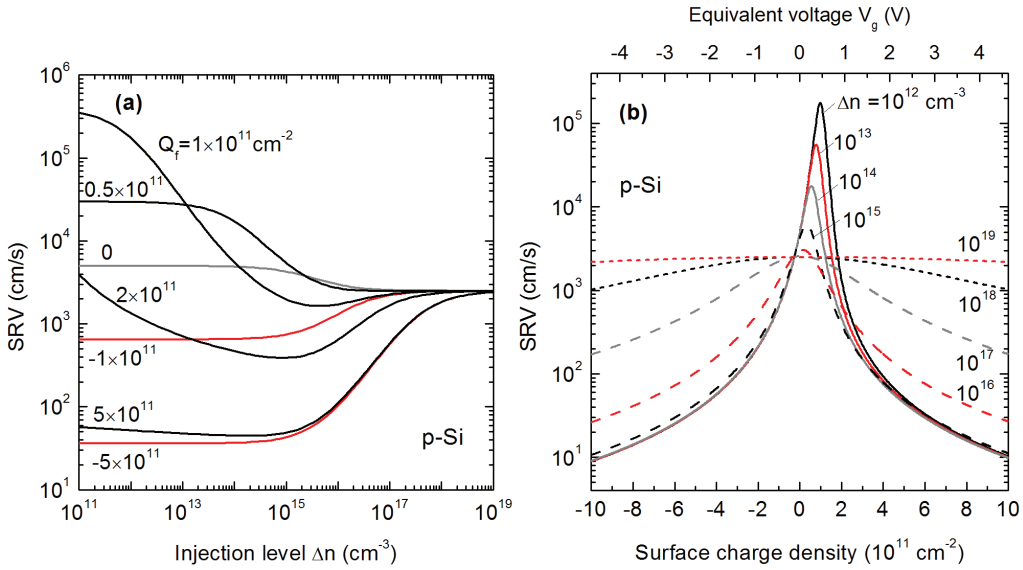

Figure 3.4. (a) Calculated effective SRV as a function of injection level for different values of the fixed insulator charge density Q_f. Black curves are used for $Q_f > 0$, red curves for $Q_f < 0$, grey curve for $Q_f = 0$.

(b) Calculated effective SRV as a function of fixed charge density at different injection levels. The corresponding voltage (top axis) is calculated using $d_i = 100$ nm, $\epsilon_i = 3.9$ and $\Delta\phi_{ms} = 0$ Simulation parameters: $N_A = 5 \times 10^{15}$ cm^{-3}, $\sigma_n = \sigma_p = 10^{-15}$ cm^2, $D_{it} = 5 \times 10^{11}$ cm^{2}eV^{-1} for 0.54 eV $< E < 0.56$ eV (only midgap defects), $Q_{it} = 0$.

For negative Q_f values the concentration of minority carriers (in this case electrons) at the surface is strongly reduced by the electrostatic attraction from the fixed charges. The majority carrier (hole) concentration is correspondingly increased, and this situation is therefore referred to as *accumulation*. Because capture of minority carriers is the limiting process for surface recombination at low injection the SRV is significantly reduced. When Q_f is small and positive (in the order of 1×10^{11} cm^{-2} for normal solar cell doping levels) the majority carrier (hole) concentration at the surface is slightly reduced compared to the flat band case, and we have *depletion* conditions at the surface. The minority carrier concentration however increases and becomes comparable to the majority carrier concentration at the surface. The SRV thus increases strongly as the surface goes into depletion, typically by several orders of magnitude. By examining Eq. (2.11) the maximum SRV can be found to occur when the following condition is met:

$$\frac{n_s}{p_s} = \frac{\sigma_n}{\sigma_p}. \tag{3.1}$$

(For equal capture cross sections this simplifies to $n_s = p_s$). As seen from Figure 3.4 (b) the position of this maximum depends weakly on Δn. If Q_f is increased further after this point the SRV again starts to decrease as we get *inversion* conditions at the surface. For very large positive charge densities the majority carriers are very effectively repelled, and the surface is in strong inversion. In this case the recombination is limited by the availability of holes, even if they are majority carriers in the bulk.

The use of an electric field at the surface to reduce the SRV is referred to as *field-effect passivation*. It is important to note that both positive and negative charges can be used to decrease the SRV, in contrast to the commonly quoted simplified view that negative/positive charges can be used to passivate p-type/n-type material, respectively. Field-effect passivation using accumulation layers at the surface is however normally preferred, as this always causes a reduction in the SRV, while using inversion layers may result in an increased or decreased SRV depending on the charge density and the doping level. In addition, solar cells with rear side passivation employing an accumulation avoids the detrimental effect of parasitic shunting (described in section 2.5.2.1 [44]).

As seen in Figure 3.4 (a) field-effect passivation with both charge polarities causes a strong injection level dependency of the SRV, which may have detrimental effects on solar cell performance at varying excitation conditions [47]. For a moderately high charge density of 5×10^{11} cm^{-2} the SRV increases by approximately two orders of magnitude when going from low injection to high injection conditions, which may be detrimental for solar cells working under high excitation intensities, for instance in concentrated photovoltaics (CPV).

3.1.2.3 Impact of asymmetry in capture cross sections

As previously reported in e.g. Ref. [68], changing the σ_n/σ_p ratio causes only a small shift of the peak in the SRV vs. Q_f curve. A σ_n/σ_p ratio different than 1 however causes a clear asymmetry in the peak, with significant differences in the SRV at accumulation and inversion conditions. Both these effects are shown in Figure 3.5, showing the simulated SRV as a function of surface charge density for different values of the capture cross section for holes.

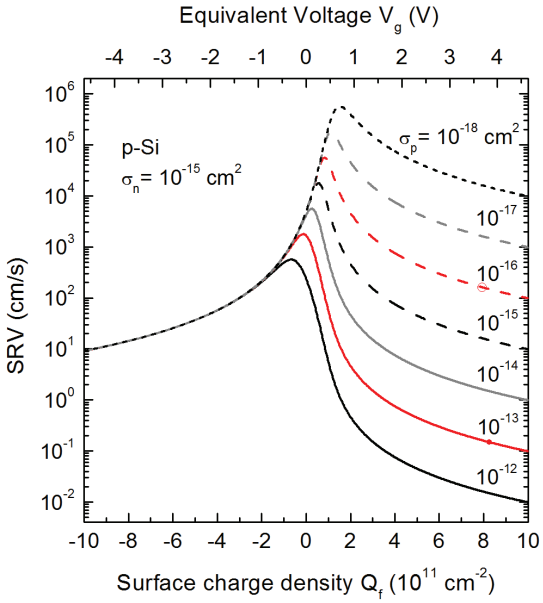

Figure 3.5. Calculated effective SRV as a function of surface charge density for different values of the majority carrier capture cross section σ_p. Parameters used for the simulations: $\sigma_n = 1 \times 10^{-15}$ cm², $N_A = 5 \times 10^{15}$ cm⁻³, $Q_f = 0$ cm⁻², $D_{it} = 5 \times 10^{11}$ cm²eV⁻¹ for 0.54 eV $< E < 0.56$ eV (only midgap defects), $Q_{it} = 0$.

3.2 SCRIPTED PC1D SIMULATIONS

Many of the simulation results presented throughout this work are performed using the semiconductor simulation software PC1D. The program uses a finite-element numerical method for solving the coupled nonlinear equations for carrier generation, recombination and transport in the device and has for many years been the most commonly popular program for simulation of crystalline semiconductor solar cells [69]. The main advantages of PC1D include high calculation speeds, an intuitive user interface and an extensive list of material and physical parameters. However, PC1D has some limitations in that it is

cumbersome to do parameter variations, and additional calculations cannot be implemented directly by running it from within another program.

In the duration of the thesis work we have developed a new version of PC1D called cmd-PC1D which runs from a command line. With scripted simulations we are now able to use PC1D for faster and more advanced analysis with improved resolution, as well as implementing PC1D simulations into other calculations. Throughout this thesis the cmd-pc1d tool has been used for theoretical investigations of surface recombination mechanisms (section 3.2.2), fitting of experimental data (Paper I) and calculations of the impact of surface properties on device performance (Figure 1.3). Note that many of these calculations would have been impractical or impossible using the original PC1D program. This functionality (among other things) has also been implemented into a new graphical user interface named PC1D for Matlab, which was published in Paper VI. The program has been made freely available for download and has attracted many users from the solar cell research community.

We are currently working on a modified version of the cmd-PC1D program that utilizes Fermi-Dirac statistics and several updated, Si-specific models for improved results. Details of this new program will be described in section 6.2.

3.2.1 CALCULATING THE ENERGY BAND STRUCTURE TOWARDS THE SURFACE

The simulations performed in section 3.1 are based on calculations of the surface potential ψ_s. In order to correctly predict the recombination in the subsurface damage region (SDR) it is also necessary to calculate the electrical potential $\psi(x)$, and thus the carrier concentrations (Eq. (2.20)), as a function of depth. This can only be calculated analytically by using strong simplifications [70], and we therefore use the numerical cmd-PC1D program for this purpose. Figure 3.6 (a) and (b) shows the surface band bending and carrier densities, respectively, for a p-type Si wafer with a fixed positive charge density of 1×10^{12} cm^{-2} located at the surface, both at thermal equilibrium and under low injection illumination. In agreement with Figure 3.4 (a) the surface potential is reduced under illumination. For the inverted surface the crossover point with equal concentrations of electrons and holes is observed approximately 250 nm below the surface. If defects are present in this region, the crossover point corresponds to a peak in the SRH recombination rate, as shown in Figure 3.6 (c).

Figure 3.7 shows the calculated surface potential as a function of surface charge density. We find a good correspondence between the results from the Girisch model and the cmd-PC1D program apart from a small difference at the highest charge densities. This deviation corresponds to a difference of ~25% in the resulting surface charge densities, which can also be observed in Fig. 4 in Paper I.

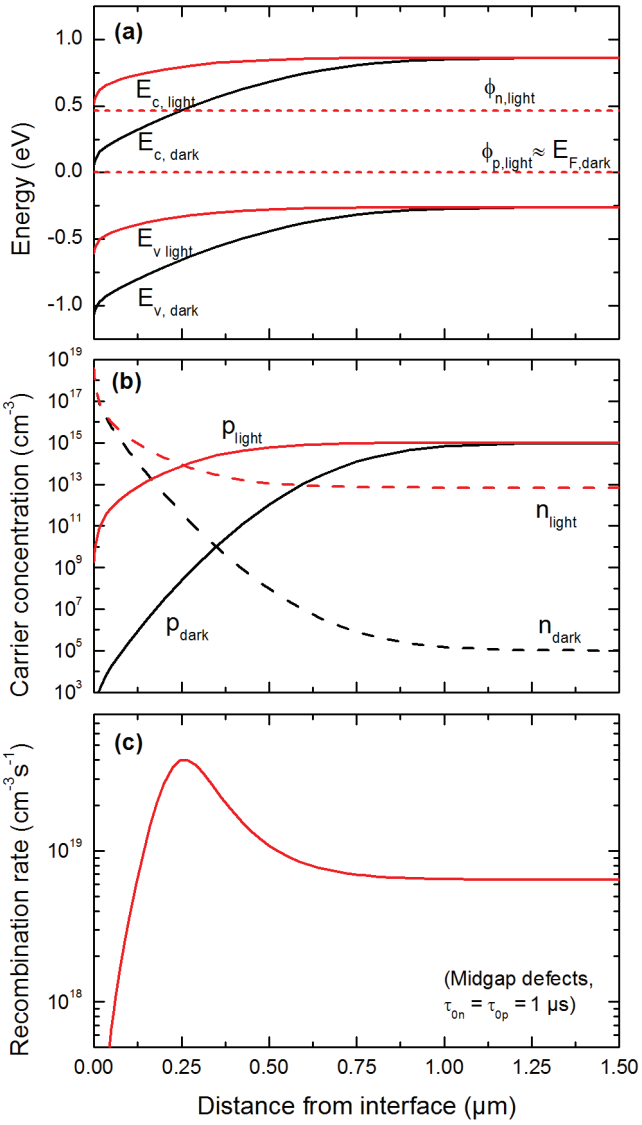

Figure 3.6. (a) Energy band diagram showing the band bending towards a charged Si surface under inversion conditions, both in the dark and under low level illumination, calculated using PC1D. (b) Corresponding carrier densities as a function of depth below the surface. (c) SRH recombination rate caused by from subsurface defects under illumination. The peak in the recombination rate corresponds to the point where $n_{light} = p_{light}$. (Simulation parameters: $Q_f = 1 \times 10^{12}$ cm^{-2}, $N_A = 1 \times 10^{15}$ cm^{-3}, generation rate $G = 1.3 \times 10^{14}$ cm^{-3}s^{-1}).

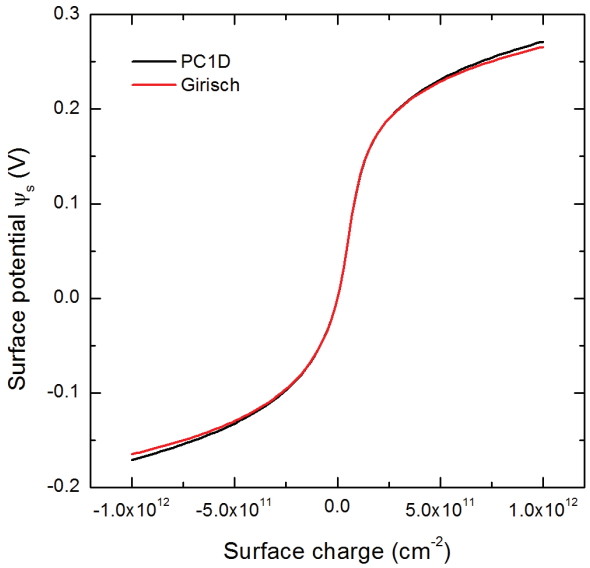

Figure 3.7. Surface potential as a function of charge density at the surface, calculated both using the Girisch model and with PC1D simulations. A small deviation of 3-4 % is observed for large positive and negative charge.

3.2.2 RECOMBINATION AT SUBSURFACE DEFECT STATES

In addition to the interface states described above, recombination-active defects may also be present in the region below the surface. These recombination states may be caused by in-diffusion of impurities or by structural damage. As described in section 2.3.4 the effect of recombination in the SDR is observed as an additional contribution to the SRV. In most previous work on the subject [17],[19] this recombination has been parameterized using the phenomenological parameter J_{02}, as described in section 2.3.4. Eq. (2.30) does however not account for expected difference between the SRV in accumulation and inversion conditions. For the simulations in Paper III, we accounted for this difference by using the following simple parameterization of S_{SDR}:

$$S_{SDR} = \begin{cases} S_{min,n} & \text{for } \psi_s < 0 \\ S_{min,p} & \text{for } \psi_s > 0. \end{cases} \tag{3.2}$$

In this section we will investigate the SDR from a more fundamental point of view, using PC1D simulations performed with the PC1D for Matlab program. The simulation results

will then be used to give a physical justification for Eq. (3.2), which was not included in the paper because of space requirements.

3.2.2.1 Details of the cmd-PC1D simulations

The PC1D simulations of the SDR recombination where performed using a simple model consisting of a p-type wafer with two regions of different bulk lifetime, with parameters given in Table 3.1. The carrier lifetime in the SDR τ_{SDR} is given by the bulk SRH equation (Eq. (2.10)) with the SRH lifetime parameters $\tau_{0n,SDR}$ and $\tau_{0p,SDR}$, which are assumed to be constant for $0 < x < d_{SDR}$.

Figure 3.8 (a) shows the calculated effective lifetime as a function of surface charge density for a wafer with recombination both at the surface (S_{it}) and in the SDR (S_{SDR}), shown together with the carrier concentrations at the surface. In agreement with the results from the Girisch model presented in Figure 3.4 the SRV goes through a maximum at depletion conditions, resulting in a minimum in the effective lifetime at a small positive charge density. The lifetime increases on each side of the minimum, but for large charge densities the curve starts to flatten out as the SRV is increasingly dominated by SDR recombination. As expected the effective lifetime is lowest for inversion conditions (large positive Q_f) but the SDR recombination is also clearly noticeable in strong accumulation (large negative Q_f). Figure 3.8 (b) shows the corresponding SRV as a function of charge density, calculated using Eqs. (2.35) and (2.36). The simulations were also repeated with only interface states and with only subsurface defects, and S_{it} and S_{sdr} are also plotted against Q_f in the figure. The total SRV is observed to be equal to the sum of the two contributions within an error of 5% at each point of the curve, meaning that this approach can be used to successfully investigate the two mechanisms independently. For small Q_f we see that S_{eff} is dominated by S_{it}, whereas $S_{eff} \approx S_{sdr}$ for large Q_f.

Table 3.1. Simulation parameters used for the PC1D simulations presented in Figure 3.8. The recombination in the bulk and at the front surface was set to zero.

Parameter	Symbol	Value	Unit
Subsurface damaged region thickness	d_{SDR}	0.5	µm
Electron/hole lifetime parameter in the SD region	$\tau_{0n,SDR}$, $\tau_{0p,SDR}$	1×10^{-6}	s
Interface SRV parameter for electrons/holes	S_{n0}, S_{p0}	10^4	cm/s
Acceptor doping density	N_A	5×10^{15}	cm^{-3}
Generation rate (long wavelength excitation)	G	1.5×10^{17}	$cm^{-3}s^{-1}$
Total wafer thickness	W	280	µm

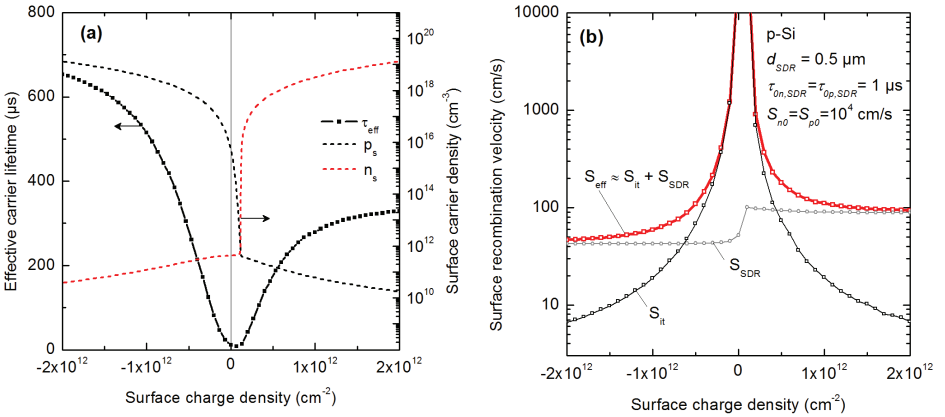

Figure 3.8. Steady state effective lifetime as a function of surface charge density applied to a surface with subsurface defects, calculated using the PC1D for Matlab program (section 3.2). (b) Effective SRV contribution from only subsurface defects S_{sdr} and from only interface states S_{it}, together with the total effective SRV. Simulation parameters are given in Table 3.1.

Furthermore, from Figure 3.8 (b) the S_{SDR} curve can be seen to resemble a step function, which is almost entirely flat in both accumulation and depletion, where it has a significant influence on S_{eff}. We therefore argue that Eq. (3.2) can be used to give a good description of the SDR recombination in a measurement of the SRV with varying surface potential. A similar figure of the SRV contributions, using the Girisch model extended with a SDR contribution, is shown in Figure 5 of Paper III for comparison.

According to the argument above and the curves shown in Figure 3.8, the SRV should be largest for inverted surfaces. For the combination of parameters given in Table 3.1, $S_{min,p}$ (inversion) is found to be approximately a factor of 2 larger than $S_{min,n}$ (accumulation). As we will see in section 5.2.5, this behavior was not always in correspondence with that observed in experiments. This ratio between $S_{min,n}$ and $S_{min,p}$ however depends on several factors, like the thickness of the SDR as compared to the depth of the space charge region (S_{SDR} becomes independent of the band bending for $d_{SDR} \gg d_{sc}$), or the ratio between the capture cross sections for the defects in the SRD, given by $\tau_{0n,SDR}/\tau_{0p,SDR}$. We found that the inversion S_{SDR} is approximately equal the S_{SDR} in accumulation for $\tau_{0n,SDR}/\tau_{0p,SDR} = 0.1$, and that the S_{SDR} can be significantly lower in inversion for small $\tau_{0n,SDR}/\tau_{0p,SDR}$ ratios. The SDR recombination model presented in this section can therefore be used for analyzing SRV vs. band bending curves also under more general conditions. A more thorough discussion of the interpretation of experimental SRV vs. band bending curves are given in section 5.2.5.

CHAPTER 4

EXPERIMENTAL TECHNIQUES

In this chapter the details for sample processing are given, together with a short description of the most important characterization techniques. All the described equipment is installed in the solar cell laboratory at IFE if not stated otherwise. The new photoluminescence imaging under applied bias (PL-V) method developed though this work is presented separately in Chapter 5. For supplementary information see references within each section. In the end of the chapter an overview of the process parameters and key material properties for various materials processed by plasma enhanced chemical vapor deposition (PECVD) are presented.

4.1 SAMPLE PROCESSING

4.1.1 WAFER CLEANING

High quality surface passivation is not only about finding the right surface layer, but also about the purity and morphology of the Si surface prior to processing. The chemistry of Si surface cleaning has been an important topic for the integrated circuit and the process known as the RCA standard clean, developed at Radio Corporation of America in 1965, has been the industry standard for many years [71]. Most of the samples used in this work received a standard RCA clean before subsequent passivation steps, as described in Table 4.1. For PECVD processing, it is also crucial to perform an HF immersion immediately before loading the wafers into the vacuum system. This HF etch removes the native oxide layer and leaves a hydrogen-terminated, hydrophobic (water repellant) surface, creating a suitable and reproducible starting point for the thin film deposition step.

Table 4.1. RCA cleaning sequence used to clean the Si wafers before processing. If necessary, the sample can be stored in a clean environment for a few days/weeks between the RCA2 step and the final HF dip.

Process	Chemicals/ratio	Time/temperature	Purpose
RCA1	H_2O : NH_4OH^* : $H_2O_2^{**}$ / (5:1:1)	15 min, 70℃	Removal of organic contaminants
HF dip	HF, 5%	30 sec, ~25℃	Oxide removal
RCA2	H_2O : HCl^{***} : $H_2O_2^{**}$ / (6:1:1)	10 min, 70℃	Removal of metallic impurities
HF dip	HF, 5%	30 sec, ~25℃	Oxide removal
In between each step:			
Rinse	DI water	1 min ~25℃	Removal of chemicals

Concentrations used in the lab: * 27 % ** 30 % *** 28 %

4.1.2 PLASMA ENHANCED CHEMICAL VAPOR DEPOSITION (PECVD)

Chemical vapor deposition (CVD) is a technique in which gaseous precursor atoms react to deposit a film of a given material onto a substrate. Thermal CVD processes depend on elevated temperatures to obtain any significant reaction rate. In plasma enhanced chemical vapor deposition (PECVD) a large electric field is used to ionize the precursor gases, forming an energetic plasma. The large concentration of free radicals in the plasma means that large deposition rates and low process temperatures (typically below 400°C) are possible. Because of this, PECVD processing is widely used to deposit antireflection coatings and passivation layers in the solar cell industry [26].

The PECVD thin films processed in this work were processed by a PlasmaLab 133 system from Oxford Instruments. This is a lab-scale instrument consisting of a direct parallel plate reactor with an automatic wafer loading system. A schematic illustration of the reactor is shown in Figure 4.1. A radio frequency (RF) electric field is applied between two circular conductive electrodes inside the reactor chamber in order to excite the plasma. Prior to processing, the substrate (Si wafer) is loaded onto the heated bottom electrode by a robot arm, and the precursor gases are injected into the process chamber via a perforated top electrode. The specifications of the instrument are given in Table 4.2.

As with other direct PECVD reactors, the samples are placed between the electrodes within the plasma, meaning that ion bombardment from charged ions being accelerated by the electric field can occur. The effect of the ion bombardment is however minimized by the high plasma frequency of 13.56 MHz, as the acceleration periods (and thus the energy of the ions) are largest at low frequencies.

An overview of PECVD processing parameters and characterization result from different materials processed at the Solar cell laboratory at IFE is given in section 4.5.

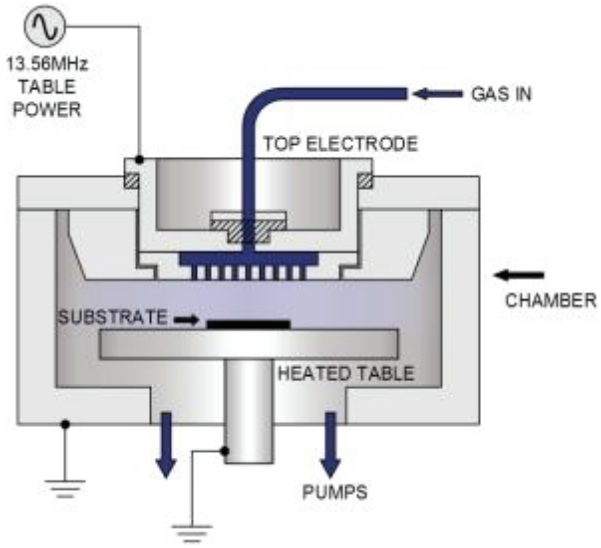

Figure 4.1. Direct-plasma PECVD reactor with parallel plate electrodes. From the Oxford Instruments PlasmaLab 133 instrument manual.

Parameter	Value
RF frequency:	13.56 MHz
RF power:	< 300 W
Pressure:	< 2000 mTorr
Temperature:	< 400℃
Electrode area:	855 cm^2
Gases:	SiH_4, NH_3, N_20, N_2, H_2, B_2H_6, PH_3, Cl_2, Ar, CF_4

Table 4.2. Instrument specifications for the Oxford Instruments Plasmalab 133 PECVD system

4.1.3 THERMAL OXIDATION OF SI

Thermal oxidation of Si wafers is normally performed in a tube furnace consisting of a pure, heated quartz tube with gas flowing through it. Two different chemical reactions are used to form SiO_2 surface layers:

$$Si_{(s)} + O_{2(g)} \rightarrow SiO_{2(s)} \quad \text{(Dry oxidation)}$$

$$Si_{(s)} + 2\,H_2O_{(g)} \rightarrow SiO_{2(s)} + 2H_{2(g)} \quad \text{(Wet oxidation)}$$

In both cases, the oxide grows into the Si by diffusion of oxidizing ions through the existing SiO_2 film. The growth rate is therefore not linear over time, but is proportional to $\sqrt{t}$ for long oxidation times [72].

For the thermal oxide passivation layers examined in Papers II and III we have used a dry oxidation process at 1000 ℃ in a Tempress Systems model TS 8603 tube furnace. Subsequently, selected wafers also received a post-oxidation forming gas anneal (FGA) with 5% H_2 in N_2 at 400 °C for 30 min. This process is used to reduce the interface state density by hydrogen passivation of dangling bonds.

A short description of the passivating properties of thermal SiO_2 layers and their application in Si solar cells is given in section 2.5.2.3

4.1.4 METALLIZATION

Different processing equipment has been used for deposition of metal layers, depending on the desired material and application. In most cases metallized regions have been produced by a Kurt J. Lesker Company NANO 36thermal evaporation system, using a laser processed shadow mask for pattern definition. During thermal evaporation, highly pure metal is melted in a crucible or a boat by the use of a large current passed through a resistive heating element. The sample is mounted over the crucible within a vacuum chamber. Because of the low pressure the metal will gradually evaporate, and the evaporated metal atoms will have a long mean free path within the chamber. A metal film is thus formed on the full interior of the chamber, including on the sample surface. Both Al and Ag layers for contacts and electrodes have been processed by this method during the thesis work.

In addition to this, Al layers have also been processed by radio-frequency magnetron sputtering using a Leybold Optics A550V7 inline sputter system, which has the advantage of large processing area and high film deposition rates. The chamber in the sputtering system is filled with Ar gas at low pressure. An oscillating electric field is then applied to form an Ar plasma, and energetic Ar+ ions are used to sputter atoms off the Al target, which can be deposited on a sample placed on the opposite wall. The sputtering system was primarily used for making contacts to Si wafers, and was used for both rear and front side metallization of the co-planar cell structure discussed in section 6.1.

Al has a high diffusivity and acts as a p-type dopant in Si. It has a relatively low melting point of 660℃ and when heated to moderate temperature it will react with Si forming a conductive interface layer. These properties can be used to make low resistivity contacts to p-type Si. By evaporating or sputtering Al layers and subsequently heating the sample to 450 ℃ for 10 min high quality Ohmic contacts (with linear electrical characteristics) can readily be made.

4.2 CARRIER LIFETIME MEASUREMENTS

Several different methods are commonly employed for determination of the carrier lifetime, most of which rely on measurements of the photoconductance. The conductance can be measured without the need for making contacts to the sample by measuring e.g. the free carrier absorption of infrared light, the reflectance of microwaves, or the current generated in an inductively coupled coil. The coil-based quasi-steady state photoconductance method (QSSPC) and the microwave-detected photoconductance (μ-PCD) method have both been widely used, especially in the field of Si solar cells. In the later years carrier lifetimes have

also been measured by high spatial resolution imaging of the band-to-band photoluminescence (PL). These three techniques are described in sections 4.2.1, 4.2.2 and 4.2.3, respectively.

4.2.1 *QUASI-STEADY STATE PHOTOCONDUCTANCE (QSSPC)*

The quasi-steady state photoconductance (QSSPC) method was first suggested by Sinton and Cuevas [73], and has since then been widely adopted in solar cell characterization labs. In this technique, the excess carrier density is calculated from the conductivity of the sample under illumination, measured by an inductively coupled coil, as shown in Figure 4.2 (a). The excitation intensity is varied over time by the use of a flash, and the lifetime can therefore be measured as a function of injection level in a single, fast measurement. In the first version of the setup it was required that the time constant of the flash decay was much longer than the carrier lifetime in the material, meaning that the excess carrier density is approximately in steady state at each point of the measurement (hence the name quasi-steady state). Later, Nagel et al. [74] published a generalized analysis to allow for measurements of longer carrier lifetimes, in the same range or larger than the decay constant of the flash. This generalized analysis is used for all measurements presented in this work.

The starting point for the general analysis is the time evaluation of the carrier density, given by

$$\frac{d\Delta n(t)}{dt} = G(t) - U(t) + \frac{1}{q}\nabla J \tag{4.1}$$

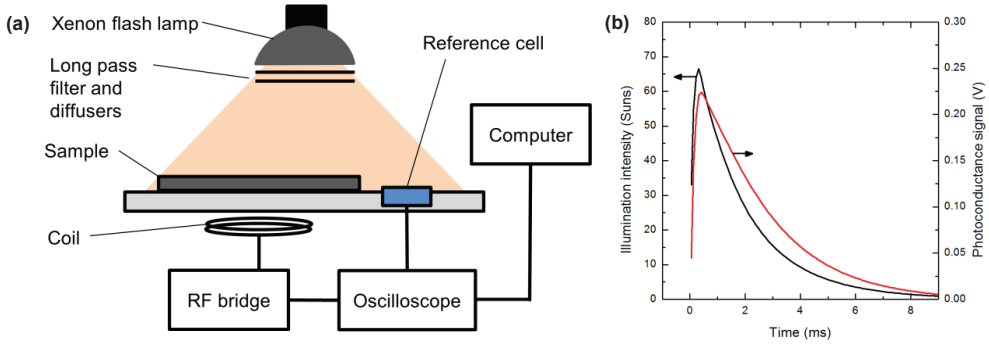

Figure 4.2. (a) Schematic illustration of the Sinton WCT-100 inductively coupled photoconductance measurement setup used for the QSSPC measurements. (b) Typical raw measurement data of photoconductance and illumination intensity used to calculate $\Delta n(t)$ and $G(t)$ in Eq. (4.2).

The Sinton QSSPC setup uses a Xenon flash with a long pass filter as the excitation source to ensure a homogeneous generation throughout the wafer, the gradient in the current density ∇J can therefore be set to zero with a small error, and the other quantities are taken as depth-averaged values. By inserting the relation between the recombination rate and the effective lifetime $U = \Delta n/\tau_{eff}$ from Eq. (2.1) and solving for τ_{eff} we get

$$\tau_{eff} = \frac{\Delta n(t)}{G(t) - \frac{d\Delta n(t)}{dt}}. \tag{4.2}$$

To measure τ_{eff} it is thus necessary to measure both the injection level and the generation rate in the wafer as a function of time, as shown in Figure 4.2 (b). In the Sinton WCT-100 lifetime tester the generation rate is measured as

$$G(t) = OC \times \frac{I_{ref}(t)}{qW_{ref}} \tag{4.3}$$

where I_{ref} is the generated photocurrent measured by a small reference solar cell placed on the sample stage and OC is the so-called optical constant determined by the optical properties of the sample as compared to the reference diode. (Correct values for OC can be found for a range of different surface coatings in the Sinton WCT-100 manual. A calculation of the OC has also been incorporated in the PC1D for Matlab program described in Paper VI.

The injection level is determined simultaneously from the measured excess conductivity in the sample $\Delta\sigma$ as

$$\Delta n(t) = \frac{\Delta\sigma(t)}{q(\mu_n + \mu_p)W}, \tag{4.4}$$

where μ_n and μ_p are the electron and hole mobilities and W is the wafer thickness. Finally, the effective lifetime at each injection level is calculated using Eq. (4.2).

4.2.2 *MICROWAVE DETECTED PHOTOCONDUCTANCE DECAY (μPCD)*

The microwave detected photoconductance decay method utilizes a very short (~200 ns) light pulse from a near-infrared laser source to illuminate a small area (~1 mm^2) of the wafer, generating excess carriers. The transient in the increased photoconductivity arising from these carriers is then monitored by measuring the change of the microwave reflectivity of the sample over time [75]. In contrast to QSSPC, the μPCD technique has the ability to scan the measurement probe over the sample, thus creating lifetime maps with high spatial resolution. A simplified illustration of the μPCD measurement setup is shown in Figure 4.3 (a).

Because the generation rate G is zero throughout the duration of the decay, Eq. (4.2) is simplified to

$$\tau_{eff} = -\frac{\Delta n(t)}{\frac{d\Delta n(t)}{dt}}. \tag{4.5}$$

This differential equation in Δn has solutions on the form $\Delta n(t) = A \times \exp(-t/\tau_{eff})$. The transient nature of the technique gives the advantage that no absolute measurement of the carrier density or the generation rate is needed; as long as τ_{eff} is not changing throughout the transient, it can be extracted by fitting a single exponential function to the measured decay. For most measurement conditions τ_{eff} is however dependent on Δn, so that the decay constant of the measured curve is not well defined. Also, no information about the injection level is obtained. Even though a Semilab WC-2000 µPCD system has been available for this work, the PL imaging technique described below has been preferred for lifetime image measurements, because of the well-defined measurement conditions and short measurement times (~1 s as compared to ~1 hour for µPCD).

Newer µPCD instruments like the Semilab PV-2000 setup used for the measurements in Paper II utilizes a variable, large area bias light to set the injection level in the sample [76]. The excess conductivity transient created by the laser source can then be treated as a small perturbation of the total photoconductivity, so that the injection level is well-defined and constant throughout the whole decay. By scanning the intensity of the bias light as shown in Figure 4.3 (b) τ_{eff} can be measured as a function of Δn, and this method is referred to as quasi-steady state µPCD (QSS-µPCD). A comparison between QSS-µPCD and QSSPC measurements on the thermally oxidized samples is shown in Figure 2 in Paper II.

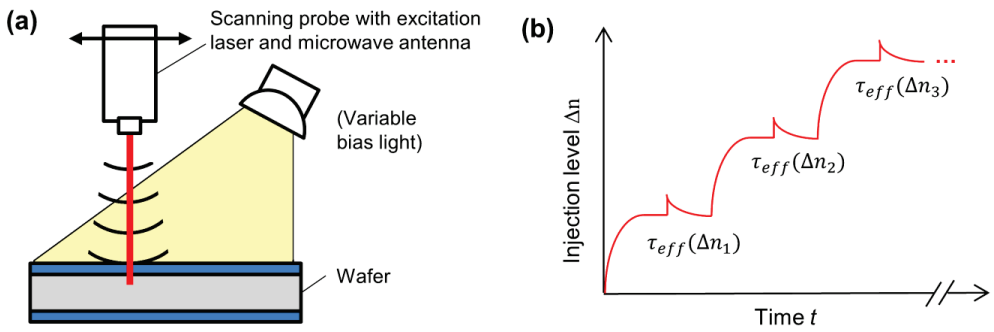

Figure 4.3. (a) Schematic illustration of the µPCD measurement setup (b) Illustration of the principles behind the small perturbation QSS-µPCD measurement.

4.2.3 PHOTOLUMINESCENCE IMAGING (PL-I)

Camera-based photoluminescence imaging (PL-I) has in recent years become a widely used technique for characterization of crystalline silicon wafers and solar cells [77], [78]. The technique provides a fast way of measuring the quality of Si wafers with high spatial resolution. Also, because the method is contactless and non-destructive, measurements can be performed at almost any stage of solar cell production, thus making it a useful tool for process control and even in-line inspection [79]. A schematic illustration of the measurement setup is given in Figure 4.4 below.

The main physical principle underlying the technique is radiative recombination, where a conduction band electron and a valence band hole recombine, releasing the energy as a photon (see section 2.2.1). When the excess carriers are generated optically, this process is referred to as *photoluminescence* (PL). Because each recombination event produces one photon, the PL emission rate Φ_{PL} is equal to the rate of radiative recombination (Eq. (2.2))

$$\Phi_{PL} = B_{rad}\left(np - n_i^2\right), \tag{4.6}$$

where B_{rad} is the radiative recombination coefficient. For moderately doped p-type material we can insert $p = N_A + \Delta n$ and $n = \Delta n$ for the carrier concentrations. Also, the term n_i^2 can be safely omitted for most doping and injection conditions. The measured intensity I_{PL} can then be written as

$$I_{PL} = C_{cal}B_{rad}(N_A + \Delta n)\Delta n = C_{cal}B_{rad}N_A\Delta n + C_{cal}B_{rad}\Delta n^2, \tag{4.7}$$

where C is an instrument- and sample specific constant describing the fraction of the emitted light which is detected by the camera. The injection level Δn can be calculated from the measured intensity at each point as the solution of the quadratic equation in Eq. (4.7):

$$\Delta n(x,y) = \sqrt{\left(\frac{N_A}{2}\right)^2 + \frac{I_{PL}(x,y)}{C_{cal}B_{rad}}} - \frac{N_A}{2} \tag{4.8}$$

For low injection conditions we can avoid the quadratic term by setting $p = N_A$. In this case the injection level is simply proportional to the measured intensity:

$$\Delta n(x,y) = \left(\frac{1}{C_{cal}B_{rad}N_A}\right) \times I_{PL}(x,y) \tag{4.9}$$

The PL image is measured at steady state conditions, so the effective lifetime can be obtained from the injection level as

$$\tau_{eff}(x,y) = \frac{\Delta n(x,y)}{G} = \frac{\Delta n(x,y)}{\left(1 - R_f\right)\Phi_{\mathrm{ph}}/W}. \tag{4.10}$$

where G is the generation rate, R_f is the front reflectance and Φ_{ph} is the photon flux from the excitation source.

Initially, PL images were published in arbitrary units [80]. Such raw PL images are useful for investigation of relative variations over the wafer, but do not give any absolute measure of the lifetime in the material. On the other hand, if the calibration constant C_{cal} is known, equations (4.7)-(4.10) can be used to calculate the effective lifetime at each point of the image. In most PL imaging setups C_{cal} is calculated by an integrated photoconductance measurement using an inductively-coupled coil [81]. The BT imaging LIS-R1 setup used in this work employs an integrated Sinton QSSPC stage (as described in section 4.2) for this purpose. From the measured lifetime vs. injection level curve the point corresponding to the correct generation rate is calculated. C_{cal} is then calculated by comparing the injection level at the calibration point Δn_{cal} to the PL intensity in the region above the coil $I_{PL,cal}$:

$$C_{cal} = \frac{I_{PL,cal}}{B_{rad}(N_A \Delta n_{cal} + \Delta n_{cal}^2)} \tag{4.11}$$

For the general calibration procedure both B_{rad} and the doping concentration of the sample have to be known. Under low injection conditions Eq. (4.9) can be used instead, thus removing this restriction. Correct quantification of the QSSPC measurement also requires knowledge of thickness of the sample and the front side reflectance at the excitation wavelength ($\lambda = 808$ nm).

The calibration method described above only requires steady state measurements of the PL intensity, and is the most common way of relating the measured signal to Δn and thus τ_{eff}. By taking advantage of the time-domain it is also possible to measure Δn without the need for a secondary photoconductance measurement. In the so-called quasi-steady state photoluminescence (QSSPL) method [82], the PL intensity in a small region is measured as a function of time as the generation rate is gradually varied. The injection dependent effective lifetime is then calculated from the two curves $G(t)$ and $I_{PL}(t)$ in an equivalent manner to the procedure described in section 4.2. The calibration constant C_{cal} in Eq. (4.7) is determined using a self-consistent lifetime calibration technique presented by Trupke et al. [83], by minimizing the hysteresis of the trajectory

$$\tau_{eff}\left(\Delta n(t)\right) = \frac{\Delta n(t)}{G(t) - \frac{d\Delta n(t)}{dt}}. \tag{4.12}$$

The QSSPL technique has the additional advantage of being able to measure effective lifetimes at very low injection levels without influence of carrier trapping, which typically is a problem for techniques based on photoconductance measurements. Also, no knowledge of carrier mobilities are necessary, simplifying measurements on e.g. heavily compensated Si wafers.

A different approach for calibration of the PL images has been proposed by Kiliani et al. [84], in which a rotating shutter wheel is used to modulate the camera signal. The excitation source is also turned on and off periodically with the same period as the shutter rotation, and the PL intensity transient is recorded by the camera. The effective lifetime is then calculated by analyzing this transient at each pixel, and a lifetime map is constructed. This method is less sensitive to lateral inhomogeneities as it does not rely on the use of a universal calibration constant for the whole image. Also no knowledge of the doping or the optical properties of the sample are necessary. The method is however limited to measurements under low-injection conditions, and is typically more time consuming than calibrated steady state measurements (1-5 minutes per measurement).

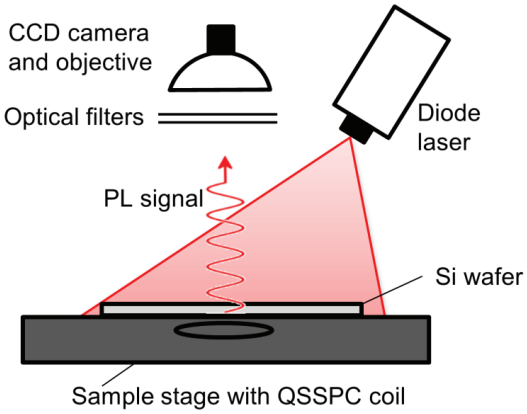

Figure 4.4. (a) Illustration of the PL imaging equipment. A defocused diode laser is used to inject carriers homogeneously over the wafer. The emitted PL light is then detected by a Si CCD camera, with a resolution down to 23 µm.

4.3 ELECTRICAL CHARACTERIZATION OF MIS STRUCTURES

4.3.1 CAPACITANCE-VOLTAGE (C-V)

The charge density in a dielectric thin film on a semiconductor substrate can be determined by capacitance-voltage measurement of metal-insulator-semiconductor (MIS) capacitors. In this work a Keithley 4200-SCS semiconductor characterization system has been used for this purpose. The details of this technique are well covered in various textbooks on semiconductor characterization [7],[85] and this section will therefore be limited to providing a summary of the analysis presented in Ref. [7]. A schematic illustration of the MIS structures is shown in Figure 4.5 (a), and the energy band diagram is shown in Figure 2.1.

The (area-specific) capacitance is normally given in units of F/cm^2 and is defined as

$$C = q\frac{dQ_g}{dV_g}, \tag{4.13}$$

where Q_g is the charge (in elementary charges per area) and V_g is voltage of the gate electrode. During the capacitance measurement a small AC voltage is applied to the MIS structure, and the resulting charge variation is measured from the current I, defined as the change in the charge per time $I = dQ_g/dt$. The total charge in the MIS structure must be zero, so the gate charge is balanced by the insulator fixed charges Q_f, the charges at the interface states Q_{it} and the induced charge in the space charge region of the semiconductor Q_{sc}, as described in Eq. (2.22).

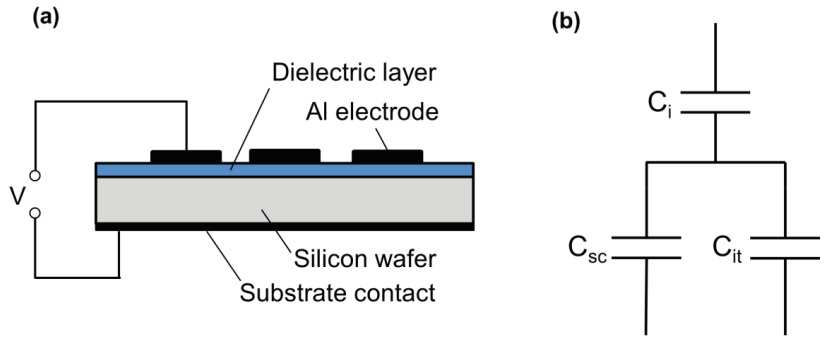

Figure 4.5. (a) Schematic illustration of the MIS structure used for the C-V measurements. (b) Equivalent circuit of the MIS structure.

The gate voltage is partially dropped over the insulator and partially over the space charge region in the semiconductor:

$$V_g = V_{fb} + V_i + \psi_s, \tag{4.14}$$

where V_{fb} is the flat band voltage. The equivalent circuit of the MIS structure is shown in Figure 4.5 (b), with the insulator capacitance C_i in series with a parallel connection of the capacitance of the space charge region C_{sc} and the capacitance associated with the interface states C_{it}. The total capacitance is then given by

$$C = \frac{1}{\frac{1}{C_i} + \frac{1}{C_{sc} + C_{it}}} = \frac{C_i(C_{sc} + C_{it})}{C_i + C_{sc} + C_{it}}. \tag{4.15}$$

A typical high-frequency C-V curve measured on a p-type sample is shown in Figure 4.6. In order to understand the shape of the curve and the information that can be extracted from it a few limiting cases are considered: For large negative voltage the Si surface is heavily accumulated, and C_{sc} is very high, approaching a short circuit (the large hole concentration at the surface act as the second electrode), and the total capacitance is simply $C = C_i$.

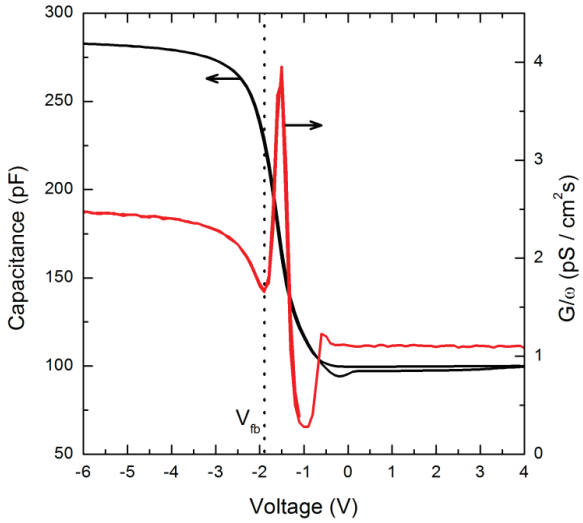

Figure 4.6. Capacitance (left axis) and conductance (right axis) vs. voltage curves, measured on a MIS structure with a thermal oxide dielectric layer at a frequency of $f = 100$ kHz. The shift of the C-V curve with respect to the ideal curve can be used to determine the flatband voltage V_{fb}(dashed, vertical line) and thus also Q_f. The height of the conductance peak can be used to determine the D_{it} at a certain position in the band gap.

For small positive voltages the surface is depleted, and C is given by the total capacitance over the insulator and the width of the space charge region d_{sc}, given in Eq. (4.15). The fact that the depletion capacitance is lower than in accumulation can be understood by the inverse relation of the capacitance per area and the thickness in a parallel plate capacitor, $C = \epsilon_0\epsilon_i/d$. In strong inversion the measured capacitance depends on the ac frequency of the probing signal. If the frequency is low enough so that the inversion charge is able to follow the applied voltage the capacitance is reduced to C_i. When the inversion layer charge is unable to follow the ac voltage the equivalent circuit is reduced to a series connection of C_i and C_{sc}, with $C_{sc} = \epsilon_{Si}\epsilon_0/d_{sc}$. C-V measurements are most easily analyzed in the high frequency limit, and this is also the case for the experiments presented in this work.

4.3.1.1 Measurements of the fixed charge density

The main motivation for measuring high frequency C-V curves in this work is to obtain precise measurements of the fixed charge density. Q_f can be determined by measuring the shift in experimental C-V curve along the voltage axis as compared to a theoretical C-V curve. This shift is caused by a combination of the insulator charges and the difference between the metal and semiconductor work functions $\Delta\phi_{ms}$. The voltage shift is normally measured at the flatband capacitance C_{fb}, which is the (known) capacitance at which there are no band bending in the semiconductor, i.e. the bands are flat. The voltage required to obtain these conditions are then called the *flatband voltage* V_{fb}. The flatband capacitance C_{fb} can be calculated from Eq. (4.15), with C_{sc} set equal to $C_{sc,fb}$, the space charge region capacitance per unit area at flat band conditions [7]:

$$C_{sc,fb} = \frac{\epsilon_{Si}\epsilon_0}{L_D}. \tag{4.16}$$

Here L_D is the Debye-length, defined for p-type material as

$$L_D = \sqrt{\frac{k_B T \epsilon_{Si}\epsilon_0}{q^2 N_A}}. \tag{4.17}$$

Q_f can then be calculated from the charge neutrality of the system, given in Eq. (2.22), by inserting V_{fb} in Eq. (2.23) and setting $Q_{sc} = 0$ and $\psi_s = 0$, which apply under flatband conditions. Q_f is then given by

$$Q_f = \frac{\frac{C_i}{q}\left(\Delta\phi_{ms} - V_{fb}\right) - Q_{it}}{1 - C_i d_f/2\epsilon_i}. \tag{4.18}$$

If we assume that the charge associated with the interface states Q_{it} are negligible compared to Q_f and that the fixed charges are located at the insulator/semiconductor interface ($d_f = 0$) the expression is simplified to

$$Q_f = \frac{C_i}{q}(\Delta\phi_{ms} - V_{fb}). \tag{4.19}$$

As in section 2.3.3.1, $\Delta\phi_{ms}$ was calculated from Eq. (2.24), using a metal work function F_m for Al of 4.1 eV and an electron affinity for Si χ_{Si} of 4.05 eV.

4.3.2 *CONDUCTANCE MEASUREMENTS*

The conductance method is an electrical characterization method for determination of D_{it}. Measurements are performed on MIS capacitor structures using the same experimental setup as for C-V measurements. Capture and emission of carriers in the traps increase the AC-conductivity of the structure; hence conductance is a measure of the density of interface states [85]. Experimentally, D_{it} can be found by applying a voltage to keep the semiconductor in depletion and measuring the equivalent parallel conductance G_p as a function of frequency. Plotting G_p/ω (where ω is the angular frequency) versus frequency produces a maximum value, which is related to the D_{it} in a specific part of the band gap. Alternatively, the peak conductance can be extracted from conductance-voltage plots, as shown in Figure 4.6. This method was used for determination of D_{it} for different a-SiN_x:H films in Paper IV.

4.4 COMPLEMENTARY CHARACTERIZATION METHODS

4.4.1 *VARIABLE ANGLE SPECTROSCOPIC ELLIPSOMETRY*

Ellipsometry is the study of changes in the polarization of light after reflection from a surface. The technique is widely used to measure the thickness and optical properties of a sample, and is particularly useful for investigation of thin films [86]. The ellipsometry measurements in this work were performed using a variable angle spectroscopic ellipsometer (VASE) from J. A. Woollam Co., Inc. In this setup light from a Xenon arc lamp is passed through a monocromator to select the desired wavelength and through a polarizer and a retarder in order to polarize it to a known state. The light is then reflected from the sample (specular reflection is necessary) and passed onto a detector with a polarization analyzer and a detector. A schematic illustration of the instrument setup is shown in Figure 4.7.

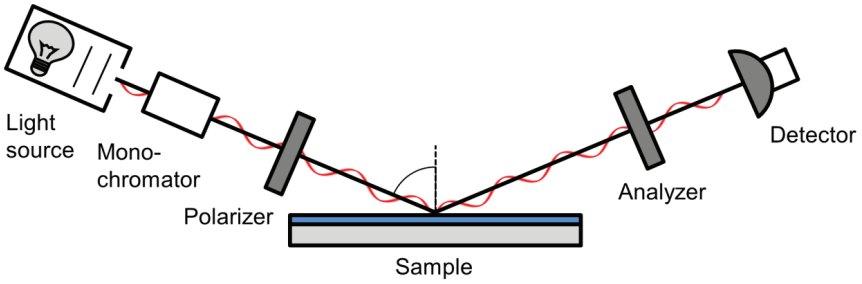

Figure 4.7. Schematic illustration of the variable angle spectroscopic ellipsometry (VASE) setup.

The component of the incident polarized light which is parallel to the sample surface (s-plane) is reflected differently than the component which is polarized normal to the surface (p-plane). The ratio between the s-plane reflectance R_s and the p-plane reflectance R_p is related to the so-called ellipsometric parameters Ψ and Δ by

$$\frac{R_p}{R_s} = \tan(\Psi)\, e^{i\Delta}. \tag{4.20}$$

By measuring Ψ and Δ as a function of both wavelength and incoming angle it is possible to extract accurate information about the thicknesses and optical properties of both single- and multilayer films. The analysis is performed by fitting the experimental data to a model of the structure that is being measured, using different parameterizations for the dispersion relationships $n(\lambda)$ and $k(\lambda)$. The accuracy of the measurement thus depends both on the physical properties of the instrument and on the quality and correctness of the optical model that is being used.

4.4.2 *FOURIER TRANSFORM INFRARED SPECTROSCOPY (FTIR)*

Infrared (IR) spectroscopy is the study of the interaction between IR light and matter. It covers a range of techniques, the most common being absorption spectroscopy, which exploits the fact that chemical bonds absorb radiation at specific frequencies that are characteristic of their nature and chemical environment. IR spectroscopy can therefore be used to investigate the chemical composition of a sample. In a Fourier transform infrared spectroscopy (FTIR) instrument an interferometer is used to measure all the wavelengths of the spectrum simultaneously, without the need for a monocromator. FTIR measurements have many applications in material science, among others it can be used to determine the bond densities in thin amorphous films. FTIR measurements were performed on a Bruker IFS

113-v spectrometer located at MiNaLab at the University of Oslo, and used in Paper IV to investigate the stoichiometry and hydrogen concentration in our PECVD a-SiN_x:H. layers.

4.4.3 *SOLAR CELL CHARACTERIZATION*

In addition to surface passivation, this thesis also deals to some extent with the impact of surface recombination and rear electric fields on solar cell performance (see section 6.1 for details). A complete discussion of solar cell operation and electrical characterization of solar cells is beyond the scope of this text. Interested readers are instead referred to one of several good textbooks on the topic, e.g. Refs. [29], [87]–[89]. This section will therefore be limited to a short technical description of the instruments that have been used.

Current-voltage (I-V) measurements of solar cells were performed in a Wacom Solar Simulator Model WXS-150-10 AM 1.5, using a Model STG-200VPXYZ water cooled sample stage. The cells were illuminated with a xenon lamp with intensity equivalent to one sun (100 mW/cm2, AM 1.5). Wavelength dependent reflectance and quantum efficiency measurements were performed in a LOANA system from PVTools.

4.5 OVERVIEW OF PECVD PASSIVATION MATERIALS

PECVD layers are used for different purposes in solar cell processing, with the now standard a-SiN_x:H antireflection coatings (ARCs) being the most important example. In addition to the simulations and experiments presented in the papers and in chapters 3 and 5, a large part of this PhD work has been devoted to the development and use of different PECVD processes. We have developed and optimized processes for double-layer ARCs (as described in Paper V), for etching and metallization barriers and for surface passivation, using the PECVD thin film deposition systems described in section 4.1.2.

A good surface passivation process is useful in order to reduce recombination losses in solar cell devices. However, good surface passivation is also critical for accurate measurements of the bulk lifetime of c-Si wafers and slabs. The optimal surface passivation structure should exhibit as low SRV as possible, but should also be stable over time and be able to withstand subsequent heat treatment steps. PECVD processing parameters for a selection of passivation layers commonly used in the Solar cell laboratory at IFE are listed in Table 4.3, together with the measured growth rates and optical properties of each layer. The thickness and wavelength-dependent refractive index and absorption coefficient of each layer was measured using variable angle spectroscopic ellipsometry, as described in section 4.4.1.

Measured results from different single- and double layer passivation structures are given in Table 4.4. The reported effective carrier lifetimes were measured on ~280 μm thick

double side polished (100)-oriented 3 Ωcm FZ wafers with a high bulk lifetime, RCA cleaned (section 4.1.1) and passivated symmetrically on both sides. The best passivation results have been obtained by a 20 nm a-Si:H film with a 100 nm thick a-SiN_x:H capping layer deposited at low temperature. As shown in Figure 4.8, this structure was used to achieve effective lifetimes up to 12.5 ms on n-type wafers, and up to 5.3 ms on p-type wafers. This corresponds to a maximum SRV (assuming infinite bulk lifetime) of 1.1 cm/s and 2.6 cm/s, respectively. Single layer a-Si:H films also show excellent passivation properties, particularly after a 1 min subsequent anneal at 450 ℃. The capping layer however provides additional scratch protection and improves the thermal and temporal stability of the passivation quality. Also, because of the longer process time at elevated temperatures the need for an additional annealing step is eliminated. This PECVD a-Si:H/a-SiN_x:H stack has been used as a rear side passivation layer for the cell structure described in section 6.1.

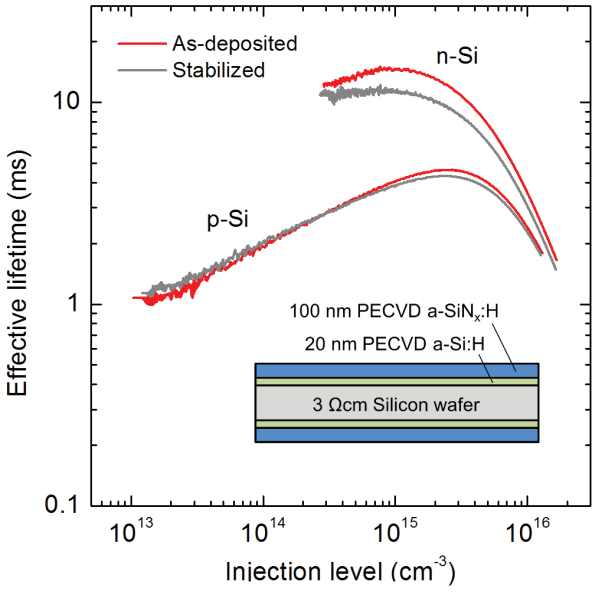

Figure 4.8. QSSPC curves showing the effective lifetime vs. injection level Δn for n-type and p-type FZ wafers passivated by a stack of PECVD a-Si:H/a-SiN_x:H. Deposition parameters are given in Table 4.3.

Table 4.3. Typical PECVD processing parameters (top) and measured growth rates and refractive index (bottom) for selected passivation layers processed in the Solar cell laboratory at IFE

		a-SiN_x:H, (Std.)	a-SiN_x:H, (High n)	a-SiN_x:H (Low T)	a-Si:H	a-SiO_xN_y:H	a-AlO_x
Deposition parameters:							
Temperature	℃	400	400	200	230	130	380
Power density[2]	mW/cm^2	46.8	46.8	46.8	9.4	58.5	23.4
Chamber pressure	mTorr	800	800	800	300	500	400
SiH_4 flow	sccm	20	50	20	25	45	0
NH_3 flow	sccm	20	20	20	0	0	0
N_2 flow	sccm	980	950	980	0	20	0
N_2O flow	sccm	0	0	0	0	0	1000
TMA[3] flow	sccm	0	0	0	0	0	8
Measured film properties:							
Growth rate	nm/min	14.2	17.1	19.0	8.0	41	~15
Refractive index[4]		2.04	2.51	1.89	4.2	1.8	1.6

Table 4.4. Best passivation results and fixed charge density of different PECVD layers processed in the Solar cell laboratory at IFE. The maximum SRV values are calculated from Eq. (2.35) and (2.36) assuming an infinite bulk lifetime.

Passivation structure	p-type			n-type		
	τ_{eff} (µs)	S_{max} (cm/s)	Q_f (C-V) (cm^{-2})	$\tau_{eff}{}^*$ (µs)	S_{max} (cm/s)	Q_f (C-V) (cm^{-2})
a-SiN_x:H (Std) + firing[5]	210	72	$7-8\times10^{11}$	370	41	$7-8\times10^{11}$
a-SiN_x:H (High n) + firing[5]	320	50	?	440	32	?
a-Si:H + annealing[6]	3300	4.5	-	4700	3.2	-
a-Si:H + a-SiN_x:H (Low T)	5300	2.8	-	12500	1.2	-
a-SiO_xN_y:H + a-SiN_x:H (Std) + firing[5]	2230	6.3	$1-2\times10^{12}$	3200	4.4	$1-2\times10^{12}$
a-AlO_x + a-SiN_x:H (Std) + firing[5]	200	45	$\sim-1\times10^{12}$	600	15	$\sim-1\times10^{12}$

[2]Electrode area = 855 cm^2. [3]Trimethylaluminium [4]Measured at $\lambda = 630$ nm
[5]Std. contact firing process, IR heated belt furnace. Total time 9 s, peak temperature 810 °C **
[6]Belt furnace, 450℃ for 1 min

CHAPTER 5

PHOTOLUMINESCENCE IMAGING UNDER APPLIED BIAS (PL-V)

The surface recombination velocity (SRV) at a passivated Si surface can be assessed from carrier lifetime measurements if the bulk lifetime is known, using Eqs. (2.35) and (2.36). By modulating the surface band bending at the semiconductor-insulator interface it is possible to substantially change the carrier concentrations at the surface and thus also the SRV, as described in section 2.3.3. It is therefore interesting to be able to controllably change the surface potential during lifetime experiments. One of the major contributions of this thesis is the development of a new approach to this type of measurements, using a MIS structure in combination with a PL imaging setup. The new method has been named photoluminescence imaging under applied bias, abbreviated PL-V. Before going into the details of these measurements we will first describe the currently used techniques for modulation of the surface potential. This previous work is described in section 5.1. In section 5.2 the details, advantages and limitations of the PL-V method are described. At the end of the chapter (section 5.2.5), a selection of measurements performed on different passivation materials is presented, together with an analysis of the experimental results by comparison with the simulations, as described in Chapter 3.

5.1 PREVIOUS WORK ON CONTROLLING THE SURFACE POTENTIAL

Two main principles are used for measurements of the effective lifetime (and thus the SRV) at different surface band bending conditions. The surface potential can either be varied using a

MIS structure or by depositing charged ions on the insulator surface. In this section different examples of the two methods will be described.

5.1.1 *LIFETIME MEASUREMENTS IMPLEMENTING GATE ELECTRODES*

By applying a voltage over a metal-insulator-semiconductor (MIS) structure it is possible to directly change the surface potential in the same way as for a C-V measurement (section 4.3.1). The SRV can then be calculated from measurements of the effective lifetime in the region affected by the external voltage. The use of metal electrodes for this purpose has the important advantage that the surface potential can be readily changed by the press of a button, and measurement can be performed in a fast and efficient manner. It is also easy to do multiple voltage sweeps to investigate the repeatability of the results and obtain information on whether the sample is influenced by the measurement.

Conventional lifetime measurements based on measurements of the excess photoconductance are however problematic to use for this purpose, as the metal layer typically shields either the excitation light or the induced magnetic field from entering the sample. This problem has previously been overcome by using partially transparent electrodes made of very thin metal layers [90], [91] or a mercury probe in combination with transparent conductive oxide layers as electrodes [92]. In these works lifetime measurements were performed in transient mode (Eq. (4.5), as quantification of absolute values for both the generation rate and the excess conductance is difficult when taking the influence of the metal layers into account.

5.1.2 *LIFETIME MEASUREMENTS AFTER CORONA CHARGING*

In order to avoid the problems caused by highly conductive and opaque metal electrodes described in the section above, the surface band bending can also be influenced by deposition of charged ions on the surface of the dielectric. The technique was first presented by Schöfthaler et al. [93] who reported very low SRV values below 1 cm/s on 0.25 Ωcm float-zone (FZ) p-type Si wafers passivated with thermal SiO_2 and covered in a layer of positive ions. The deposition of charged ions is normally performed in a corona charging setup, as shown in Figure 5.1. A wafer with dielectric layers on both sides is placed on a grounded metal electrode, and a metal needle, normally made of tungsten, is placed a few cm above the sample. A voltage of 5-10 kV is then applied between the needle and the bottom electrode. The field strength close to the tip of the needle is large enough to ionize molecules in the ambient air, and depending on the polarity of the voltage, positive or negative ions can be deposited on the sample surface. The charged ions are stabilized by attracting charge carriers

in the Si substrate, which cause the desired surface band bending. The charged ions have a short free path length in air, so they arrive at the sample with little kinetic energy, and will thus not cause any surface damage. If the passivation layer is well insulating and the ambient humidity is low the surface charges are stable. The charges may readily be washed off in a polar solvent like water or isopropanol.

Corona charging has the advantage of being non-destructive and contactless, so that there are not any complications with subsequent lifetime measurements, and has therefore become very popular for characterization of solar cell passivation materials, [22],[57], [94],[95],[96],[97]. The method is however dependent on a secondary measurement using a vibrating kelvin probe for quantification of the charge density on the surface. Also, the process of charging the surface and measuring the charge density and the carrier lifetime is time-consuming. If the investigated passivation layer is not perfectly insulating (e.g. due to the presence of pinholes or defects), the charge density is not stable over time, which may cause quantification issues and poor repeatability. There have also been reports on irreversible damage to the SiO_2 layers after corona charging, possible caused by the large field strengths over prolonged time below the charged surface [98].

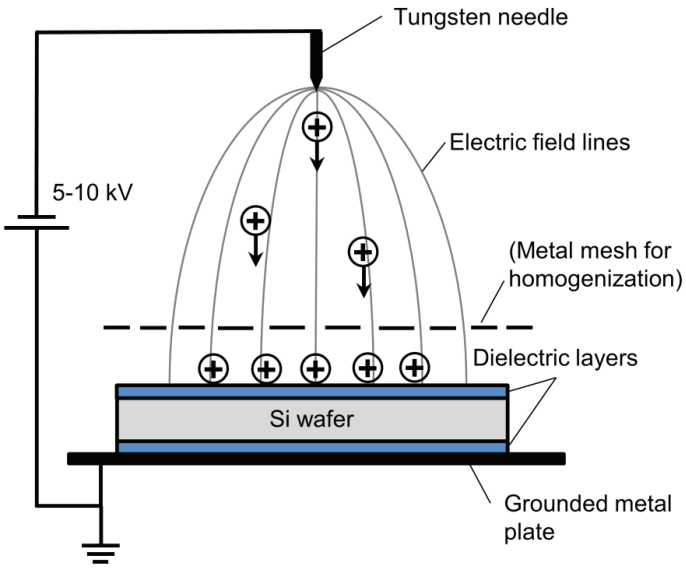

Figure 5.1. Schematic illustration of a corona charging setup used to deposit charged ions on the surface of a dielectric layer. Figure adapted from [94].

5.2 THE PL-V METHOD

In Paper I we for the first time introduced the idea of using photoluminescence imaging (PL-I) measurements (section 4.2.3) in combination with metal electrodes to measure the surface passivation properties of dielectric materials by varying the surface potential. Analysis of such curves, for instance using the Girisch model described in section 2.3.3.1, gives valuable information about the passivation mechanisms, and can be used to separate the contributions from field-effect and chemical passivation. Such a procedure may be used to determine the three defining parameters S_{n0}, S_{p0} and Q_f for a wide range of dielectric passivation layers, and in combination with supplementary measurements of the interface state density D_{it} the method can also be used to determine the absolute values of σ_n and σ_p for the recombination active defects at the interface.

5.2.1 DESCRIPTION OF THE MEASUREMENT

An advantage of the PL-I technique as compared to e.g. QSSPC is that both the excitation source and detection of the emitted PL light are on the same side of the sample, thus enabling measurements on wafers with rear side metallization. Also, unlike most μPCD measurement setups there is plenty of room around the sample for probes, wires and other equipment necessary for contacting the sample. An inductively coupled coil cannot (directly) be used for calibration of wafers with rear metallization, but the self-consistent calibration procedures described in section 4.2.3 can still be used. Alternatively, the calibration can be performed before processing of the metal layer, or on a part of the wafer without metallization, after correcting for optical effects, as shall be described in section 5.2.4. The latter approach was used for the measurements in this work.

A schematic illustration of the PL-V measurement setup is shown in Figure 5.2. Steady state lifetime measurements were carried out with a LIS-R1 PL imaging setup from BT imaging described in section 4.2.3. An external voltage source is connected to the sample in order to obtain lifetime images with an applied bias over the rear passivation layer. The voltage was changed in steps and the injection level Δn was calculated at each point from the PL intensity averaged over the central region of the electrode from Eq. (4.8).

A picture of typical samples used for combined PL-V, C-V and QSSPC measurements is shown in Figure 5.3 (a) and the electrical connections to the sample on the PL sample stage are shown in Figure 5.3 (b). The reference region used to calibrate the measured PL signal can either be made as a part of the same sample, or a separate reference sample may be used.

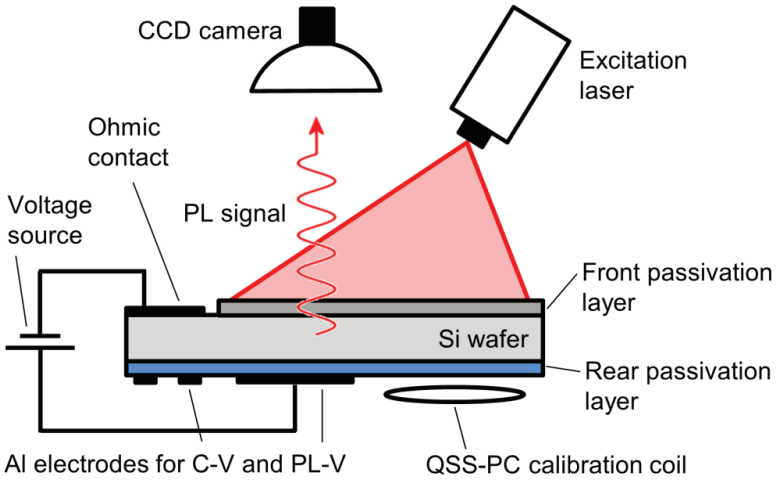

Figure 5.2. Schematic illustration of the PL-V measurement setup.

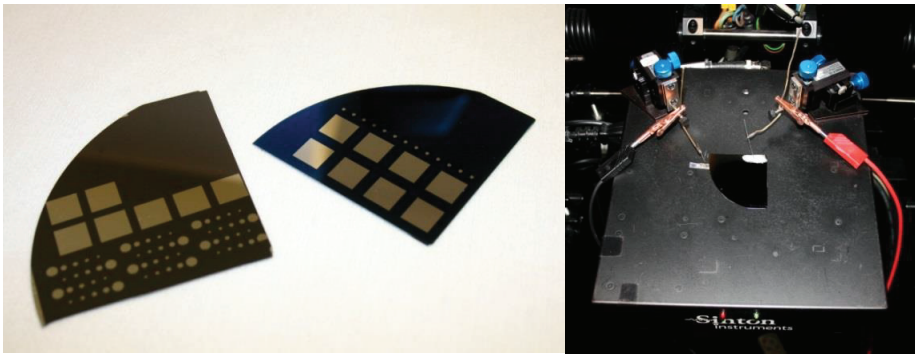

Figure 5.3. (a) Typical samples used for combined PL-V, C-V and QSSPC measurements. The samples shown are passivated with thermal SiO_2 (left) and PECVD a-SiN_x:H (right). The 7×7 mm^2 square electrodes are used for PL-V measurements, and the circular electrodes for C-V measurements. (b) Picture of the sample stage with probes for contacting of the samples.

A flowchart illustrating the measurement procedure and the necessary sample properties is shown in Figure 5.4. The parameters have already been presented in section 4.2.3. As described in the first column, several sample-specific properties need to be known in order to correctly calculate the effective lifetime. The measurement of the excess photoconductivity and the PL intensity in the reference region are used to calculate the calibration constant C_{cal}. as described in section 4.2.3. These measurements are made once for each PL-V curve, so that only the uncalibrated PL images are recorded for each value of the applied voltage. To simplify the procedure the QSSPC calibration curve and the raw PL images were imported into Matlab and analyzed using a custom-built script.

A typical PL-V measurement is shown in Figure 5.5. The effective lifetime vs. voltage curve, which was published in Paper I, is measured on a sample passivated by PECVD a-SiN$_x$:H on the rear side, with a front side passivation layer of PECVD a-Si:H. Figure 5.5 (a)-(f) shows the effective lifetime images for selected voltages, illustrating how the lifetime in the region above the bottom right electrode changes as a function of voltage. Circular electrodes for C-V measurements with diameter of 1 mm can be seen to the right of the larger electrodes used for the PL-V measurements, and the coil used for the calibration QSSPC measurement is visible on the right side of the sample.

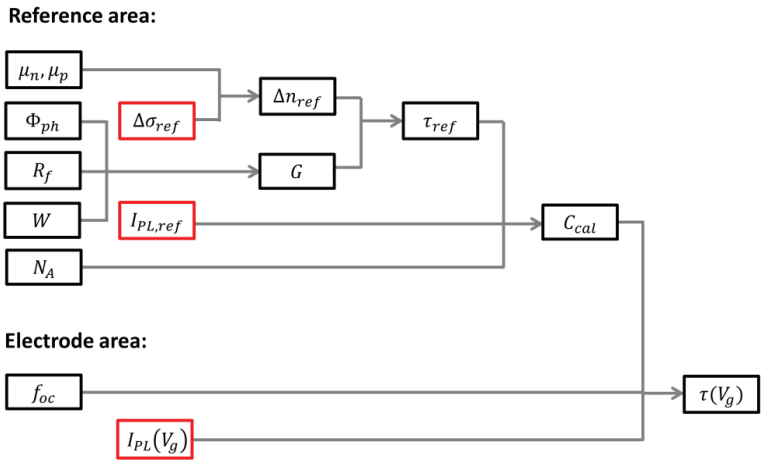

Figure 5.4. Flowchart showing the measurement procedure of a PL-V measurement. The first column shows input values that must be known for correct quantification and the quantities in the second column are the measured data. See List of Symbols on page 106 or section 4.2.3 for parameter definitions.

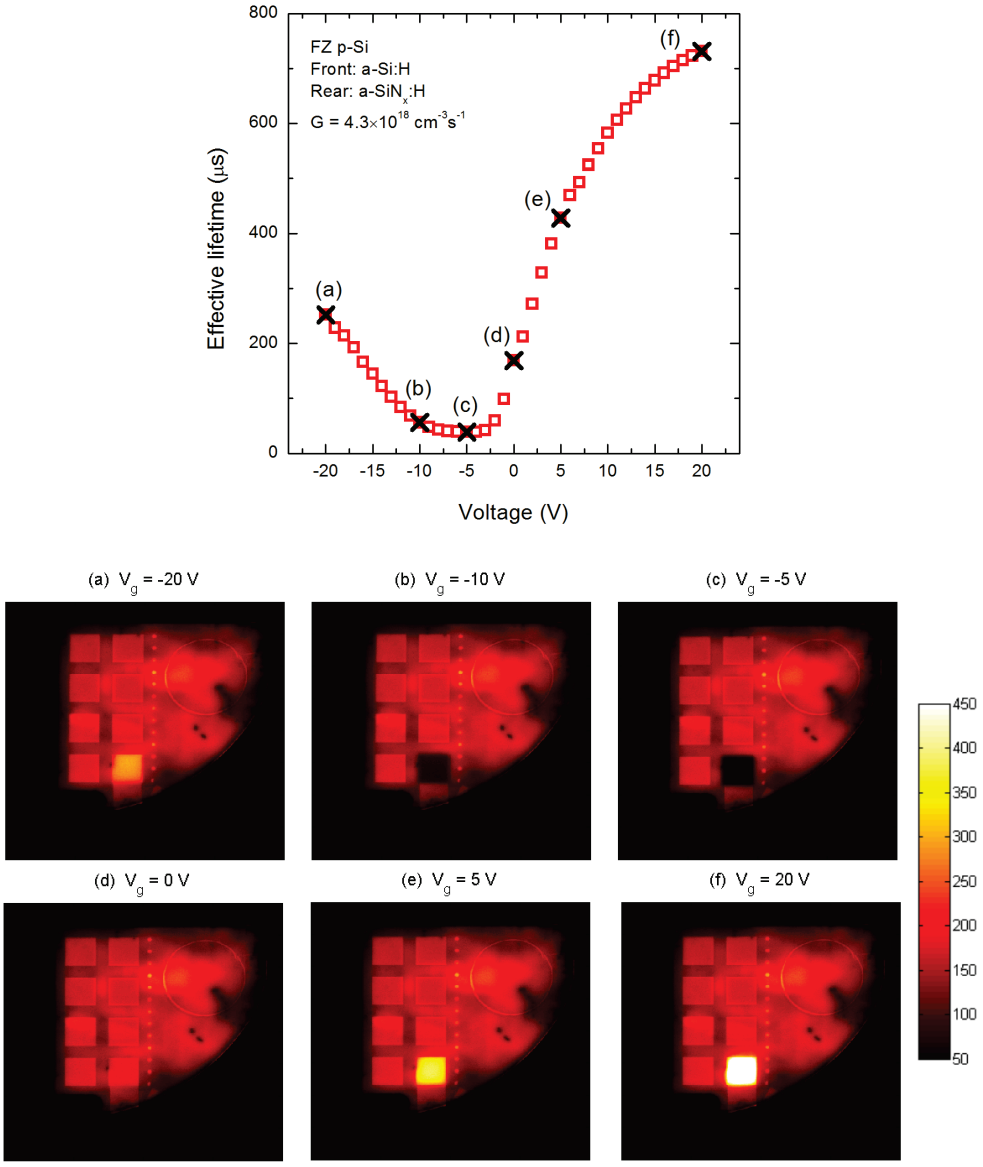

Figure 5.5. Top: Effective lifetime as a function of voltage applied over the rear side a-SiN$_X$:H layer. The lifetime values are averaged over the central part of the electrode area after correcting for optical differences between the metallized and reference regions. Bottom: Lifetime images corresponding to the six marked measurement points (a) to (f) above, showing the influence of the voltage applied to the bottom right electrode.

5.2.2 *ADVANTAGES AND LIMITATIONS*

Compared to the traditional method of corona charging the PL-V method has some advantages:

- The modulation of the surface potential can easily be changed and quantified in-between measurements using a voltage source, no external measurement of the surface potential is required.
- Measurements can be performed in-situ, as there is no need to move the sample. This may result in less error from handling and lateral variations of the surface properties.
- The PL measurement is fast. By using a computer to control the voltage source and the PL measurement the PL-V curve can typically be measured in less than 1 min. As the optical properties of the sample do not change during the measurement the more time-consuming calibration procedure needs to be performed only once for each PL-V curve.
- The fast measurement time allows for measurements of effective lifetime vs. voltage curves with high resolution. This is particularly important for data points close to the point of maximum recombination, where the SRV varies sharply with the applied voltage.
- The applied voltage can easily be turned off in-between measuring the data points of the PL-V curve in order to control if the sample is influenced by the applied voltage. For PECVD a-SiN_x:H layers and other films which exhibit significant charge buildup and hysteresis effects, this procedure can be used to quantify the error arising from changes in the charge density of the layers. Also, measurements can be performed with alternating positive and negative voltages with increasing magnitude in order to reduce the effect of charge buildup over time. This technique was used for the measurements presented in Paper I.
- Leakage currents through the insulating film do not affect the time stability of the surface potential, which may be a problem for corona charging techniques.
- If the modulation of the surface potential is applied to only a small part of the sample, errors may arise from edge effects and lateral carrier transport, which affect the extraction of the SRV from the measured lifetime in the area under investigation. As shown in Paper II, the imaging capabilities of the PL-I setup can be used for analysis and quantification of these effects.
- By utilizing the imaging capabilities of the PL-I setup together with a grid of metal electrodes, multiple areas of the sample can be measured simultaneously. This can be

useful for investigations of samples exhibiting lateral variations in the surface passivation properties.

However, the method also has some limitations as compared to corona charging.

- The PL-V method is a destructive technique, as metal electrodes have to be fabricated on top of the passivation layer, and a contact has to be made to the substrate. The metallization process is time consuming, and the wafers may not be used for subsequent processing. The process sequence for making PL-V samples is however very similar to the one used for making samples for C-V measurements, which are commonly used for characterization of insulating passivation layers. For most of the experiments presented in this work, a single sample was made for both QSSPC, PL-V and C-V measurements.
- In contrast to corona charging the PL-V setup only allows for modulation of the surface potential on the rear side of the wafer. The front SRV S_f must therefore be known, and the full asymmetric equations (Eq. (2.35) and (2.36)) for the surface lifetime must be used to calculate the rear side SRV S_r
- The metallized regions locally change the rear side reflectivity of the sample, causing the optical properties of the measurement area to differ from those of the reference region. This effect has to be taken into account in order to correctly quantify the effective carrier lifetime (see section 5.2.4 for details).

5.2.3 *SAMPLE REQUIREMENTS*

Based on the discussion above the following sample requirements need to be met to obtain a successful PL-V measurement;

- Samples should ideally be made from substrates with a high bulk lifetime to correctly calculate the SRV, particularly at large voltages where the SRV is usually low.
- Samples must be passivated on both sides. The front side passivation layer should ideally have as low SRV as possible, but symmetrically passivated samples can also be used.
- The reflectance (and absorbance) of the front side passivation layer at the excitation wavelength should be known.
- The rear side passivation layer should be insulating, with a low leakage current.
- The size of the electrode should be large enough to avoid significant effects of lateral carrier diffusion. Too large electrodes however have a larger probability for leakage currents caused by pinholes. From the discussion in Paper II we concluded that 7 x 7 mm electrodes were usually suitable. Also, several electrodes are made on each sample so that electrodes with too large leakage current can be discarded.

- Samples should ideally have a polished rear surface, in order to simplify the analysis and reduce the probability of pinhole formation.
- The rear side passivation layer should ideally have a low hysteresis in C-V measurements to avoid changing the insulator charge density during the measurements.

5.2.4 *CALIBRATION OF THE PL SIGNAL FROM METALLIZED REGIONS*

In order to obtain good results from a PL-V measurement, a precise relation must be found between the measured PL signal and the SRV over the electrode area. In Paper II we discuss different issues that are encountered in this process and attempt to quantify their impact on the final result. The most important problem comes from the fact that the rear side reflectance is higher in the metallized area than in the calibration area. This causes an enhanced PL signal at the metallized sample surfaces, due to the detection of long wavelength light reflected at the metallized rear surface. By directly applying the reference calibration to the metallized areas Δn will therefore be overestimated. For the PL-V measurements presented in this thesis the difference in optical properties, was taken into account by dividing the PL intensity in the region above the electrodes with an optical enhancement factor f_{oc}. The numerical value of this factor was determined experimentally for each sample by measuring the increase of the PL intensity after placing the sample over an Al mirror. In Paper II we also performed analytical calculations of the signal enhancement including wavelength-dependent emission, reflection and reabsorption. From these calculations we show that f_{oc} is not dependent on the carrier density in the sample, and we found a similar (within ~10%) numerical value as the one measured experimentally. Depending on the thickness and front and rear side reflectivity of the sample f_{oc} values between ~1.15 and ~1.40 have been used for the measurements performed in this work.

This issue of photoconductance calibration of metallized regions for PL imaging has as also been encountered previously [99]. Müller et al. [100] used a 970 nm short pass filter placed in front of the Si CCD camera to ensure that only the short wavelength part of the PL emission peak was used for the measurement. As these photons are easily reabsorbed within the sample they have a low probability for escaping and reaching the detector after having been reflected at the rear surface. In this way, less than 10% of the PL intensity reflected at the rear surface is detected for samples thicker than 140 μm.

During the work on Paper II we performed similar experiments using a 1000 nm short pass filter in front of the camera. As shown in Figure 5.6 the measured optical enhancement factor f_{oc} was reduced from 1.36 to 1.07 using the filter. This decrease however comes at the expense of an increased measurement time (for equal signal to noise ratio) by approximately a factor 10, since a large part of the emitted PL light is filtered out. The f_{oc}

value can in principle be further reduced by using a filter with a lower cut-off wavelength, at the expense of an even lower intensity of the PL signal.

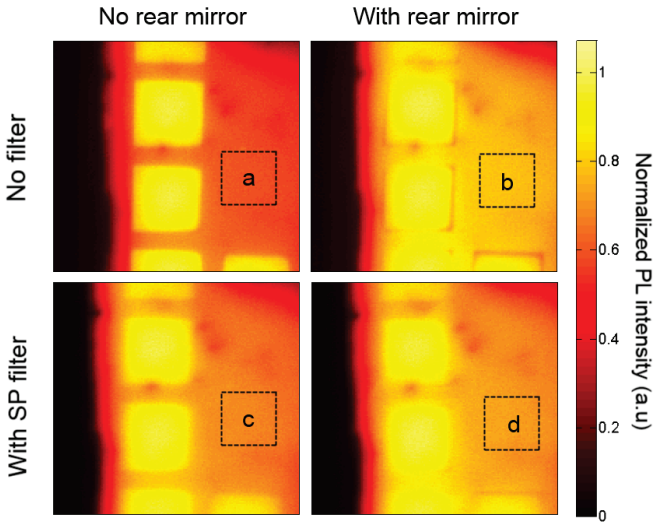

Figure 5.6. Uncalibrated PL images showing the effect of implementing a 1000 nm short pass filter in front of the camera. An Al mirror was placed behind the sample for the images to the right. The increase in intensity in the non-metallized reference region (a and b) is 1.36 without the filter. This ratio is reduced to 1.07 when using a short pass filter, as shown in the bottom two images (c and d). Note that the intensity is larger in the electrode area than in the reference region with a rear mirror. This is because of the improved passivation from a built-in electric field caused by the Al-Si work function difference.

5.2.5 OVERVIEW OF RESULTS

In this section we present selected PL-V measurements performed on p-type Si wafers passivated by different materials. Experimental PL-V curves measured on PECVD a-SiN_x:H are presented and analyzed in Paper I, and measurements of the thermally grown SiO_2 layers are discussed in Papers II and III. Both of these materials have been extensively studied for solar cell applications in the past. Our main motivation for these publications was however not to publish new material properties, but to develop the PL-V method and illustrate its potential as a characterization technique for solar cell passivation layers. The thermally grown SiO_2 layers also have the advantage of excellent dielectric properties (low leakage current, little hysteresis in C-V measurements, etc.) and stable passivation properties. For the same reason PECVD SiN_x layers with low refractive index ($n \sim 1.9$) where chosen for the measurements in Paper I, in order to the avoid difficulties with charge buildup and hysteresis effects commonly observed in high refractive index SiN_x layers [20].

In addition to this we have studied a few other material systems, including stacks of a-SiO_xN_y:H/a-SiN_x:H and a-Si:H/a-SiN_x:H processed by PECVD (as described in section 4.5) and single layers of Al_2O_3. The Al_2O_3 layers used for these measurements were processed by Yacine Boulfrad at the University of Aalto, Finland, using a Beneq TFS-500 thermal ALD system. The films were deposited at 200 ℃ to a thickness of 21 nm, using trimethylaluminum (TMA) and ozone (O_3) as process gases.

Figure 5.7 shows the measured SRV as a function of applied voltage for the passivation layers listed above. The processing details for the layers are given in section 4.5. and in Papers I, II and III. Eq. (2.23) states that the induced charge in the gate electrode scales inversely with the insulating layer thickness d_i, as long as the assumption that the fixed charges are located at the Si/insulator interface holds ($d_f = 0$). In order to properly compare the different measurements in the same figure, the voltage axis has therefore been scaled in each case to correspond to an insulator thickness of $d_i = 100$ nm. The red lines show simulation results from the Girisch model (described in section 2.3.3.1) with an added contribution to the SRV from subsurface recombination using the parameterization shown in Eq. (3.2). (This is the same model as the one that was used in Paper III). Following a similar procedure to the one used in the papers, a Nelder-Mead optimization algorithm which is available through the Mathworks Optimization toolbox [101] was used to fit the theoretical model to the experimental data for each measurement. The effective SRV parameters S_{n0} and S_{p0}, the fixed charge density Q_f and the parameters for the subsurface recombination mechanism $S_{min,n}$ and $S_{min,p}$ were used as free fitting variables. The best-fit simulation results are shown in Table 5.1. We find a good correspondence between the best-fit simulated curves and the experimental data, except for the fact that the extended SRH model consistently overestimates the maximum SRV in the region close to the flat-band voltage. A short discussion on this discrepancy can be found in Papers I, II and III.

Figure 5.8 shows the effect of the different parameters on the simulated curve. Note that even if five different free parameters are used, the best fit combination represents a unique solution, as the parameters influence the simulated curve in different ways. The peak position is mainly determined by Q_f, whereas S_{n0} and S_{p0} determine the slope of the left-hand and right-hand part of the curve, respectively. From Eq. (2.13) it can be seen that S_{eff} at is limited by the charge carrier type with the lowest surface concentration. For voltages below the minimum the surface potential ψ_s is negative, so that $n_s \gg p_s$. The last term in the denominator in Eq. (2.13) can thus be omitted, and S_{eff} becomes independent of S_{n0}, meaning that the slope of this region only depends on S_{p0}. Similarly, for $\psi_s > 0$ the slope of S_{eff} only depends on S_{n0}. The flattening of the curves at large negative and large positive voltages is described by the parameters $S_{min,n}$ and $S_{min,p}$, respectively.

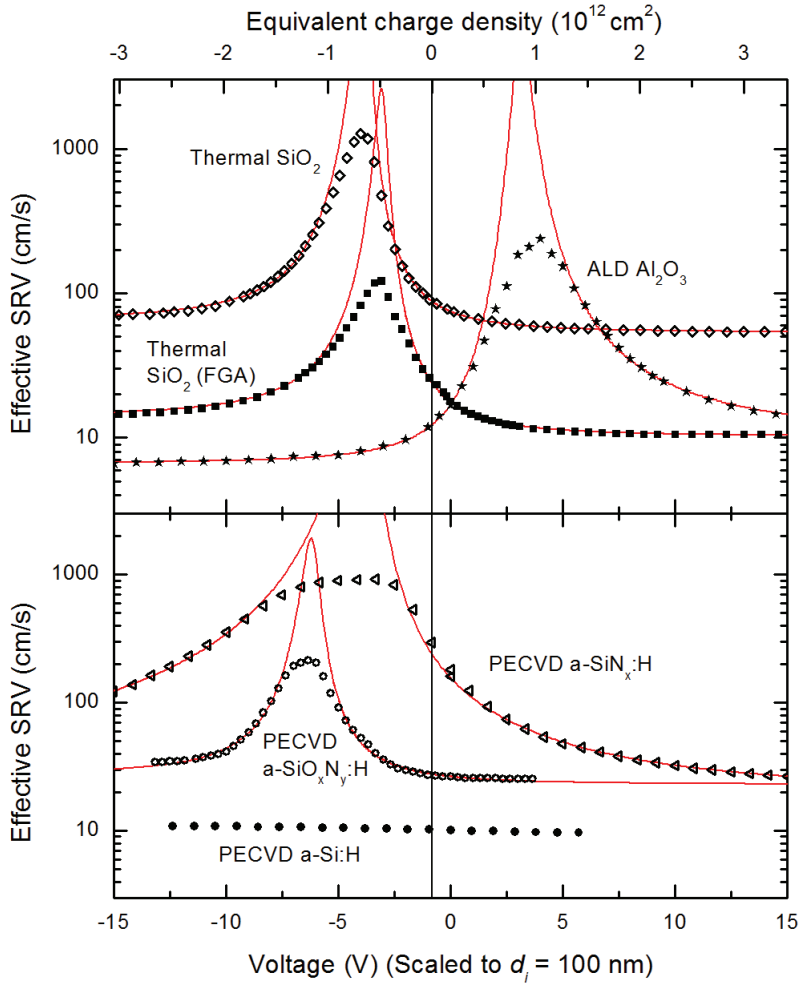

Figure 5.7. Effective SRV as a function of applied gate voltage for different passivation materials investigated during the course of this thesis. The Al-Si work function difference $\Delta\varphi_{ms}$ is subtracted and the voltage axis has been scaled to correspond to an insulator thickness of $d_i = 100$ nm for each curve. The top axis indicates the equivalent charge density, calculated from Eq. (2.23). The graphs are separated into two figures for the purpose of clarity. The metal-semiconductor work function difference $\Delta\varphi_{ms}$ (corresponding to zero external potential) is indicated by a vertical black line.

Table 5.1. Top: Parameters used as input to the simulations described in section 3.1 . The model was used to find the best fit to the measured SRV vs. voltage curves for different passivation materials shown in Figure 5.7. Bottom: Corresponding capture cross section ratio σ_n/σ_p and (average) fixed charge density extracted from high frequency C-V measurements.

Parameter	Unit	Thermal SiO_2		PECVD		ALD
		As-oxidized	After FGA	a-SiN_x:H	a-SiO_xN_y:H	Al_2O_3
Q_f	cm^{-2}	6.1×10^{11}	4.0×10^{11}	6.5×10^{11}	1.1×10^{12}	-1.4×10^{12}
S_{n0}	cm/s	2.1×10^{4}	2.5×10^{3}	2.5×10^{5}	3.2×10^{3}	8.5×10^{2}
S_{p0}	cm/s	8.8×10^{3}	9.9×10^{2}	4.1×10^{4}	2.1×10^{3}	1.1×10^{4}
$S_{min,n}$	cm/s	61	14	<20	29	6.6
$S_{min,p}$	cm/s	53	10	19.2	23	10.1
σ_n/σ_p		2.4	2.5	6.1	1.5	0.077
Q_f (C-V)	cm^{-2}	6.9×10^{11}	3.5×10^{11}	$7-8 \times 10^{11}$	$1-2 \times 10^{12}$	-1×10^{12}

All the samples were symmetrically passivated, and the front side SRV S_f was calculated from the effective lifetime in the reference region, as described in Papers II and III. The only exception is the PECVD a-SiN_x:H sample, which was passivated by a high quality PECVD a-Si:H layer on the front to minimize the influence of front side recombination. In the analysis performed in Paper I, S_f was set as a free fitting parameter, used to describe the flattening of the lifetime vs. voltage curve at large voltages. The best-fit S_f value was however several times larger than the experimental SRV normally measured for the a-Si:H layers. For the analysis shown here we have therefore used a fixed S_f of 7 cm/s, calculated from lifetime measurements of double side a-Si:H passivated reference samples. The flattening of the lifetime vs. voltage curve at large voltages is instead described as an added contribution to the rear side SRV, i.e. following the approach used in Paper II and III.

By examining the SRV vs. gate voltage curves in Figure 5.7, several observations can be made regarding the properties of the different passivation layers. Firstly, the materials containing positive charges (PECVD a-SiN_x:H and a-SiO_xN_y:H and thermal SiO_2) all show a peak in the SRV for negative voltages, whereas the peak is observed at a positive voltage for the negatively charged ALD Al_2O_3 layer, as expected. The equivalent charge density corresponding to the applied voltage values are shown on the top x-axis of the figure. Note that the position of the peak in each case corresponds to the Q_f value extracted from the simulations shown in Table 5.1.

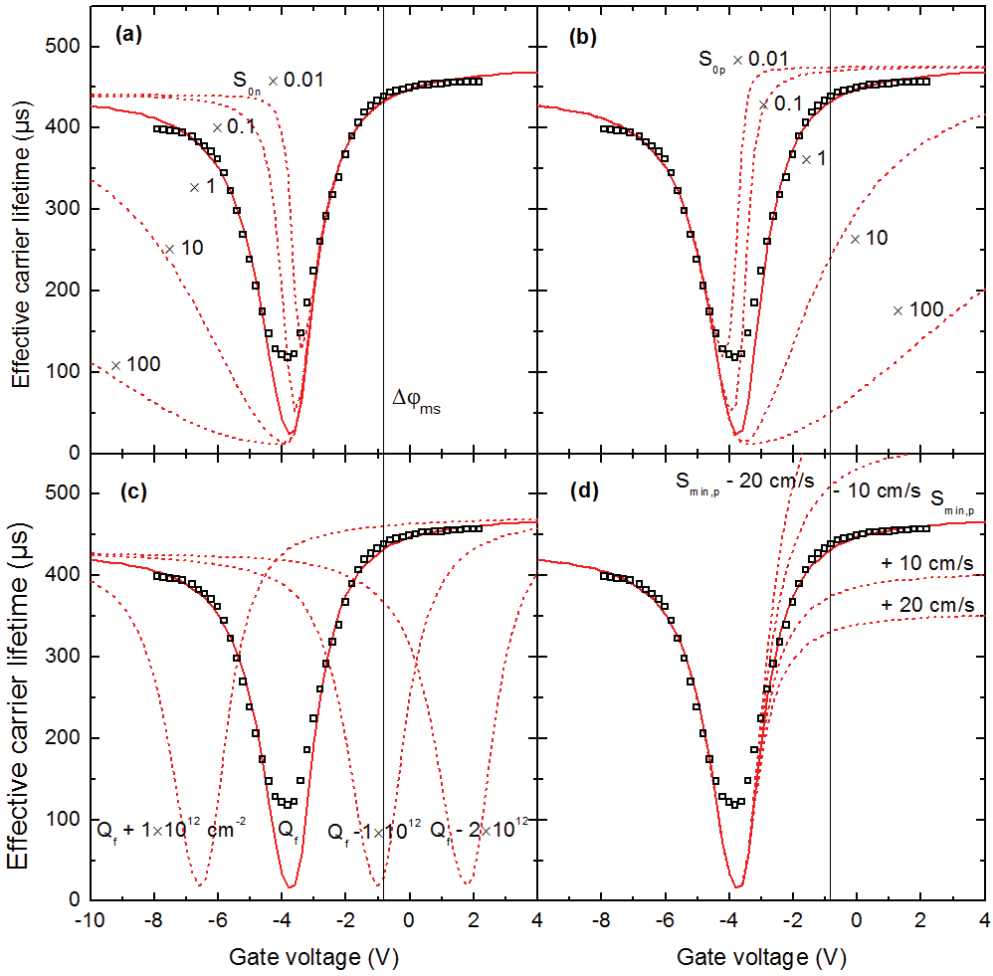

Figure 5.8. A typical PL-V measurement measured on a PECVD a-SiO_xN_y:H film, showing the effective carrier lifetime vs voltage. Different simulated curves are shown to illustrate the impact of the simulation parameters: (a) SRV parameter for electrons S_{0n}, (b) SRV parameter for holes S_{0p}, (c) Fixed charge density Q_f and (d) Added SRV contribution in inversion $S_{min,p}$. The best-fit parameters are given in Table 5.1. The metal-semiconductor work function difference $\Delta\varphi_{ms}$ (corresponding to zero external potential) is indicated by a vertical black line.

The slope on each side of the peak is steepest for the material with the highest degree of chemical passivation, whereas the slope is less steep for e.g. PECVD a-SiN_x:H, caused by a larger recombination activity of the surface defects (larger S_{n0} and S_{p0}). Because the slope at the left and right side of the SRV maximum is described by S_{n0} and S_{p0} parameters, the asymmetry of the SRV peak gives a good measure of the ratio between S_{n0} and S_{p0}, which is equal to the ratio of the capture cross sections σ_n/σ_p of the surface defects. This ratio is shown in Table 5.1 for each passivation layer. The thermal SiO_2 and PECVD a-SiO_xN_y:H layers have an electron/hole capture ratio close to 1 (1.5-2.5) and the PECVD a-SiN_x:H layer has a somewhat larger σ_n/σ_p ratio of 6.1. On the other hand, the ALD Al_2O_3 layer has a clearly asymmetric SRV vs. voltage peak, with σ_p over 100 times larger than σ_n ($\sigma_n/\sigma_p < 0.01$). A similar asymmetry in the Al_2O_3 passivation peak has also previously been observed by other groups [30].

PL-V measurements were also attempted on a PECVD a-Si:H/a-SiN_x:H stack. The measured lifetime did however not change significantly with gate voltage. This may be caused by the fact that the a-Si:H layer is not sufficiently insulating, so that the voltage drop occurs over the capping layer only, and no surface band bending is obtained. Alternatively, the high degree of chemical passivation for the a-Si:H layer cannot be further improved by an additional field effect. The measurement is included in Figure 5.7 for reference.

CHAPTER 6

PRELIMINARY RESULTS AND FURTHER WORK

There are always unfinished projects at the end of a PhD. Luckily, all parts of this work will be continued by the candidate, with several related publications planned in the months and years to come. In this section a few preliminary results and ideas for continuation of this thesis work are presented.

6.1 DEVICE IMPLEMENTATION

In order to test the PECVD layers presented in section 4.5 as rear side passivation in a device structure we have developed a lab-scale solar cell process. The cell structure is rear passivated with local contact openings created using a femtosecond laser on both the front and rear side. The process is far from industrially relevant, as it does not include front surface texturing (resulting in a high front side reflectance) and involves multiple local laser processing steps (resulting in an expensive and time consuming processing). Instead the resulting cell is intended to be used as a reproducible and easily analyzed test-bed for investigation of fundamental physical mechanisms. The cell process also has the advantage of being capable of successfully producing solar cells from very thin wafers ($W = 50$ μm has been successfully demonstrated), and the resulting solar cell structure can therefore also be used for future testing of different light trapping schemes. Another important application of the co-planar cell process will be to develop a gate controlled solar cell, as shall be discussed in section 6.1.4.

6.1.1 *PROCESS SEQUENCE*

For the first experiments, solar cells and lifetime test samples were fabricated from 3 Ωcm double-side polished FZ p-type Si wafers with a thickness of ~280 μm, using the process steps shown in Figure 6.1. The high quality FZ wafers ensures that the cell is not affected by bulk recombination, and the clean polished surfaces are ideally suited for fundamental investigations of surface recombination mechanisms and comparisons with lifetime test samples. The process has a low thermal budget (T < 450 ℃) and no contact firing steps, implying that materials like PECVD a-Si:H can be utilized, which would otherwise be significantly degraded by high temperature processes.

Line contacts were created by using a femtosecond processing laser for locally opening the PECVD layers and a RF sputtering system for deposition metallic Al layers through a shadow mask. Non-overlapping laser pulses were used for this purpose, with a 35% opening fraction within each line contact.

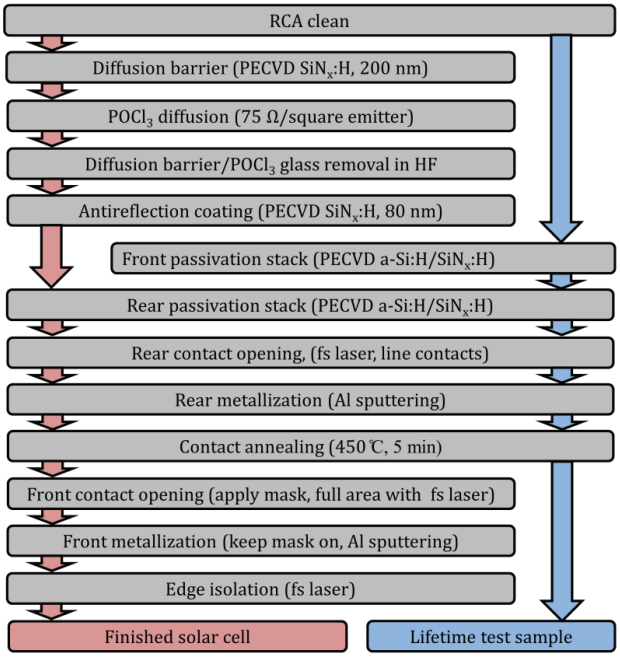

Figure 6.1. Process sequence for the co-planar solar cell structure used for investigations of surface passivation layers and for the lifetime test structures used for investigation of recombination at the partially metallized, passivated Si surfaces.

6.1.2 *SRV MEASUREMENTS OF PARTIALLY METALLIZED REGIONS*

Prior to the solar cell processing the rear side structure was investigated on double-side passivated test samples without the emitter layer (right hand process in Figure 6.1). The total effective SRV of the passivated and locally contacted regions was calculated from PL-I measurement of the effective lifetime over the metallized regions, as shown in Figure 6.2. The PL signal was calibrated using a QSSPC measurement in a reference region without metal contacts, using an assumed signal enhancement of 20% from increased reflectance of the rear side metal. The pitch between the rear contact fingers, the width of each finger and the power used for laser ablation was varied by processing 1 × 1 cm² patches of each parameter set over the test samples. The measurements were also repeated after multiple subsequent annealing steps at 450 ℃ in order to find the optimal annealing time which gives a low contact resistance without degrading the a-Si:H/a-SiN_x:H passivation stack.

Figure 6.3 (a) shows the measured SRV as a function of the rear side metallization fraction, which was varied by changing the pitch between the rear contacts. As expected the SRV decreases as the fraction of metallized area is reduced.

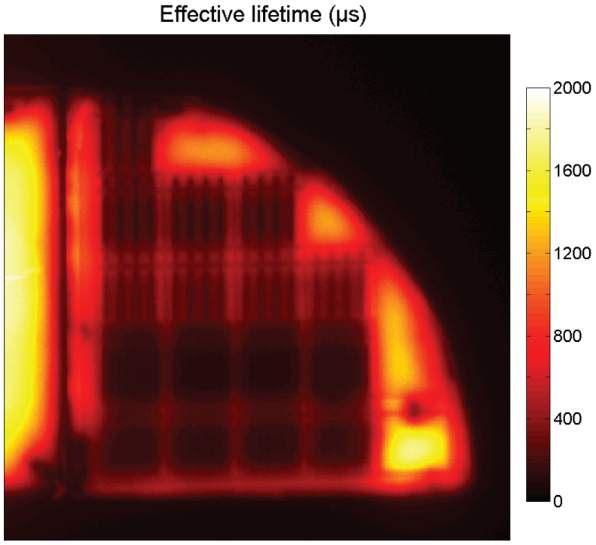

Figure 6.2. PL image of the effective lifetime of a test sample with areas of different rear side processing parameters. Four different metallization patterns (p = 0.1 cm, 0.3 cm, $f_{met} = 1\%, 3\%$) and four different laser parameters are shown.

6.1.3 SOLAR CELL CHARACTERISTICS

Measured cell efficiencies and open circuit voltages V_{oc} are shown in Figure 6.3 (b) for four different cells with varying rear side metallization fraction f_{met}. Both the V_{oc} and short circuit current J_{sc} (not shown) were observed to increase with decreasing f_{met}. As no significant change in the series resistance and the fill factor was observed for decreasing f_{met} for the locally contacted cells, the measured reduction in the rear SRV resulted in an increased in the cell efficiency from 13.8 % at $f_{met} = 100\%$ to 15.8% at $f_{met} = 1\%$. The I-V curve for the best cell is shown in Figure 6.4, together with a schematic illustration of the cell. Note that the absolute efficiency values are limited by large reflectance and shading losses on the front surface, resulting in relatively low values for J_{sc}. The relatively high V_{oc} values are however indicative of low recombination loss. The internal quantum efficiency data measured on the same cells is shown in Figure 6.5. The increased SRV for large f_{met} values reduces the collection probability (quantum efficiency) for charge carriers excited by low energy photons, which are generated deep in the bulk of the wafer. As expected, the measured red response of the solar cells therefore decreases with increasing rear SRV (increasing f_{met}), corresponding to the observed changes in solar cell efficiency.

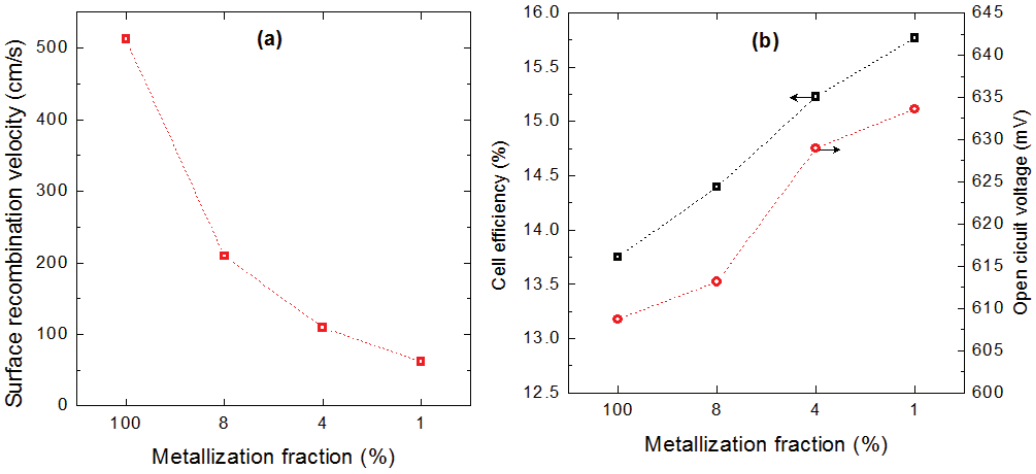

Figure 6.3. (a) Rear side effective SRV as a function of the rear metallization fraction f_{met}, for optimized laser power and annealing time. Measurements were performed on test samples with identical rear metallization as the solar cells, and the SRV values are for the combination of passivated and metallized regions. (b) Measured cell and open circuit voltage as a function of rear side metallization fraction.

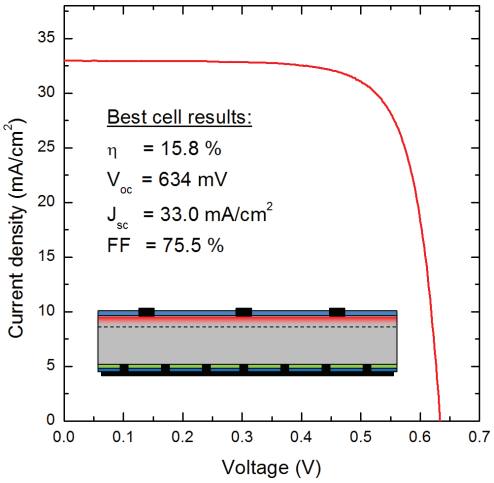

Figure 6.4. Current-voltage curve and key solar cell characteristics for the best cell, created from

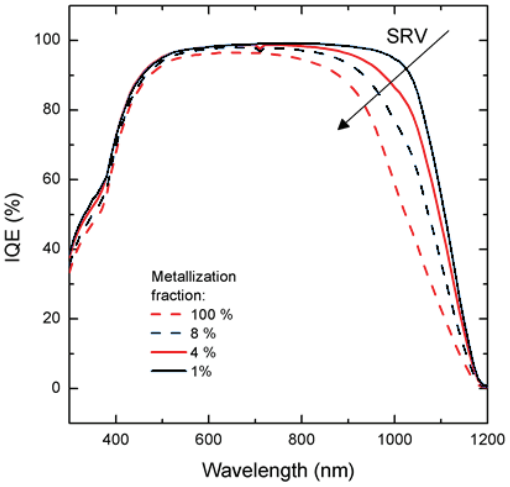

Figure 6.5. Measured internal quantum efficiency curves for the four solar cells described in Figure 6.3, showing the increased red response with decreasing rear side SRV.

6.1.4 *GATE-CONTROLLED SI SOLAR CELL*

An interesting possibility for future work using the co-planar cell structure described above is the production of a gate-controlled Si solar cell. By implementing a large, "interdigitated" electrode in-between the rear contact fingers, an external voltage can be used to directly control the field-effect passivation on the rear side of the solar cell under operation. This idea has also been suggested previously, for example by Aberle et al. [34], but is much more powerful in the combination of the PL-V method developed in this work. The combination of electrical characterization (I-V, IQE) as a function of gate voltage and full area PL-V measurements will hopefully provide enhanced knowledge of the recombination mechanisms in solar cells incorporating rear side field-effect passivation structures.

Initial experiments have been performed, and we hope to demonstrate a working gate-controlled solar cell in the near future. Figure 6.6 shows a PL lifetime images measured on the full cell area of 2.7×2.7 cm² for different values of the applied voltage. The samples are lifetime test samples for contact testing (right hand process in Figure 6.1), using a 150 nm thick a-SiN_x:H layer for the rear side passivation. A relatively thick a-SiN_x:H layer was adopted in order to reduce leakage currents. As seen from Figure 6.6, the SRV of the rear surface changes homogeneously across the sample as the gate voltage is varied. In the planned experiment, this behavior of the SRV will be linked to measured electrical characteristics of the cells at different gate voltages and fitted to simulations using the cmd-PC1D program.

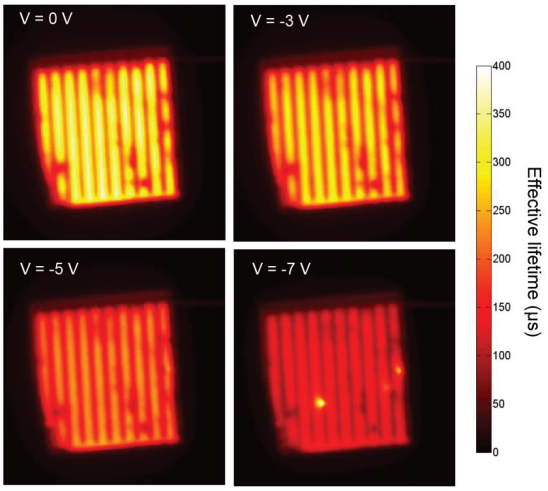

Figure 6.6. PL images measured on lifetime test structures with a large electrode deposited in-between the rear contacts fingers, for different values of the voltage applied over the rear side passivation layer.

Another interesting feature of the gate-controlled cell structure is the possibility of permanently changing the fixed charge density of the PECVD a-SiN_x:H layers. As discussed in section 2.5.2.1 the fixed charge density in such layers is attributed to so-called K-centers, which can be both positively and negatively charged by interaction with mobile carriers in the Si wafer. The charge state of these centers can be changed by a sufficiently large electric field, e.g. from an applied voltage. The process can be both fast and reversible, and is therefore utilized in flash memory devices [102]. By applying a large gate voltage over the rear side of a solar cell it is therefore possible to permanently change Q_f and produce negatively charged a-SiN_x:H layers, which are more suitable for passivation of p-type base material [103]. Figure 6.7 shows the result of such experiment on a sample originally intended for PL-V measurements. A significant, permanent decrease in the SRV, caused by an increased fixed charge density, could be obtained by applying a large negative voltage of -60 V for several seconds. This improved passivation was found to be very stable, persisting without the need for an external voltage for more than two years.

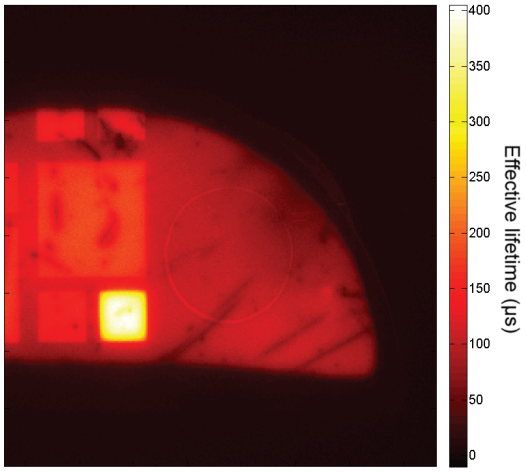

Figure 6.7. Effective lifetime image measured by PL–I showing locally improved passivation properties of the PECVD a-SiN_X:H layer after charging the dielectric using a large voltage. The image was taken more than two years after the voltage was applied, implying that a permanent change of the fixed charge density of a-SiN_X:H layers is possible with this method.

6.2 FURTHER WORK ON THE PL-V METHOD

6.2.1 AUTOMATED MEASUREMENTS AND PROCESS CONTROL

For the PL-V measurement presented in Chapter 5 and in the papers, the voltage was changed manually between each measurement. However, one of the most important advantages of the PL-V method is the possibility of automating the measurements, so that the whole lifetime vs. voltage curve can be recorded by the click of a button. A setup for automated measurements is planned in the near future, using a Windows automation software for controlling the PL measurements and a programmable voltage source connected to the instrument computer. Furthermore, it would be useful to build a custom sample stage with metal pads and clamps for easy contacting of the samples.

Another interesting aspect of the PL-V method is to use it for process control of passivation layers during solar cell production. By employing a fast electrode deposition, for instance by the application of liquid metal electrodes, the PL-V method may possibly also be used for fast, automated and spatially resolved characterization of Si surface passivation layers, allowing for in-line control of selected wafers during solar cell fabrication.

6.2.2 *VARIATION OF THE GENERATION RATE AND MEASUREMENTS AT CONSTANT INJECTION LEVEL*

PL imaging as described in section 4.2.3 is a steady state technique, meaning that the generation rate is constant for each image. By varying the intensity of the excitation source, effective lifetime vs. voltage curves can however be measured for different generation rates. So far a fixed generation rate with relatively low intensity has been used in order to avoid high injection conditions. However, because each measurement is relatively fast (in the order of seconds), several images with varying generation rate can be recorded for each value of the applied voltage while still keeping a low total time for the measurement. The measured carrier lifetimes as a function of both voltage and generation rate provide valuable additional information about the surface passivation layer under investigation, and gives more data points when comparing the results with simulations.

Figure 6.8 shows an example of PL-V curves measured on a thermally oxidized Si sample for three different generation rates *G*. This measurement has been used to investigate the injection level dependence of the flat regions on each side of the lifetime minimum. A model consisting of the Girisch (section 2.3.3.1) together with the expression from Glunz et al. [19] for space charge recombination (Eq. (2.30)) was fitted to the experimental data. As seen from the figure, the same parameters could be used to find a good fit for all three curves, by using a ideality factor of $m = 1.3$ for the space charge recombination current. This value is

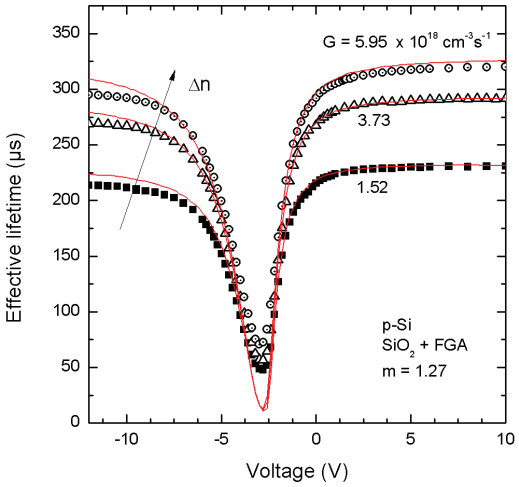

Figure 6.8. Effective lifetime as a function of applied gate voltage for three different generation rates. The measurements are performed on a p-type sample passivated on both sides by thermal SiO_2 layers.

lower than the range of 1.5-1.8 predicted by Dauwe [17], as described in section 2.3.4.

By interpolating between the lifetime values measured at different generation rates as described above it is also possible to construct lifetime images and lifetime vs. voltage curves for a constant injection level instead of constant generation rate. This can also be achieved by changing the excitation intensity for each voltage until a given PL intensity (corresponding to a fixed injection level) is measured over the electrode area. Measurements of PL-V curves with constant Δn may provide additional information and simplify comparison with simulations, which are commonly performed at a constant injection level.

With the LIS-R1 setup used in this work the (constant) photon flux Φ_{ph} can be varied between 9.2×10^{15} $\mathrm{cm^{-2}s^{-1}}$ and 3.4×10^{17} $\mathrm{cm^{-2}s^{-1}}$, corresponding to a generation rate G in the range from 2.9×10^{17} $\mathrm{cm^{-3}s^{-1}}$ to 1.1×10^{19} $\mathrm{cm^{-3}s^{-1}}$ for a typical lifetime sample ($R_f = 5\%, W = 300$ μm). The dynamic range of the measurement (the highest measured lifetime divided by the lowest) can therefore in principle be up to 38 while still keeping a constant Δn for the entire curve.

6.3 FERMI-DIRAC STATISTICS AND IMPROVED PHYSICAL MODELS FOR THE CMD-PC1D PROGRAM

One of the major drawbacks of the PC1D program is the use of Boltzmann statistics, which results in significant errors in regions with high doping or large carrier concentrations [104]. This approximation was used to simplify and speed up the calculations, but with modern computers this is no longer necessary in order to achieve acceptable computation times. With this in mind we are currently working on a new, modified version of PC1D which applies the correct Fermi-Dirac (F-D) statistics for the charge carrier dynamics, thus giving more accurate results.

Also, current models available for crystalline silicon rely on the most recent data and are generally more precise and sophisticated than the general parameterizations of semiconductor properties implemented in PC1D. We have implemented several new models for crystalline Si in the modified PC1D program, including up-to-date models for injection dependent band gap narrowing [105], carrier mobility [106] and Auger recombination [11]. These advanced models together with F-D statistics are necessary for obtaining correct results when simulating highly doped regions, such as solar cell emitters. The new Auger parameterization also gives improved accuracy of simulations on lowly doped n-type

material. The updated models are not pre-initialized, but are coupled to the carrier densities throughout the device, enabling injection dependent evaluation.

As shown in Figure 6.9, the results from the PC1D simulations have been verified against an existing Excel VBA implementation of the models, which has previously been cross-checked against commonly used simulation tools like the numerical simulation tool EDNA [107] and the Sentaurus TCAD package. The relative deviation between the two calculations was found to be less than 0.05% for all the simulated parameters.

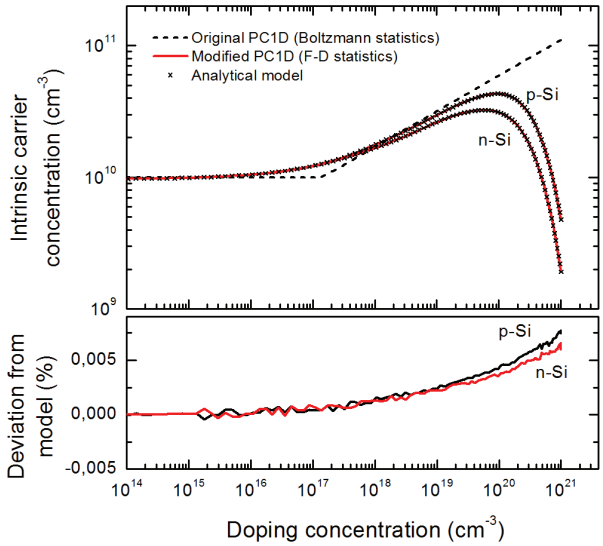

Figure 6.9. Top: Intrinsic carrier concentration as a function of doping concentration, calculated with the original PC1D (black dashed line) and the modified PC1D program (red solid line). The results from the Excel VBA implementation are shown as black symbols. Bottom: Corresponding relative deviation between the PC1D output and the Excel VBA implementation.

CHAPTER 7

CONCLUDING REMARKS

The paramount objective of this PhD thesis was to gain a fundamental understanding of the passivation mechanisms of different surface passivation layers. On the path towards this goal we have developed procedures for reproducible, high quality processing of passivation layers by both direct PECVD and thermal oxidation. By adopting a low temperature a-Si:H/a-SiN_x:H stack we were able to consistently produce surfaces with SRVs below 4 cm/s for both Si substrate polarities, with the lowest SRV measured at 1.2 cm/s on n-type 3 Ωcm FZ material. Within this work we have also developed a thermal oxidation process with high quality surface passivation, with stable SRVs of 15 cm/s (18 cm/s) on n-type (p-type) substrates after forming gas anneal. These values are sufficiently low for effectively reducing or eliminating the power loss arising from surface recombination in high efficiency solar cells.

One of the two main contributions from this work is the development of the PL-V method, a new characterization technique for quantitative measurements of the effective lifetime (and thus the SRV) of dielectric surface passivation layers as a function of the surface band bending. The technique is based on measurements of the effective lifetime in an existing PL imaging setup while applying a voltage to an electrode placed on the rear side passivation layer. We show that these measurements have several important advantages over the commonly used corona charging methods while producing very similar results on thermally oxidized samples. Important measurement uncertainties have been discussed and accounted for, including optical effects from the electrodes, lateral carrier diffusion and hysteresis effects arising from changes in the insulator charge density during measurements.

Furthermore, the PL-V method has been used to investigate a range of different dielectric passivation layers. A routine for interpretation of the measured results have been

developed, using the extended SRH formalism and the Girisch model to solve the surface band bending problem. In addition, we found that the standard model was not sufficient to predict the experimental SRV for large absolute values of the surface potential. To account for the observed behavior we therefore included an additional contribution to the simulated SRV, which may arise from recombination at subsurface defect states or from tunneling of charge carriers through the space charge region. This model can be used to extract the important parameters S_{n0}, S_{p0} and Q_f for the standard SRH model, as well as the phenomenological parameters $S_{min,n}$ and $S_{min,p}$. Different passivation layers have been studied using this technique, including PECVD a-SiN_x:H and a-SiO_xN_y:H, thermal SiO_2 and ALD Al_2O_3. A good agreement was found between the best-fit Q_f under illumination and corresponding values extracted from dark C-V measurements. The capture cross section ratio σ_n/σ_p was found to be between 1 and 10 for all the investigated samples except for the ALD Al_2O_3 film, which required a σ_n/σ_p ratio below 0.01 to obtain the best fit.

The second main contribution from this work, and the one that so far has been mostly appreciated by other researchers, is the development of a command-line version of PC1D, which provides the possibility for scripted simulations. A new graphical user interface has been implemented, providing direct access to features like better data visualization, optimization and fitting to experimental data and implementation of external models.

LIST OF SYMBOLS

Symbol	Description	Unit
B_{rad}	Radiative recombination coefficient	cm^3s^{-1}
C	Capacitance per area	F/cm^2
C_{cal}	Calibration constant used for PL imaging	cm^3s
C_{fb}	Flat band capacitance	F/cm^2
C_i	Insulator capacitance	cm
C_{it}	Capacitance from interface states	F/cm^2
C_n, C_p	Auger coefficients	cm^6s^{-1}
C_{sc}	Space charge region capacitance	F/cm^2
$C_{sc,fb}$	Space charge capacitance and flat band conditions	F/cm^2
D	Minority carrier diffusion coefficient	cm^2/s
d_f	Thickness of insulator region containing fixed charges	cm
d_i	Thickness of insulating layer	cm
D_{it}	Interface state density per energy interval	$cm^{-2}eV^{-1}$
D_{it}	Interface state density	$cm^{-2}eV^{-1}$
$D_{it,d}$, $D_{it,a}$	Density of donor/acceptor type interface states	cm^{-2}
D_n, D_p, D_a	Electron/hole/ambipolar diffusion coefficient	cm^2/s
d_{sc}	Width of the space charge region	cm
d_{sc}	Space charge region width	cm
d_{SDR}	Thickness of the subsurface defect region	cm
E	Energy	eV
E_c	Conduction band energy	eV
E_F	Fermi energy	eV
E_g	Band gap	eV
E_i	Intrinsic energy level	eV
E_t	Trap energy level	eV
E_t	Single defect level energy	eV
E_v	Valence band energy	eV
f	Frequency	s^{-1}
f_d, f_a	Occupancy functions for donor- and acceptor type states	-
FF	Fill factor	%
F_m	Metal work function	eV
f_{oc}	Optical correction factor (for PL-V)	-
G	Optical generation rate per volume	$cm^{-3}s^{-1}$
G_p	Equivalent parallel conductance	S
I_{PL}	Detected PL intensity	counts/s
J_{02}	Equivalent diode saturation current	A/cm^2
J_{sc}	Short circuit current density	A/cm^2

k	Extinction coefficient	-
k_B	Boltzmann constant	eV/K
k_B	Boltzmann constant	J/K
L_D	Debye length	cm
m	Diode ideality factor	-
n	Electron concentration in the conduction band	cm^{-3}
n	Refractive index	-
n_0, p_0	Electron/hole concentration at thermal equilibrium	cm^{-3}
n_1, p_1	Statistical parameters for SRH recombination	cm^{-3}
N_A, N_D	Acceptor/donor doping concentration	cm^{-3}
n_b, p_b	Electron/hole concentration in the neutral bulk of the sample	cm^{-3}
n_b, p_b	Bulk concentration of electrons/holes	cm^{-3}
n_i	Intrinsic carrier density at thermal equilibrium	cm^{-3}
N_{it}	Interface state density per unit area, single defect level	cm^{-2}
n_s, p_s	Surface concentration of electrons and holes	cm^{-3}
N_t	Concentration of surface states, single defect level	cm^{-2}
N_t	Single defect level density	cm^{-3}
OC	Optical constant for QSSPC measurements	-
p	Hole concentration in the valence band	cm^{-3}
q	Elementary charge	C
Q_f	Fixed charge density in the insulating layer	cm^{-2}
Q_g	Charge density in the metal electrode	cm^{-2}
Q_{it}	Charge density in the interface states	cm^{-2}
Q_{sc}	Charge density in the space charge region	cm^{-2}
R_p, R_s	Reflectance for p- and s-polarized light	-
R_{sh}	Equivalent shunt resistance	Ωcm^2
S	Surface recombination velocity	cm/s
S_{eff}	Effecive surface recombination velocity	cm/s
S_f, S_r	Front/rear surface recombination velocity	cm/s
S_{it}	Interface surface recombination velocity	cm/s
S_{li}, S_{hi}	Surface recombination velocity at low/high injection conditions	cm/s
S_{max}	SRV calculated using infinite bulk lifetime	s
$S_{min,n}$, $S_{min,p}$	Added SRV contributions for $\psi_s < 0$ and $\psi_s > 0$	cm/s
S_{n0}, S_{p0}	Effective surface recombination parameters for electrons/holes	cm/s
S_{Rsh}	SRV contribution from tunneling current	cm/s
S_{SDR}	SRV contribution from subsurface recombination	cm/s
T	Temperature	K
t	Time	s
U	Rate of recombination	$cm^{-3}s^{-1}$
U_{Aug}	Rate of Auger recombination	$cm^{-3}s^{-1}$
U_{rad}	Rate of radiative recombination	$cm^{-3}s^{-1}$
U_s	Surface recombination rate per unit area	cm^{-2}
U_{SRH}	Rate of SRH recombination	$cm^{-3}s^{-1}$

V	Voltage	V
V_b	Separation of quasi-Fermi levels in the bulk	V
V_{fb}	Flat band voltage	V
V_g	Gate voltage	V
V_{oc}	Open circuit voltage	V
v_{th}	Thermal velocity for electrons	cm/s
W	Wafer thickness	cm
x	Distance from the interface	cm
α_0	Smallest eigenvalue solutions to equation (2.36)	cm^{-1}
β	q/k_BT	V^{-1}
$\Delta n(x=d_{sc})$	Excess carrier concentration at the edge of the space charge region	cm^{-3}
Δn, Δp	Excess electron/hole density	cm^{-3}
Δn_s	Excess carrier concentration at the surface	cm^{-3}
$\Delta\sigma$	Excess photoconductivity	S/cm
$\Delta\varphi_{ms}$	Metal-semiconductor work function difference	V
ε_0	Free space permittivity	F/cm
ε_i	Insulator dielectric constant	-
ε_s	Semiconductor dielectric constant	-
η	Solar cell conversion efficiency	%
λ	Wavelength	nm
μ_n, μ_p	Electron/hole mobility	cm^2/Vs
ρ	Charge density	C/cm^3
σ_n, σ_p	Capture cross sections for electrons and holes	cm^2
τ	Recombination lifetime	s
τ_{Aug}	Auger lifetime	s
$\tau_{Aug,li}$, $\tau_{Aug,hi}$	Auger lifetime at low/high injection conditions	s
τ_b	Bulk lifetime	s
τ_{eff}	Effective minority carrier lifetime	s
τ_{eff}	Effective carrier lifetime	s
τ_{n0}, τ_{p0}	Capture time constants for electrons and holes	s
τ_{n0}, τ_{p0}	Capture time constants for electrons/holes	s
$\tau_{n0,SDR}$, $\tau_{p0,SDR}$	Capture time constants for electrons and holes in the SDR	s
$\tau_{rad,li}$, $\tau_{rad,hi}$	Radiative recombination lifetime at low/high injection	s
τ_{SRH}	SRH lifetime	s
φ_n, φ_p	Quasi-Fermi levels for electrons and holes	V
Φ_{ph}	Excitation photon flux	$cm^{-2}s^{-1}$
Φ_{PL}	Rate of photoluminescence emission	s^{-1}
χ	Electron affinity	eV
ψ	Potential	V
Ψ, Δ	Ellipsometric parameters	-
ψ_s	Surface potential	V
ω	Angular frequency, $\omega=2\pi f$	s^{-1}

LIST OF ABBREVIATIONS

Abbreviation	Description
ALD	Atomic layer deposition
APCVD	Atmospheric pressure chemical vapor deposition
ARC	Antireflection coating
BSF	Back surface field
CCD	Charge-coupled device
CPV	Concentrated photovoltaics
c-Si	Crystalline silicon
C-V	Capacitance-voltage
CVD	Chemical vapor deposition
Cz	Czochralski
EQE	External quantum efficiency
F-D	Fermi-Dirac
FGA	Forming gas anneal
FTIR	Fourier transform infrared spectroscopy
FZ	Float zone
G-V	Conductance-voltage
IEEE	Institute of Electrical and Electronics Engineers
IFE	Institute for Energy Technology
IQE	Internal quantum efficiency
I-V	Current-voltage
I-V	Current-voltage
MIS	Metal-insulator-semiconductor
PC1D	A semiconductor device simulation software
PECVD	Plasma enhanced chemical vapor deposition
PL	Photoluminescence
PL-I	Photoluminescence imaging
PL-V	Photoluminescence imaging under applied bias
PV	Photovoltaic
QSS-μPCD	Quasi-steady state microwave photoconductance decay
QSSPC	Quasi-steady state photoconductance
QSSPL	Quasi-steady state photoluminescence
RCA	Radio corporation of America
RF	Radio frequency
SCR	Space charge region
SDR	Subsurface damaged region
SRH	Shockley-Read Hall
SRV	Surface recombination velocity
VASE	Variable angle spectroscopic ellipsometry
μPCD	Microwave detected photoconductance decay

BIBLIOGRAPHY

[1] European Photovoltaic Industry Association, "Global Market Outlook for Photovoltaics 2013-2017," 2013.

[2] International Energy Agency, "Technology Roadmap Solar photovoltaic energy," 2010.

[3] Semiconductor Equipment and Materials International, "International Technology Roadmap for Photovoltaic (ITRPV) - Results 2012," 2012.

[4] J. Zhao, A. Wang, and M. A. Green, "24·5% Efficiency silicon PERT cells on MCZ substrates and 24·7% efficiency PERL cells on FZ substrates," *Prog. Photovoltaics Res. Appl.*, vol. 7, no. 6, pp. 471–474, Nov. 1999.

[5] S. Rein, *Lifetime Spectroscopy - A Method of Defect Characterization in Silicon for Photovoltaic Applications*. Springer-Verlag, 2005.

[6] A. G. Aberle, *Crystalline silicon solar cells - Advanced surface passivation and analysis*. Centre for Photovoltaic engineering, University of New South Wales, 1999.

[7] D. K. Schroder, *Semiconductor material and device characterization*, 3rd ed. John Wiley & Sons, Inc., 2006, p. 334.

[8] T. Trupke, M. A. Green, P. Wurfel, P. P. Altermatt, A. Wang, J. Zhao, and R. Corkish, "Temperature dependence of the radiative recombination coefficient of intrinsic crystalline silicon," *J. Appl. Phys.*, vol. 94, no. 8, pp. 4930–4937, Oct. 2003.

[9] T. Matsusue and H. Sakaki, "Radiative recombination coefficient of free carriers in GaAs-AlGaAs quantum wells and its dependence on temperature," *Appl. Phys. Lett.*, vol. 50, no. 20, p. 1429, 1987.

[10] M. J. Kerr and A. Cuevas, "General parameterization of Auger recombination in crystalline silicon," *J. Appl. Phys.*, vol. 91, no. 4, pp. 2473–2480, Feb. 2002.

[11] A. Richter, S. W. Glunz, F. Werner, J. Schmidt, and A. Cuevas, "Improved quantitative description of Auger recombination in crystalline silicon," *Phys. Rev. B*, vol. 86, no. 16, p. 165202, Oct. 2012.

[12] W. Shockley and W. T. Read Jr., "Statistics of the Recombinations of Holes and Electrons," *Phys. Rev.*, vol. 87, no. 5, pp. 835–842, Sep. 1952.

[13] R. Hall, “Electron-Hole Recombination in Germanium,” *Phys. Rev.*, vol. 87, no. 2, pp. 387–387, Jul. 1952.
[14] A. S. Grove and D. J. Fitzgerald, “Surface effects on p-n junctions: Characteristics of surface space-charge regions under non-equilibrium conditions,” *Solid. State. Electron.*, vol. 9, no. 8, pp. 783–806, 1966.
[15] D. J. Fitzgerald and a. S. Grove, “Surface recombination in semiconductors,” *IEEE Trans. Electron Devices*, vol. 15, no. 6, pp. 426–427, Jun. 1968.
[16] R. B. M. Girisch, R. P. Mertens, and R. F. De Keersmaecker, “Determination of Si-SiO2 interface recombination parameters using a gate-controlled point-junction diode under illumination,” *IEEE Trans. Electron Devices*, vol. 35, no. 2, pp. 203–222, 1988.
[17] S. Dauwe, “Low temperature surface passivation of crystalline silicon and its applications on the rear side of solar cells,” PhD thesis, University of Hannover, 2004.
[18] A. G. Aberle, S. Glunz, and W. Warta, “Impact of illumination level and oxide parameters on Shockley--Read--Hall recombination at the Si-SiO2 interface,” *J. Appl. Phys.*, vol. 71, no. 9, pp. 4422–4431, 1992.
[19] S. W. Glunz, D. Biro, S. Rein, and W. Warta, “Field-effect passivation of the SiO2/Si interface,” *J. Appl. Phys.*, vol. 86, no. 1, p. 683, 1999.
[20] J. Schmidt and A. G. Aberle, “Carrier recombination at silicon--silicon nitride interfaces fabricated by plasma-enhanced chemical vapor deposition,” *J. Appl. Phys.*, vol. 85, no. 7, pp. 3626–3633, 1999.
[21] S. De Wolf, S. Olibet, and C. Ballif, “Stretched-exponential a-Si:H/c-Si interface recombination decay,” *Appl. Phys. Lett.*, vol. 93, no. 3, pp. 32101–32103, Jul. 2008.
[22] J. Schmidt, F. Werner, B. Veith, D. Zielke, S. Steingrube, P. P. Altermatt, S. Gatz, T. Dullweber, and R. Brendel, “Advances in the Surface Passivation of Silicon Solar Cells,” *Energy Procedia*, vol. 15, no. 2011, pp. 30–39, Jan. 2012.
[23] S. Mack, A. Wolf, C. Brosinsky, S. Schmeisser, A. Kimmerle, P. Saint-Cast, M. Hofmann, and D. Biro, “Silicon Surface Passivation by Thin Thermal Oxide/PECVD Layer Stack Systems,” *Photovoltaics, IEEE Journal of*, vol. 1, no. 2. pp. 135–145, 2011.
[24] S. Steingrube, P. P. Altermatt, D. S. Steingrube, J. Schmidt, and R. Brendel, “Interpretation of recombination at c-Si/SiNx interfaces by surface damage,” *J. Appl. Phys.*, vol. 108, no. 1, p. 014506, 2010.
[25] A. B. Sproul, “Dimensionless solution of the equation describing the effect of surface recombination on carrier decay in semiconductors,” *J. Appl. Phys.*, vol. 76, no. 5, pp. 2851–2854, 1994.
[26] A. G. Aberle, “Surface passivation of crystalline silicon solar cells: a review,” *Prog. Photovoltaics Res. Appl.*, vol. 8, no. 5, pp. 473–487, Sep. 2000.
[27] W. D. Eades and R. M. Swanson, “Calculation of surface generation and recombination at the Si-Si02 interface,” *J. Appl. Phys.*, vol. 58, no. December, pp. 4267–4276, 1985.
[28] E. Yablonovitch, D. Allara, C. Chang, T. Gmitter, and T. Bright, “Unusually Low Surface-Recombination Velocity on Silicon and Germanium Surfaces,” *Phys. Rev. Lett.*, vol. 57, no. 2, pp. 249–252, Jul. 1986.

[29] M. A. Green, *Solar cells - Operating principles, technology and system applications*. The university of New South Wales, 1982.
[30] G. Dingemans and W. M. M. Kessels, "Status and prospects of Al2O3-based surface passivation schemes for silicon solar cells," *J. Vac. Sci. Technol. A Vacuum, Surfaces, Film.*, vol. 30, no. 4, p. 040802, 2012.
[31] M. Rahman and S. Khan, "Advances in surface passivation of c-Si solar cells," *Mater. Renew. Sustain. Energy C7 - 1*, vol. 1, no. 1, pp. 1–11 LA – English, 2012.
[32] S. De Wolf, A. Descoeudres, Z. C. Holman, and C. Ballif, "High-efficiency Silicon Heterojunction Solar Cells: A Review," *Green*, vol. 2, no. 1, pp. 7–24, 2012.
[33] F. Duerinckx and J. Szlufcik, "Defect passivation of industrial multicrystalline solar cells based on PECVD silicon nitride," *Sol. Energy Mater. Sol. Cells*, vol. 72, no. 1–4, pp. 231–246, 2002.
[34] T. Lauinger, J. Moschner, A. G. Aberle, and R. Hezel, "Optimization and characterization of remote plasma-enhanced chemical vapor deposition silicon nitride for the passivation of p-type crystalline silicon surfaces," *J. Vac. Sci. Technol. A Vacuum, Surfaces, Film.*, vol. 16, no. 2, pp. 530–543, 1998.
[35] W. Soppe, H. Rieffe, and A. Weeber, "Bulk and surface passivation of silicon solar cells accomplished by silicon nitride deposited on industrial scale by microwave PECVD," *Prog. Photovoltaics Res. Appl.*, vol. 13, no. 7, pp. 551–569, 2005.
[36] I. G. Romijn, W. J. Soppe, H. C. Rieffe, A. R. Burgers, and A. W. Weber, "Passivation mc-Si solar cells using Sinx:H: from magic to physics," in *20th European Photovoltaic Solar Energy Conference*, 2005, pp. 1352–1355.
[37] J. F. Lelièvre, E. Fourmond, A. Kaminski, O. Palais, D. Ballutaud, and M. Lemiti, "Study of the composition of hydrogenated silicon nitride SiNx:H for efficient surface and bulk passivation of silicon," *Sol. Energy Mater. Sol. Cells*, vol. 93, no. 8, pp. 1281–1289, 2009.
[38] H. Mäckel and R. Lüdemann, "Detailed study of the composition of hydrogenated SiNx layers for high-quality silicon surface passivation," *J. Appl. Phys.*, vol. 92, no. 5, p. 2602, 2002.
[39] S. De Wolf, G. Agostinelli, G. Beaucarne, and P. Vitanov, "Influence of stoichiometry of direct plasma-enhanced chemical vapor deposited SiNx films and silicon substrate surface roughness on surface passivation," *J. Appl. Phys.*, vol. 97, no. 6, pp. 63303–63308, 2005.
[40] A. G. Aberle, "Overview on SiN surface passivation of crystalline silicon solar cells," *Sol. Energy Mater. Sol. Cells*, vol. 65, no. 1–4, pp. 239–248, 2001.
[41] D. T. Krick, P. M. Lenahan, and J. Kanicki, "Electrically active point defects in amorphous silicon nitride: An illumination and charge injection study," *J. Appl. Phys.*, vol. 64, no. 7, p. 3558, 1988.
[42] G. Beylier, S. Bruyere, P. Mora, and G. Ghibaudo, "New Characterization Methodology of Borderless Silicon Nitride Charge Kinetics Using C-V Hysteresis Loops," *J. Electrochem. Soc.*, vol. 155, no. 5, pp. H273–H279, 2008.

[43] T. Lauinger, J. Schmidt, A. G. Aberle, and R. Hezel, "Record low surface recombination velocities on 1 Omega cm p-silicon using remote plasma silicon nitride passivation," *Appl. Phys. Lett.*, vol. 68, no. 9, pp. 1232–1234, 1996.

[44] S. Dauwe, L. Mittelstädt, A. Metz, and R. Hezel, "Experimental evidence of parasitic shunting in silicon nitride rear surface passivated solar cells," *Prog. Photovoltaics Res. Appl.*, vol. 10, no. 4, pp. 271–278, 2002.

[45] M. A. Green, K. Emery, Y. Hishikawa, W. Warta, and E. D. Dunlop, "Solar cell efficiency tables (version 43)," *Prog. Photovoltaics Res. Appl.*, vol. 22, no. 1, pp. 1–9, Jan. 2014.

[46] H. Li and S. R. Wenham, "Influence of a-Si:H deposition power on surface passivation property and thermal stability of a-Si:H/SiNx:H stacks," *AIP Adv.*, vol. 2, no. 2, p. 022106, 2012.

[47] A. G. Aberle, S. W. Glunz, A. W. Stephens, and M. A. Green, "High-eficiency silicon solar cells: Si/SiO2, interface parameters and their impact on device performance," *Prog. Photovoltaics Res. Appl.*, vol. 2, no. 4, pp. 265–273, Oct. 1994.

[48] a. W. Stephens, a. G. Aberle, and M. a. Green, "Surface recombination velocity measurements at the silicon–silicon dioxide interface by microwave-detected photoconductance decay," *J. Appl. Phys.*, vol. 76, no. 1, p. 363, 1994.

[49] D. Biro, S. Mack, A. Wolf, A. Lemke, U. Belledin, D. Erath, B. Holzinger, E. A. Wotke, M. Hofmann, L. Gautero, S. Nold, J. Rentsch, and R. Preu, "Thermal oxidation as a key technology for high efficiency screen printed industrial silicon solar cells," *Photovoltaic Specialists Conference (PVSC), 2009 34th IEEE*. pp. 1594–1599, 2009.

[50] G. Agostinelli, A. Delabie, P. Vitanov, Z. Alexieva, H. F. W. Dekkers, S. De Wolf, and G. Beaucarne, "Very low surface recombination velocities on p-type silicon wafers passivated with a dielectric with fixed negative charge," *Sol. Energy Mater. Sol. Cells*, vol. 90, no. 18–19, pp. 3438–3443, Nov. 2006.

[51] B. Hoex, S. B. S. Heil, E. Langereis, M. C. M. van de Sanden, and W. M. M. Kessels, "Ultralow surface recombination of c-Si substrates passivated by plasma-assisted atomic layer deposited Al[sub 2]O[sub 3]," *Appl. Phys. Lett.*, vol. 89, no. 4, pp. 42112–42113, 2006.

[52] G. Dingemans, R. Seguin, P. Engelhart, M. C. M. van de Sanden, and W. M. M. Kessels, "Silicon surface passivation by ultrathin Al2O3 films synthesized by thermal and plasma atomic layer deposition," *Phys. Status Solidi – Rapid Res. Lett.*, vol. 4, no. 1–2, pp. 10–12, Feb. 2010.

[53] P. Repo, A. Haarahiltunen, L. Sainiemi, M. Yli-Koski, H. Talvitie, M. C. Schubert, and H. Savin, "Effective Passivation of Black Silicon Surfaces by Atomic Layer Deposition," *Photovoltaics, IEEE Journal of*, vol. 3, no. 1. pp. 90–94, 2013.

[54] P. Saint-Cast, D. Kania, M. Hofmann, J. Benick, J. Rentsch, and R. Preu, "Very low surface recombination velocity on <equation>p</equation>-type <equation>c</equation>-Si by high-rate plasma-deposited aluminum oxide," *Applied Physics Letters*, vol. 95, no. 15. pp. 151502–151503, 2009.

[55] L. E. Black and K. R. McIntosh, “Surface passivation of c-Si by atmospheric pressure chemical vapor deposition of Al<inf>2</inf>O<inf>3</inf>,” *Applied Physics Letters*, vol. 100, no. 20. pp. 202105–202107, 2012.

[56] T.-T. Li and A. Cuevas, “Effective surface passivation of crystalline silicon by rf sputtered aluminum oxide,” *Phys. status solidi – Rapid Res. Lett.*, vol. 3, no. 5, pp. 160–162, Jul. 2009.

[57] B. Hoex, J. J. H. Gielis, M. C. M. van de Sanden, and W. M. M. Kessels, “On the c-Si surface passivation mechanism by the negative-charge-dielectric Al[sub 2]O[sub 3],” *J. Appl. Phys.*, vol. 104, no. 11, p. 113703, 2008.

[58] J. Schmidt, A. Merkle, R. Brendel, B. Hoex, M. C. M. Van De Sanden, and W. M. M. Kessels, “Surface Passivation of High-efficiency Silicon Solar Cells by Atomic-layer-deposited Al 2 O 3,” no. March, pp. 461–466, 2008.

[59] B. Hoex, J. Schmidt, R. Bock, P. P. Altermatt, M. C. M. van de Sanden, and W. M. M. Kessels, “Excellent passivation of highly doped p-type Si surfaces by the negative-charge-dielectric Al2O3,” *Applied Physics Letters*, vol. 91, no. 11. pp. 112103–112107, 2007.

[60] J. Schmidt, M. Kerr, and A. Cuevas, “Surface passivation of silicon solar cells using plasma-enhanced chemical-vapour-deposited SiN films and thin thermal SiO2 /plasma SiN stacks,” *Semicond. Sci. Technol.*, vol. 16, no. 3, p. 164, 2001.

[61] M. Hofman, S. Kambor, C. Schmidt, D. Grambole, J. Rentsch, S. W. Glunz, and R. Preu, “PECVD-ONO: A New Deposited Firing Stable Rear Surface Passivation Layer System for Crystalline Silicon Solar Cells,” *Adv. Optoelectron.*, vol. 2008, 2008.

[62] G. Dingemans, M. M. Mandoc, S. Bordihn, M. C. M. van de Sanden, and W. M. M. Kessels, “Effective passivation of Si surfaces by plasma deposited SiO[sub x]/a-SiN[sub x]:H stacks,” *Appl. Phys. Lett.*, vol. 98, no. 22, p. 222102, May 2011.

[63] H. Li, B. Hallam, and S. R. Wenham, “Comparative study of PECVD deposited a-Si:H / SiNx:H double passivating layer on Cz crystalline Si substrate,” 2011, pp. 1481–1485.

[64] S. Gatz, H. Plagwitz, P. P. Altermatt, B. Terheiden, and R. Brendel, “Thermal stability of amorphous silicon/silicon nitride stacks for passivating crystalline silicon solar cells,” *Appl. Phys. Lett.*, vol. 93, no. 17, pp. 173502–173503, Oct. 2008.

[65] M. Hofmann, C. Schmidt, N. Kohn, J. Rentsch, S. W. Glunz, and R. Preu, “Stack system of PECVD amorphous silicon and PECVD silicon oxide for silicon solar cell rear side passivation,” *Prog. Photovoltaics Res. Appl.*, vol. 16, no. 6, pp. 509–518, 2008.

[66] J. Schmidt, B. Veith, and R. Brendel, “Effective surface passivation of crystalline silicon using ultrathin Al2O3 films and Al2O3/SiNx stacks,” *Phys. status solidi – Rapid Res. Lett.*, vol. 3, no. 9, pp. 287–289, Nov. 2009.

[67] J. Schmidt, A. Merkle, R. Brendel, B. Hoex, M. C. M. van de Sanden, and W. M. M. Kessels, “Surface passivation of high-efficiency silicon solar cells by atomic-layer-deposited Al2O3,” *Prog. Photovoltaics Res. Appl.*, vol. 16, no. 6, pp. 461–466, Sep. 2008.

[68] S. Dauwe, J. Schmidt, A. Metz, and R. Hezel, "Fixed charge density in silicon nitride films on crystalline silicon surfaces under illumination," *Conf. Rec. Twenty-Ninth IEEE Photovolt. Spec. Conf. 2002.*, pp. 162–165.

[69] D. A. Clugston and P. A. Basore, "PC1D version 5: 32-bit solar cell modeling on personal computers," *Photovoltaic Specialists Conference, 1997., Conference Record of the Twenty-Sixth IEEE*. pp. 207–210, 1997.

[70] B. G. Streetman and S. K. Banerjee, *Solid State Electronic Devices*. Pearson Prentice Hall, 2006.

[71] W. Kern, "The Evolution of Silicon Wafer Cleaning Technology," *J. Electrochem. Soc.*, vol. 137, no. 6, pp. 1887–1892, 1990.

[72] S. A. Campbell, *Fabrication Engineering at the Micro and Nanoscale*. OUP USA, 2008.

[73] R. A. Sinton, A. Cuevas, and M. Stuckings, "Quasi-Steady-State PhotoConductance, A new method for solar cell material and device characterization," in *25th IEEE Photovoltaic Specialists Conference*, 1996, p. 457.

[74] H. Nagel, C. Berge, and A. G. Aberle, "Generalized analysis of quasi-steady-state and quasi-transient measurements of carrier lifetimes in semiconductors," *J. Appl. Phys.*, vol. 86, no. 11, pp. 6218–6221, 1999.

[75] M. Kunst and G. Beck, "The study of charge carrier kinetics in semiconductors by microwave conductivity measurements," *J. Appl. Phys.*, vol. 60, no. 10, p. 3558, 1986.

[76] M. Wilson, P. Edelman, J. Lagowski, S. Olibet, and V. Mihailetchi, "Improved QSS-μPCD measurement with quality of decay control: Correlation with steady-state carrier lifetime," *Sol. Energy Mater. Sol. Cells*, vol. 106, pp. 66–70, Nov. 2012.

[77] T. Trupke, R. A. Bardos, M. C. Schubert, and W. Warta, "Photoluminescence imaging of silicon wafers," *Appl. Phys. Lett.*, vol. 89, no. 4, pp. 44103–44107, 2006.

[78] P. Wurfel, T. Trupke, T. Puzzer, E. Schaffer, W. Warta, and S. W. Glunz, "Diffusion lengths of silicon solar cells from luminescence images," *Journal of Applied Physics*, vol. 101, no. 12. p. 123110, 2007.

[79] T. Trupke, J. Nyhus, and J. Haunschild, "Luminescence imaging for inline characterisation in silicon photovoltaics," *Phys. status solidi – Rapid Res. Lett.*, vol. 5, no. 4, pp. 131–137, Apr. 2011.

[80] M. D. Abbott, J. E. Cotter, F. W. Chen, T. Trupke, R. A. Bardos, and K. C. Fisher, "Application of photoluminescence characterization to the development and manufacturing of high-efficiency silicon solar cells," *J. Appl. Phys.*, vol. 100, no. 11, p. 114514, Dec. 2006.

[81] S. Herlufsen, J. Schmidt, D. Hinken, K. Bothe, and R. Brendel, "Photoconductance-calibrated photoluminescence lifetime imaging of crystalline silicon," *Phys. status solidi - Rapid Res. Lett.*, vol. 2, no. 6, pp. 245–247, Dec. 2008.

[82] J. A. Giesecke, M. C. Schubert, B. Michl, F. Schindler, and W. Warta, "Minority carrier lifetime imaging of silicon wafers calibrated by quasi-steady-state photoluminescence," *Sol. Energy Mater. Sol. Cells*, vol. 95, no. 3, pp. 1011–1018, 2011.

[83] T. Trupke, R. A. Bardos, and M. D. Abbott, “Self-consistent calibration of photoluminescence and photoconductance lifetime measurements,” *Appl. Phys. Lett.*, vol. 87, no. 18, p. 184102, Oct. 2005.
[84] D. Kiliani, G. Micard, B. Steuer, B. Raabe, A. Herguth, and G. Hahn, “Minority charge carrier lifetime mapping of crystalline silicon wafers by time-resolved photoluminescence imaging,” *J. Appl. Phys.*, vol. 110, no. 5, p. 054508, 2011.
[85] E. . Nicollian and J. R. Brews, *MOS (metal oxide semiconductor) physics and technology.* John Wiley & Sons, Inc., 2003, p. 423.
[86] J. A. Woollam and P. G. Snyder, “Fundamentals and applications of variable angle spectroscopic ellipsometry,” *Mater. Sci. Eng. B*, vol. 5, no. 2, pp. 279–283, 1990.
[87] M. A. Green, *Silicon solar cells: advanced principles and practice*. Centre for Photovoltaic Devices and Systems, University of New South Wales, 1995.
[88] J. Nelson, *The physics of solar cells*. Imperial College Press, 2003.
[89] P. Würfel and U. Würfel, *Physics of Solar Cells: From Basic Principles to Advanced Concepts*. Wiley, 2009.
[90] E. Yablonovitch, R. M. Swanson, W. D. Eades, and B. R. Weinberger, “Electron-hole recombination at the Si-SiO[sub 2] interface,” *Appl. Phys. Lett.*, vol. 48, no. 3, pp. 245–247, 1986.
[91] W. E. Jellett and K. J. Weber, “Accurate measurement of extremely low surface recombination velocities on charged, oxidized silicon surfaces using a simple metal-oxide-semiconductor structure,” *Appl. Phys. Lett.*, vol. 90, no. 4, p. 042104, 2007.
[92] E. Suzuki, H. Takato, K. Ishii, and Y. Hayashi, “Evaluation of the Si-SiO 2 Interface by the Measurement of the Surface Recombination Velocity S by the Dual-Mercury Probe Method,” *Jpn. J. Appl. Phys.*, vol. 29, no. Part 2, No. 12, pp. L2300–L2303, Dec. 1990.
[93] M. Schofthaler, R. Brendel, G. Langguth, and J. H. Werner, “High-quality surface passivation by corona-charged oxides for semiconductor surface characterization,” in *1st World Conference on Photovoltaic Energy Conversion*, 1994, vol. 2, p. 1509.
[94] M. Mandoc, M. Adams, G. Dingemans, N. Terlinden, M. van de Sanden, and W. Kessels, “Corona charging and optical second-harmonic generation studies of the field-effect passivation of c-SI by Al2O3 films,” in *Photovoltaic Specialists Conference (PVSC), 2010 35th IEEE*, pp. 003200–003204.
[95] S. Baker-Finch, “Characterisation of corona-charged oxide-passivated silicon,” in *3rd International Solar*, 2008, no. November.
[96] M. Wilson, J. Lagowski, P. Edelman, F. Korsos, G. Nadudvari, Z. Kiss, J. Schmauder, V. Mihailetchi, and S. Olibet, “Unified Lifetime Metrology and Photoluminescence Imaging of Passivation Defects for Silicon PV,” *Energy Procedia*, vol. 38, pp. 209–215, Jan. 2013.
[97] A. O. Si, W. Liang, K. J. Weber, D. Suh, and Y. Ren, “Investigation of field-effect passivation and interface state parameters at the Al2O3/Si interface,” pp. 1–4.
[98] H. Jin, K. J. Weber, N. C. Dang, and W. E. Jellett, “Defect generation at the Si–SiO2 interface following corona charging,” *Appl. Phys. Lett.*, vol. 90, no. 26, p. 262109, 2007.

[99] F. Kløw, H. Haug, and S. E. Foss, "Surface Recombination Velocity Measurements of Metallized Surfaces by Photoluminescence Imaging," *Energy Procedia*, vol. 43, pp. 18–26, 2013.

[100] J. Müller, K. Bothe, S. Herlufsen, H. Hannebauer, R. Ferré, and R. Brendel, "Reverse saturation current density imaging of highly doped regions in silicon: A photoluminescence approach," *Sol. Energy Mater. Sol. Cells*, vol. 106, no. 0, pp. 76–79, Nov. 2012.

[101] Mathworks, "Optimization Toolbox User's Guide," 2009. [Online]. Available: http://www.mathworks.se/help/toolbox/optim/.

[102] M. She, T. King, S. Member, C. Hu, W. Zhu, Z. Luo, and J. Han, "JVD silicon nitride as tunnel dielectric in p-channel flash memory," *IEEE Electron Device Lett.*, vol. 23, no. 2, pp. 91–93, 2002.

[103] K. J. Weber and H. Jin, "Improved silicon surface passivation achieved by negatively charged silicon nitride films," *Appl. Phys. Lett.*, vol. 94, no. 6, p. 063509, 2009.

[104] P. P. Altermatt, J. O. Schumacher, A. Cuevas, M. J. Kerr, S. W. Glunz, R. R. King, G. Heiser, and A. Schenk, "Numerical modeling of highly doped Si:P emitters based on Fermi–Dirac statistics and self-consistent material parameters," *J. Appl. Phys.*, vol. 92, no. 6, p. 3187, Aug. 2002.

[105] A. Schenk, "Finite-temperature full random-phase approximation model of band gap narrowing for silicon device simulation," *J. Appl. Phys.*, vol. 84, no. 7, p. 3684, 1998.

[106] D. B. M. Klaassen, "A unified mobility model for device simulation," *Electron Devices Meeting, 1990. IEDM '90. Technical Digest., International*. pp. 357–360, 1990.

[107] K. R. McIntosh and P. P. Altermatt, "A freeware 1D emitter model for silicon solar cells," in *2010 35th IEEE Photovoltaic Specialists Conference*, 2010, pp. 002188–002193.

I

II

JOURNAL OF APPLIED PHYSICS **114**, 174502 (2013)

Modulating the field-effect passivation at the SiO_2/c-Si interface: Analysis and verification of the photoluminescence imaging under applied bias method

Halvard Haug,[1,a)] Sara Olibet,[2] Ørnulf Nordseth,[1] and Erik Stensrud Marstein[1,3]
[1]*Institute for Energy Technology, Instituttveien 18, 2007 Kjeller, Norway*
[2]*International Solar Energy Research Center-ISC Konstanz, Konstanz, Germany*
[3]*Department of Physics, University of Oslo, Pb 1048 Blindern 0316 Oslo, Norway*

(Received 21 August 2013; accepted 14 October 2013; published online 1 November 2013)

In this paper, we study the surface passivation properties of thermally oxidized silicon wafers with controlled surface band bending, using a recently developed characterization technique combining calibrated photoluminescence imaging with the application of an external voltage over the rear side passivation layer. Various aspects of the technique and possible errors in the determination of the effective surface recombination velocity are discussed, including lateral carrier diffusion, leakage currents, and optical effects related to the presence of metal electrodes on the investigated samples. In order to quantitatively describe the recombination activity at the SiO_2/c-Si interface and the effect of fixed charges in the oxide layer, the measured effective carrier lifetime vs. voltage curves have been analyzed in the framework of an extended Shockley-Read Hall recombination model. Furthermore, the results have been compared with corresponding results from microwave detected photoconductance decay measurements after depositing corona charges. We find an excellent agreement between the two techniques and between complementary measurements of the oxide charge density. Photoluminescence imaging under applied bias gives fast and repeatable measurements and allows for simultaneous data collection from multiple areas on the sample, and has thus been proven to be powerful tool for quantitative characterization of surface passivation layers. © *2013 AIP Publishing LLC*. [http://dx.doi.org/10.1063/1.4827417]

I. INTRODUCTION

Currently, there is a large research activity focusing on the implementation of effective rear side surface passivation in the production of high efficiency Si solar cells. Most of these approaches use thin dielectric layers or stacks deposited by various thin film deposition methods like plasma enhanced chemical vapor deposition (PECVD) or atomic layer deposition (ALD). High-quality surface passivation may also be achieved by thermal oxidation, and thin SiO_2 films have been demonstrated in industrial pilot production.[1] The passivating properties of these Si solar cell passivation layers are however strongly dependent on surface quality of the Si substrate as well as on the processing conditions, and the results are thus generally not directly transferable between different processing systems. Accurate characterization methods allowing for a fundamental understanding of the recombination processes for the specific passivation layer in question are therefore of high importance.

The surface recombination velocity (SRV) at a Si surface can be reduced by lowering the interface defect density (chemical passivation) or by reducing the concentration of one type of charge carriers in the region near the surface with a built-in electric field (field-effect passivation).[2] In solar cells, such a surface band bending is normally achieved by incorporating dielectric passivation layers with fixed charges, such as a-Si:N_x:H (positive charges) or a-AlO_x (negative charges). The surface potential, and thus the SRV, may also be modulated directly by applying voltage to a gate electrode placed on top of a dielectric passivation layer[3,4] or by deposition of charged ions on the surface in a corona discharge chamber.[5,6] The corona charge method has the advantage of being non-invasive (the charges can be washed off by a polar solvent), and has traditionally been the method of choice for characterization of dielectric passivation layers in solar cells. Also, gate electrodes on the sample surface will typically obstruct either the optical excitation or the photoconductance measurement that are needed in most techniques used for minority carrier lifetime measurements, like quasi-steady state photoconductance (QSSPC).

Recently, we proposed a new technique for analyzing the surface recombination for passivated silicon substrates.[7] The technique is based on measurements of the effective carrier lifetime in a photoluminescence (PL) imaging setup[8] while a voltage is applied over the rear side passivation layer. In contrast to corona charging techniques, PL imaging under applied bias, hereafter referred to as PL-V, requires metal electrodes to be produced on the sample surface. However, the PL-V method allows for very fast measurements and simultaneous data collection from multiple areas on the sample. By employing a fast electrode deposition, for instance by the application of liquid metal electrodes, the PL-V method may thus be used for fast, automated, and spatially resolved characterization of Si surface passivation layers, possibly allowing for in-line control of selected

[a)]Author to whom correspondence should be addressed. Electronic mail: halvard.haug@ife. Telephone: +47 99486756.

wafers during solar cell fabrication. The technique also has the advantage of allowing for repeated measurement scans between inversion and accumulation, which can be recorded with little or no influence of the measurement history of the sample.

In this paper, we compare the results obtained by the PL-V method with quasi-steady state microwave detected photoconductance decay (QSS-μPCD) measurements performed after controlled deposition of corona charges on the surface.[9] Various aspects of the two measurement techniques and important uncertainties in the determination of the effective SRV are discussed. Finally, the measured data is compared to both an extended Shockley-Read Hall (SRH) recombination model and complementary measurements of the oxide charge density.

II. EXPERIMENTAL DETAILS

A. Sample preparation

Double-side polished float-zone (FZ) Si(100) wafers with a high bulk lifetime (>3 ms) were used for the experiments. Samples were made from both p-type and n-type wafers with measured doping concentrations of $N_A = 5.4 \times 10^{15}\,\mathrm{cm}^{-3}$ and $N_D = 1.7 \times 10^{15}\,\mathrm{cm}^{-3}$, respectively. After carrying out a standard RCA (1 + 2) clean[10] and 30 s immersion in a 5% HF solution, the wafers were loaded into a tube furnace and oxidized in dry O_2 at 1000 °C for 60 min. The oxide thickness was measured by variable-angle spectroscopic ellipsometry and found to be 70–72 nm uniformly across the wafers. In order to get a comparable passivation quality for the two samples, the p-type wafer received a post-oxidation forming gas (5% H_2, 95% N_2) anneal at 400 °C for 30 min. The thermal SiO_2 layers on these samples provide a stable, high quality surface passivation with good dielectric properties and are thus well suited for reviewing the PL-V method and comparing the results with those from other characterization methods.

For the measurements in this paper, two different types of electrodes were deposited onto the oxide layer by thermal evaporation of Al through a shadow mask: 7 mm × 7 mm electrodes were fabricated for the lifetime vs. voltage (PL-V) measurements and 0.45–2.25 mm diameter circular electrodes were fabricated for the capacitance–voltage (C-V) measurements. Finally, a low resistivity contact was made to the Si substrate by grinding down the oxide with P200 sand paper and depositing Ag in the region opposite to the electrodes used for C-V measurements.

B. The PL-V method

A schematic overview of the experimental setup for the PL-V method is shown in Figure 1(a). Steady state carrier lifetime measurements were carried out with a LIS-R1 PL imaging setup from BT imaging with an excitation wavelength of 808 nm and a constant illumination intensity of 17.5 mW/cm^2. The PL intensity was calibrated to the effective lifetime using a QSSPC measurement[11] of a reference region without metal electrodes. An external voltage source was connected to the sample in order to obtain lifetime images with an applied bias over the rear side passivation layer. The excess carrier concentration Δn was then calculated from the PL intensity averaged over the electrode area as described in Ref. 7. The steady state effective lifetime can then be calculated as

$$\tau_{eff} = \frac{\Delta n}{G}, \tag{1}$$

where G is the generation rate per volume. Before calculating the effective lifetime, the PL intensity in the region over the rear side electrodes was divided by a sample-specific correction factor of 1.36 in order to correct for the enhancement of the signal caused by the higher rear side reflectivity (see Sec. IV A for details).

C. QSS-μPCD after corona charging

With the PV-2000 multifunctional metrology platform,[9] corona charge of both polarities was sequentially deposited on top of the dielectric, and the injection level dependent carrier lifetime was measured in-between as shown in Figure 1(b). Surface voltage measurements with a vibrating Kelvin probe were incorporated after each charging step as a means to correct for the dielectric leakage current that neutralizes corona charge. The QSS-μPCD measurement combines

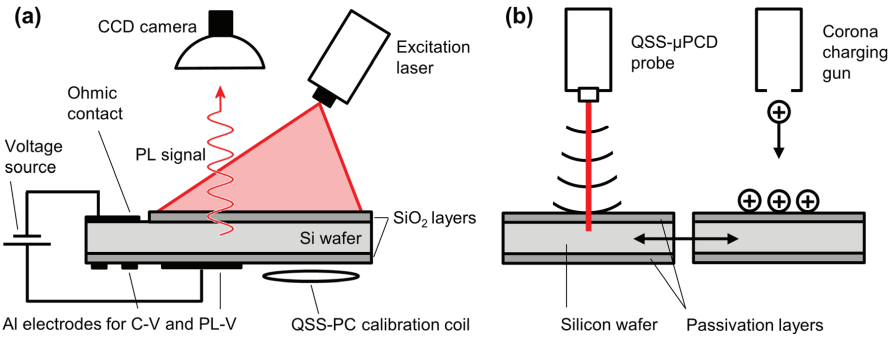

FIG. 1. Schematic overview of the experimental setup for (a) the PL-V method and (b) QSS-μPCD measurements after controlled deposition of corona charges.

scanning of near steady-state generation and pulsed laser excited microwave reflectance PCD monitoring. The combination of corona charging and contactless measurement of the contact potential difference (CPD) in the dark and under illumination allows measuring the flat band voltage, the corona charge needed to move the surface barrier from the initial to the flat band voltage, the interface trap density distribution in the energy gap and the net interface trapped charge. The capacitance was determined from the voltage change across the dielectric passivation layer caused by the applied corona charge.

The lifetime measured with the QSS-μPCD technique is a differential lifetime, and must therefore be integrated before it can be directly compared to the lifetime measured by QSSPC. The steady state lifetime τ_{ss} at the excess carrier concentration (injection level) Δn_{ss} can be calculated from the differential lifetime τ_{diff} as[12]

$$\tau_{ss} = \Delta n_{ss}\left(\int_0^{\Delta n_{ss}} \tau_{diff}^{-1}(\Delta n)d\Delta n\right)^{-1}. \quad (2)$$

III. MEASUREMENT RESULTS

The SRV of a passivated Si surface is normally calculated from measurements of the effective lifetime, which contains contributions from recombination in the bulk of the wafer and at the two surfaces. In this section, we present and compare lifetime data obtained by the two measurement methods described above. The effective lifetime was measured both as a function of injection level (QSSPC and QSS-μPCD) and as a function of surface potential at a constant generation rate (PL-V and QSS-μPCD measurements after corona charging).

A. Lifetime vs. injection level

The measured differential and steady state lifetime for the p-type and n-type samples are shown as a function of injection level in Figure 2, along with the QSSPC curves used to calibrate the PL-V measurements. The photoconductance decay measurements agree well with the QSSPC curves for injection levels between approximately 3×10^{14} and $2 \times 10^{15}\,\mathrm{cm}^{-3}$. The deviation at high injection levels is caused by lateral carrier diffusion causing a non-uniform carrier profile in the μPCD small spot measurement, whereas the deviation at low intensities is due to a violation of the small perturbation condition underlying the QSS-μPCD method.[13] For the PL-V and QSS-μPCD measurements, a constant generation rate of $G = 2.0 \times 10^{18}\,\mathrm{cm}^{-3}\,\mathrm{s}^{-1}$ was therefore chosen, resulting in injection levels in the validity range of the QSS-μPCD setup.

B. Lifetime vs. surface band bending

In order to compare the lifetime data obtained by the two methods, the corona charge values were converted to equivalent voltages, resulting in the same surface potential. This can be achieved by a simple charge balance: The sum of the oxide built-in charges Q_{ox} and the applied corona charge Q_{cor} must be imaged in the space charge region of the semiconductor as a charge Q_{sc} in order to fulfill the charge neutrality

$$Q_{ox} + Q_{cor} = -Q_{sc}. \quad (3)$$

If a gate electrode is used, Q_{cor} can be replaced with the induced charge in the gate electrode Q_g. Assuming that the oxide charges are located at the Si/SiO_2 interface, Q_g can be expressed as a function of the gate voltage V_g as[3]

$$Q_g = \frac{C_{ox}}{q}(V_g - \psi_s - \phi_{ms}), \quad (4)$$

where C_{ox} is the oxide capacitance, q is the elementary charge, ϕ_{ms} is the metal-semiconductor work function difference, and ψ_s is the surface potential (amount of band bending). Using a work function for Al of 4.1 eV, ϕ_{ms} was calculated to be -0.84 eV and -0.20 eV for the p-type and n-type samples, respectively. The set of equations given by Eqs. (3) and (4) was then solved by setting $Q_{cor} = Q_g$ and inserting experimental values for the oxide charge density Q_{ox} obtained by CPD measurements in combination with corona charging. To account for ψ_s in Eq. (4), we have used the relation between Q_{sc} and ψ_s described in Ref. 4 (note that the numerical values for ψ_s are below ± 0.25 V, resulting in only a small correction). Experimental values for C_{ox} of 4.2 $\mathrm{nF/cm}^2$ measured by the corona/CPD method were used in the calculations. If C_{ox} values obtained from C-V measurements (4.6–4.8 $\mathrm{nF/cm}^2$) are used instead, only a slight narrowing of the QSS-μPCD versus corona curve can be observed in the final result.

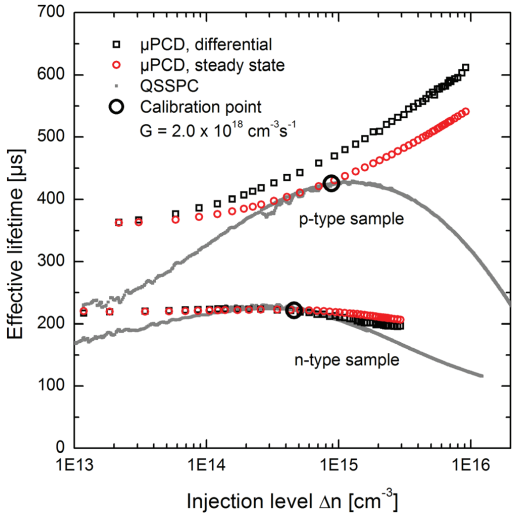

FIG. 2. Effective lifetime as a function of injection level for the n- and p-type samples. QSSPC data (closed symbols) is shown together with QSS-μPCD data (open symbols). The injection level/lifetime point used for calibration of the PL-V data (black circle) corresponds to a generation rate of $G = 2.0 \times 10^{18}\,\mathrm{cm}^{-3}\,\mathrm{s}^{-1}$.

Figure 3 shows the effective lifetime as a function of voltage for both the p-type and n-type samples measured with the two techniques. The voltage was either directly applied in the PL-V method or calculated from the corona charge density as described above. Both samples show the same general behavior: When a small negative voltage (or charge) is applied, the effective lifetime decreases as the external bias compensates the effect of the positive oxide charge density. For increasing negative voltages, the lifetime passes through a minimum corresponding to depletion conditions at the surface, before it increases as the surface is driven into accumulation (p-type sample) or inversion (n-type sample). There is a good correspondence between the two measurement methods for both samples, with the main difference being ~15% higher absolute lifetime values measured with the corona charging method on the n-type sample. This difference is within the experimental error of the calibration of the PL-V curves, caused by inhomogeneous lifetime values across the sample. Moreover, a small shift of ~0.2 V in the position of the minimum is observed for the p-type sample.

The minimum lifetime in the PL-V curve is found to be 102 μs for the p-type sample and 83 μs for the n-type sample. For the n-type sample, the lifetime vs. voltage curves are symmetrical and the curves saturate at a similar level on each side of the lifetime minimum. This indicates a similar capture cross section for electrons σ_n and holes σ_p at the interface traps. For the p-type sample, the curves are slightly asymmetrical, showing highest carrier lifetime for inversion conditions at the surface, indicating that $\sigma_n > \sigma_p$, in agreement with previous findings in the literature.[6]

C. Oxide charge

At flat band conditions, there is no band bending in the semiconductor, i.e., $Q_{sc} = 0$. Since Q_{sc} is monitored during the CPD measurements, Q_{ox} can easily be determined from the applied charge density that causes flat band conditions $Q_{ox} = -Q_{cor,fb}$.[14]

If a gate electrode is used, Q_{ox} can be found from the induced electrode charge at the flat band voltage V_{fb},

$$Q_{ox} = -Q_{g,fb} = C_{ox}(\phi_{ms} - V_{fb})/q\,, \tag{5}$$

where V_{fb} can be calculated from a high frequency C-V measurement.[15] Typical C-V curves used for these calculations and the average values for V_{fb} calculated from 10–12 measurements are shown in Figure 3. The upper part of Table I shows the oxide charge density calculated both by the corona/CPD method and from C-V curves, showing that similar values are obtained by the two techniques. The measured Q_{ox} values are found to be between 2.4 and 2.9 $\times$ 10^{11} cm^{-2} for both samples. Typical Q_{ox} values in the literature are in the range between 1 and 5 $\times$ 10^{11} cm^{-2}.[16] Note that these

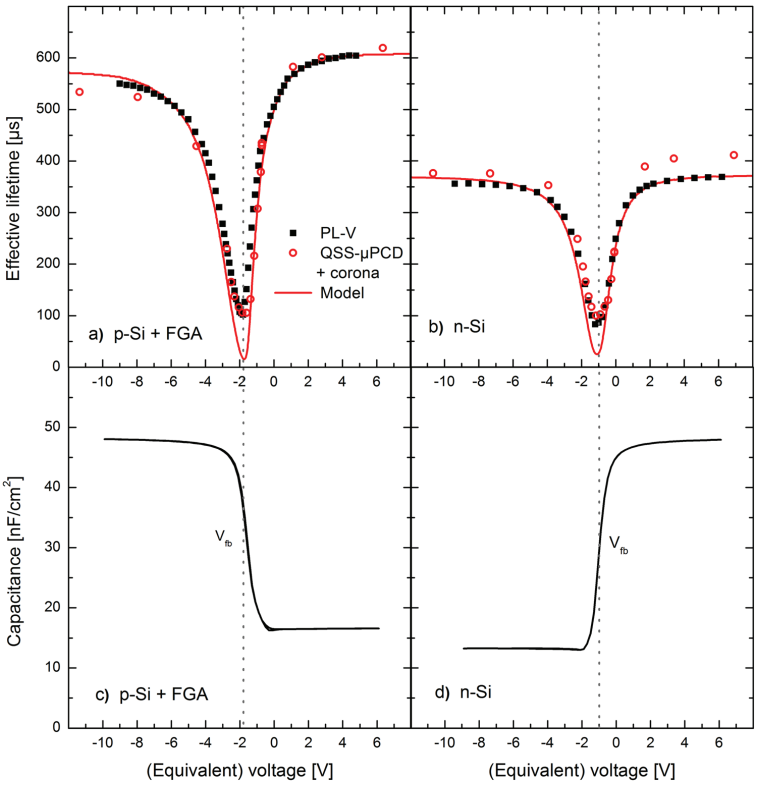

FIG. 3. Top: Effective lifetime as a function of (equivalent) voltage measured with the PL-V method and QSS-μPCD after corona charging at a constant generation rate of $G = 2.0 \times 10^{18}$ cm^{-3} s^{-1} for a (a) p-type and (b) n-type samples. The red solid lines show simulation results of the model described in Sec. V. Bottom: Typical capacitance-voltage curves for a (c) p-type and (d) n-type samples. The average flat band voltage calculated from the C-V measurements is indicated by dotted vertical lines.

TABLE I. Top: Measured values for D_{it} and Q_{ox} for both the p-type sample after forming gas anneal (FGA) and the n-type sample, together with the corona charge needed to compensate the field-effect passivation. D_{it} values are measured in the middle of the band gap by CPD measurements, whereas Q_{ox} values are determined both from CPD measurements after corona charging and C-V measurements. The numbers obtained by C-V are average values and uncertainties are calculated as two standard deviations from 10–12 measurements on different electrodes. Bottom: Fitting parameters for the extended SRH model used to calculate the curves presented in Figures 3 and 9.

Experimental values

Parameter	Description	Unit	p-Si + FGA	n-Si
D_{it}	Density of interface states	cm^{-2}/eV	2.6×10^{10}	1.2×10^{11}
Q_{cor} at τ_{min}	Corona charge at τ_{min}	cm^{-2}	-2.9×10^{11}	-2.5×10^{11}
Q_{ox}	Oxide charge (from CPD)	cm^{-2}	2.7×10^{11}	2.4×10^{11}
Q_{ox}	Oxide charge (from C-V)	cm^{-2}	$(2.8 \pm 0.2) \times 10^{11}$	$(2.7 \pm 0.4) \times 10^{11}$

Fitting parameters for SRH model

Parameter	Description	Unit	p-Si + FGA	n-Si
Q_{ox}	Oxide charge	cm^{-2}	3.0×10^{11}	2.6×10^{11}
σ_n	Electron capture cross section	cm^2	1.5×10^{-14}	7.5×10^{-15}
σ_p	Hole capture cross section	cm^2	2.9×10^{-15}	3.3×10^{-15}
R_p	Equivalent shunt resistance	$\Omega\,cm^2$	260	350

Q_{ox} values are in good agreement with the deposited charge density corresponding to the minimum effective lifetime, and that the measured V_{fb} corresponds well with the minimum in the PL-V curve. This behavior is expected since the surface recombination velocity is highest when the surface concentrations of electrons and holes are comparable (depending on the capture cross sections of the surface defects). This condition is met for depletion conditions at the surface, i.e., in a voltage range close to V_{fb}.

IV. DISCUSSION—DETERMINATION OF THE REAR SRV

In order to obtain a fundamental physical understanding of the recombination process and compare the experimental results with a theoretical model, a precise relation must be found between the measured PL signal and the effective SRV at the rear surface. In this section, we discuss various possible errors that can arise during these calculations and their impact on the final result. The four most important issues that complicate the determination of the rear side SRV in a PL-V measurement are shown schematically in Figure 4: Optical reflection from the rear electrodes, competing recombination processes in the bulk and at the front surface, lateral diffusion of charge carriers, and leakage current through the passivation layer. The latter three of these complications are also relevant for corona charging techniques. However, the combination of imaging capability and direct measurement of the voltage and current for the PL-V method simplifies the quantification of these errors.

A. Effect of increased rear reflectance

The presence of metal electrodes at the rear surface locally increases the rear side reflectance in the measurement region. This causes an enhancement of the PL signal compared to the reference region, which will result in an overestimation of the carrier lifetime if this effect is not accounted for. For the PL-V measurements presented above, this effect was taken into account by experimentally measuring the enhancement of the PL intensity after placing the sample over an Al mirror made by thermal evaporation of 100 nm Al on a glass substrate. In this section, we present a more fundamental and predictive description of the reflection and reabsorption in a typical PL measurement by analytical calculations.

The spectral rate of band-to-band photon emission dB in an energy interval dE can be calculated from the intrinsic absorption coefficient α of Si as[17]

$$dB = C\exp\left(\frac{-\eta}{k_B T}\right) E^2 \alpha(E) \exp\left(\frac{-E}{k_B T}\right) dE, \qquad (6)$$

where η is separation of the quasi-fermi energies (assumed constant in the simulations), k_B is the Boltzmann constant, T is the temperature, and C contains several physical constants. The Si absorption coefficient data was taken from Ref. 18. The PL photons are emitted isotropically in all directions, but for co-planar polished samples like the ones used in this

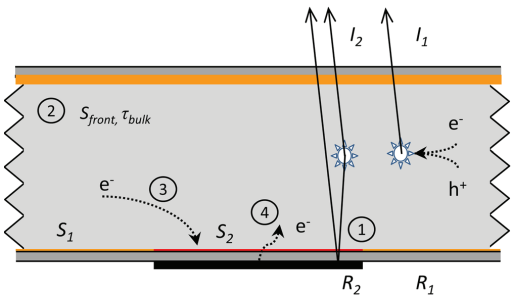

FIG. 4. Schematic overview of various effects that should be taken into account when calculating the effective SRV of the area affected by the gate electrode: (1) Signal enhancement from the increased optical reflectance of the rear side metallized regions, (2) bulk and front surface recombination contributions to the effective lifetime, (3) lateral transport of charge carriers between high and low lifetime regions, and (4) leakage current through the passivation layer.

work only a very narrow range of angles will be able to escape the sample and reach the detector. The problem can therefore be treated in one dimension with negligible error. As described in Ref. 19, the vertical photon flux escaping the front surface is given by

$$\Phi_{ph}(\lambda) = \frac{B_{\perp}(1-R_f)}{\alpha}\frac{(1-e^{-\alpha W})(1+R_b e^{-\alpha W})}{1-R_f R_b e^{-2\alpha W}}, \quad (7)$$

where W is the sample thickness, $B_{\perp}$ is the emitted photon flux in the vertical direction, and R_f and R_b are front and rear side reflectance, respectively. Equation (7) is derived by integrating over the luminescence of an assumed uniform carrier distribution throughout the wafer, taking both multiple internal reflections and reabsorption into account.

Figure 5 shows both the emitted (intrinsic) photon flux and the flux that reaches the detector after being subject to reabsorption and reflection at the sample surfaces. Two different reflectance values representative for the oxidized surface and an oxidized surface with evaporated Al have been used. As seen in the figure, the total integrated signal detected by the camera is increased by 40%, independently of the effective lifetime of the sample. This finding corresponds well with the experimentally determined signal enhancement described above, which was measured to be 36% for the oxidized samples. The deviation may be explained by small errors in the assumed reflectivity values or in the camera sensitivity function (a typical Si CCD sensitivity was used for the calculations).

The PL signal enhancement from locally increased rear reflectance can be avoided experimentally by applying a suitable short pass filter, since the highest energy photons have a large probability for reabsorption and are less likely to escape the sample after being reflected at the rear surface.[19] By placing a 1000 nm short pass filter (transmittance spectrum shown in Figure 5) in front of the camera in the PL imaging setup, the signal enhancement was reduced to ~7% for the samples used in this paper. This number can be further reduced by using filters with a lower wavelength cut-off, at the cost of reduced signal strength.

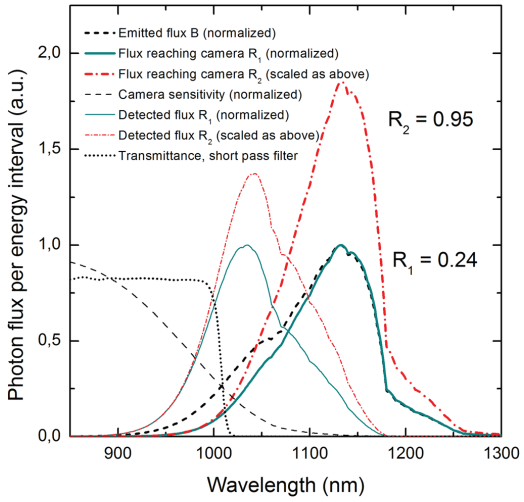

FIG. 5. Photon flux per energy interval as a function of wavelength, illustrating the effect of rear reflectance on the detected PL intensity. The black curve shows the theoretical band to band luminescence peak (Eq. (6)), while the solid red and cyan curves show the photon flux reaching the camera after being subject to reabsorption and reflection at the sample surfaces, for two different values of the rear reflectance (Eq. (7)). The dashed lines show the detected photon flux calculated from the camera sensitivity function. By applying a short pass filter, the effect of rear reflectance on the detected PL signal can be reduced.

B. Bulk and front surface recombination

The effective lifetime is related to the front and rear SRVs S_f and S_r and the bulk lifetime τ_{bulk} by the following set of equations:[20]

$$\tau_{eff} = \left(\frac{1}{\tau_{bulk}} + \alpha_0^2 D\right)^{-1}, \quad (8)$$

$$\tan(\alpha_0 W) = \frac{S_r + S_f}{\alpha_0 D - \frac{S_r S_f}{\alpha_0 D}}, \quad (9)$$

where D is the minority carrier diffusivity and α_0 is the smallest eigenvalue solution of Eq. (9). In order to calculate the rear side SRV from the measured lifetime data, Eqs. (8) and (9) were solved for S_r for each measured value of τ_{eff}. High quality FZ wafers with a high bulk lifetime were used to ensure that the contribution from bulk recombination is small. Still, there is a possibility for contamination of the bulk by in-diffusion of impurities during the high temperature oxidation step, degrading the bulk lifetime of the wafers. In order to determine the bulk lifetime of the FZ wafers after oxidation, a quarter of each wafer was dipped in a 5% HF solution for 1 min, cleaned by a standard RCA 1 + 2 clean, and passivated on both sides with a 40 nm thick PECVD a-Si:H layer. This passivation ensures a SRV less than 5 cm/s, which implies that the measured effective lifetime of these samples gives a good indication of the bulk lifetime. Based on these measurements, a constant bulk lifetime of 5 ms was chosen for both the n-type and p-type samples in the calculations. The errors in the rear side SRV was calculated using a minimum bulk lifetime of $\tau_{bulk} = 2.1$ ms and maximum bulk lifetime limited entirely by intrinsic recombination.[21]

By using symmetrically passivated wafers, the front side SRV S_f can be calculated from Eqs. (8) and (9) using the effective lifetime in a reference region which is not influenced by the metal electrodes. Another alternative, which was used in Ref. 7, is to use a known passivation layer with a low SRV on the front of the wafer, so that τ_{eff} is dominated by recombination on the rear side. We estimate the uncertainty in the determination of S_f to be 10%.

C. Effect of lateral charge carrier transport

In a PL imaging measurement, the intensity at each point is determined both by recombination in that region and diffusion of charge carriers into and out of regions that are a few diffusion lengths away. In a lifetime measurement performed by calibrated PL imaging, this can be observed as a blurring of the image on samples with high lifetimes. For the

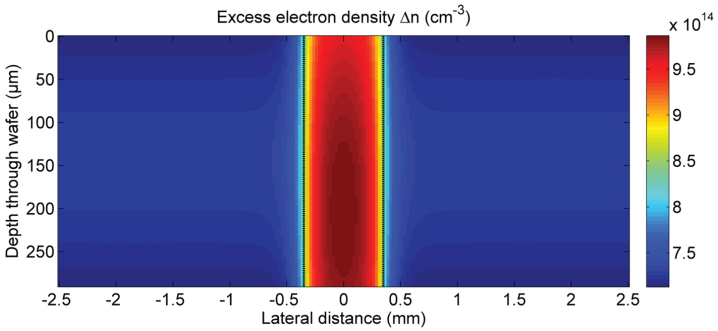

FIG. 6. Calculated excess electron density as a function of lateral distance x and depth z. The simulation was performed for a p-type Si wafer with $S_1 = 35$ cm/s and $S_2 = 15$ cm/s. The edges of the gate electrode are marked with black lines. Note the difference in scaling in the x- and z-directions.

PL-V measurements, this blurring effect can be clearly observed at the edges of the region affected by the external voltage, as carriers diffuse into or out of the region when the effective lifetime is lower or higher than the surrounding areas, respectively. In order to obtain a correct lifetime value, the metal electrode should ideally be sufficiently large so that the measured carrier concentration (and thus the effective carrier lifetime) over the central part of the electrode is unaffected by the lateral diffusion process at the edges. The electrodes can, however, normally not be made arbitrarily large, as the probability of leakage current through pinholes or other non-uniformities in the film increases with the electrode area. Another advantage of a small electrode area is that multiple PL-V curves can be (simultaneously) measured on the same sample, allowing for improved measurement statistics and/or investigation of lateral variations in the surface properties.

In order to quantitatively investigate the magnitude of the error arising from lateral carrier diffusion during the PL-V measurement, we have simulated the carrier density profile in a cross section of the wafer with two different fixed values for the effective SRV on the rear side, using the same geometry as shown in Figure 5. The simulation model of the sample was simplified to two dimensions by assuming a stripe electrode instead of the square electrodes that was used for the experiments. The generation rate G was calculated assuming a constant flux of $7.12 \times 10^{16}\,\mathrm{cm}^{-3}\,\mathrm{s}^{-1}$ uniformly distributed in x−direction and a photon wavelength of 808 nm. The spatial carrier density profiles were then simulated from the 2D continuity equation, describing a plane (x,z) normal to the direction of the stripe electrode

$$G(x,z) + D\nabla^2\Delta n(x,z) - \frac{\Delta n(x,z)}{\tau_{bulk}} = 0. \qquad (10)$$

Surface recombination was accounted for by defining boundary conditions around the simulated region given by

$$\frac{d\Delta n}{dz} = -\frac{S}{D} \quad (\text{top and bottom}),$$
$$\frac{d\Delta n}{dx} = 0 \quad (\text{sides}). \qquad (11)$$

Two different SRV values named S_1 and S_2 were used on the rear side as illustrated in Figure 4. The front side SRV was set equal to the rear SRV of the reference region S_1. The differential equation and boundary conditions described by Eqs. (10) and (11) were solved numerically using the partial differential equation solver FlexPDE 6.[22] An example of the simulated excess carrier density profile for a p-type wafer is shown in Figure 6.

Figure 7 shows the simulated effective lifetime as a function of lateral distance (calculated from the average Δn in the z-direction) for three different gate voltages, along with corresponding linescans taken from the calibrated PL images of the n-type sample. The experimental lifetime data is not corrected for the optical effects described above. Instead, the simulated curves are multiplied with an optical enhancement factor of 1.36 in the region over the rear electrode to account for the optical effects of the electrode in the measurement. The simulated curves correspond well with the experimental curves. The main difference is a slightly broader diffusion profile for the experimental curve as compared to that for the simulated curve. This may be caused by the fact that the simulation only takes diffusion in one dimension into account,

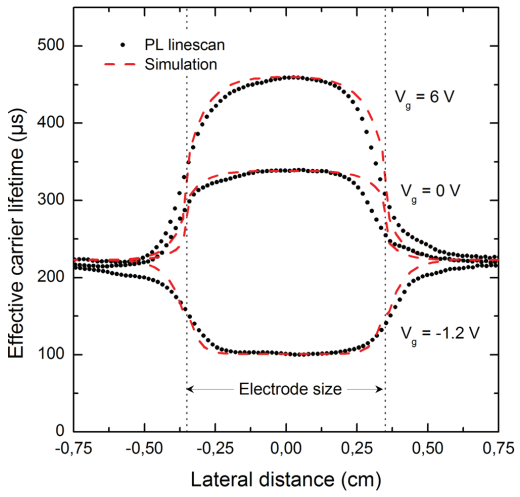

FIG. 7. Effective carrier lifetime as a function of lateral distance over a PL-V electrode for three different gate voltages. Linescans from PL images (black symbols) are shown along with simulated curves (dashed lines) obtained by solving Eqs. (10) and (11), with $S_1 = 67.0$ cm/s and $S_2 = 8.8$, 37.2, and 373.6 cm/s for the top, middle, and bottom curves, respectively.

whereas the experimental curves are affected by diffusion of carriers in both the x- and y-directions.

The simulated curves can be used to investigate general aspects of the effect of lateral diffusion on the measurements and the possible errors that arise for insufficient electrode sizes. One example of such an analysis is given in Figure 8, which shows the apparent (non-corrected) SRV for a p-type sample, calculated from the effective lifetime in the measurement region, as a function of the actual SRV in this region, for different electrode sizes. For an electrode width larger than 7 mm, the deviation in the SRV is less than 20% for actual SRVs in the range between ~8 cm/s and ~6000 cm/s, and the main deviation can be seen at low SRVs. This is consistent with the linescans shown in Figure 7, which shows that the scan profile in the center of the electrode region is flatter (indicating less influence of diffusion) for high SRVs compared to that observed for low SRVs.

D. Leakage current through the oxide layer

Both when using gate electrodes and surface corona charges, it is important to avoid significant leakage current through the passivation layer. For corona charges, leakage currents directly affect the charge stability. A Kelvin probe can be used to measure the actual surface charge before measurements, but a significant leakage current will result in uncertainties in the charge quantification. When using a gate electrode, a leakage current will not affect the stability of the surface potential, but may still influence the measurements. Charge injection into the Si wafer may result in an overestimation of the measured effective lifetime, but this effect is normally insignificant and may be neglected except in the case for large leakage currents (several mA) and very low injection conditions. A more significant effect might be a lowering of the surface potential during measurements, resulting in an overestimation of the SRV. No significant leakage current ($<1\,\mu$A) was measured during the PL-V measurements presented in this paper.

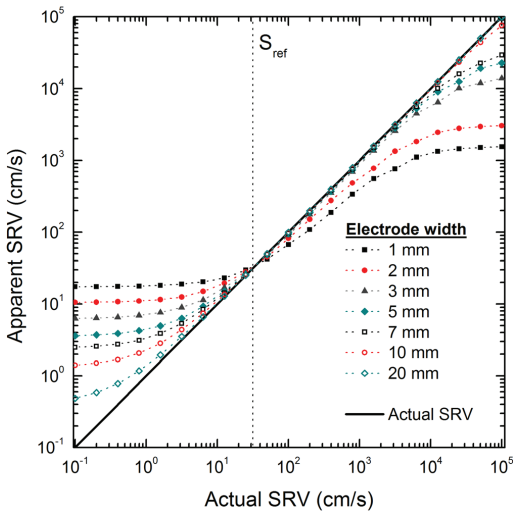

FIG. 8. Simulated apparent SRV for a p-type sample as calculated from the effective lifetime in the center of the measurement region as a function of the actual SRV in this region for different electrode sizes. The dashed line indicates the SRV of the surrounding area S_{ref}. These curves are used to estimate the error in the measured SRV arising from lateral diffusion of charge carriers into and out of the measurement region.

V. SIMULATION OF THE EFFECTIVE SRV VS. VOLTAGE

A. The extended SRH recombination model

Measurements of effective lifetime (and thus the SRV) with varying surface potential allow for a fundamental understanding of the surface recombination mechanisms, and are particularly useful for separating the contributions from field-effect and chemical passivation. In order to quantitatively extract fundamental properties of the interface traps responsible for carrier recombination, we have fitted the results to an extended SRH recombination model.[23] The effective SRV at the SiO_2/c-Si interface is then calculated by integrating the SRH defect recombination over the energy-dependent continuum of interface states $D_{it}(E)$.[24,25] The SRV is strongly dependent on the surface concentration of electrons and holes n_s and p_s, which are determined by the doping concentration, the injection level, and the surface potential ψ_s. In order to simulate the effective SRV as a function of applied gate voltage, we have used the Girisch formalism[3,23] to determine a self-consistent value of ψ_s for any given combination of ϕ_{ms}, Q_{ox}, and V_g. This is the same approach which was used to compare the effect of deposited corona charge and applied gate voltage in Sec. III B. To simplify the analysis, we have assumed that Q_{ox} is constant with all the charges located at the SiO_2/c-Si interface and that the contribution from the charges in the interface traps Q_{it} can be neglected in the charge balance.

For the simulations, we assumed a constant distribution of interface states and constant capture cross sections over the band gap. Experimental D_{it} values measured in the middle of the band gap by the CPD method described in Ref. 14 were used as input to the model.

B. Additional surface recombination mechanisms

The measured effective SRV for an oxidized Si surface can generally not be enforced arbitrarily low by increasing the corona charge density or gate voltage. For a very high surface potential, the SRV can be dominated by a process which is different from the standard SRH recombination at the surface defects. Glunz *et al.*[6] attributed this to a combination of spatial fluctuation of the surface potential caused by inhomogeneous corona charge distribution at the surface, recombination at defects in the space-charge region, and shunt (tunnelling) currents of charge carriers through the potential barrier at the surface. For the polished wafers with deposited gate electrodes used in this work, we do not expect the spatial fluctuations of the surface potential to be an issue. Furthermore, we observe a similar minimum SRV for the accumulated surface as compared to the inverted surface. This indicates that no significant recombination occurs in the

space charge region, as the highest recombination rate is expected at the cross-over point where the electron and hole concentrations are of similar magnitude, which only is the case for the inverted surface. For the simulation in this model, we have therefore only considered the contribution from tunnelling shunt currents. The additional SRV contribution from this mechanism is given by[6]

$$S_{Rp} = \frac{V_{bulk}/R_p}{qc_0(e^{qV_{bulk}/k_BT} - 1)}, \quad (12)$$

where R_p is the resistance of an effective shunt conductor in parallel with the standard recombination current, $V_{bulk} = \phi_p - \phi_n$ is the separation of the quasi-Fermi levels in the bulk, and c_0 is the equilibrium minority carrier concentration. The total effective SRV was modelled as $S_{eff} = S_{SRH} + S_{Rp}$, where S_{SRH} is the SRV originating from the standard SRH surface recombination described above.

C. Simulation results

Figure 9 shows the effective front and rear SRV for the n-type sample as a function of applied voltage. The experimental data points are calculated from the PL-V curves shown in Figure 3 using Eqs. (8) and (9), and the error bars indicate the uncertainty calculated from the sum of the different possible errors discussed in Sec. IV. A Nelder-Mead optimization algorithm available through the Matlab Optimization Toolbox (Ref. 26) was used to find a best fit of the model described above to the experimental front and rear SRV data, using Q_{ox}, σ_n, σ_p, and R_p as free fitting parameters. The solid red lines show the best fit curves, and the dashed and dotted lines show the contributions from the standard SRH model and the shunt current recombination, respectively. The same procedure was carried out for the p-type sample (data not shown). The corresponding calculated lifetime curves for both samples are shown as solid red lines in Figure 3. For both the n-type and p-type samples, we find a good agreement between the simulated curves and the experimental data, except in a small region close to the flat band voltage, where the SRV goes through a maximum. In this region, the model overestimates the SRV with more than one order of magnitude for both samples, indicating that the extended SRH cannot be used to describe the surface recombination process correctly when the field effect passivation is completely removed.

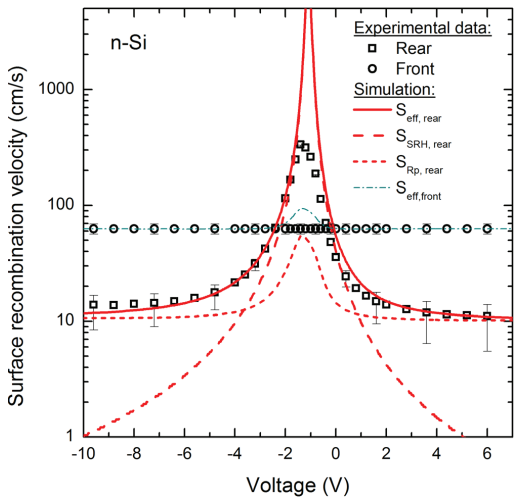

FIG. 9. Front and rear side SRV for the n-type sample as a function of applied voltage. Experimental values calculated from the PL-V data shown in Figure 3(b) are shown together with the different simulated contributions to the effective SRV described in Secs. V A and V B. Error bars were calculated as a sum of the different uncertainties discussed in Sec. IV.

The measured D_{it} values and the best fit simulation parameters for the two samples are shown in Table I, together with experimental values for the oxide charge density measured with both the CPD method and C-V measurements. The Q_{ox} values which give the best fit to the experimental SRV vs. voltage curves are in good agreement with the measured values from the CPD and C-V measurements. From the best-fit values, we find that the σ_n is in the same order of magnitude as σ_p for both samples, with the capture cross section ratio σ_n/σ_p being 5.4 and 2.2 for the p-type and n-type samples, respectively.

VI. CONCLUSION

We have demonstrated that the recently developed PL-V method can be used to analyze the recombination activity at the SiO_2/c-Si interface under varying band bending conditions. The measured effective carrier lifetime vs. voltage curves were found to be in excellent agreement with those obtained by QSS-μPCD measurements after deposition of controlled amounts of corona charges on the sample surface. We have discussed the impact of various different error contributions with regards to determination of the rear side SRV from the measured PL intensity, and the corrections presented in this paper are a first necessary step towards a quantitative analysis of more complex sample geometries and full solar cell structures. The imaging capability and direct measurement of the potential gives an additional advantage for the PL-V method in the quantification of these errors as compared to other techniques involving local modulation of the surface potential. We have shown how the measured SRV under varying applied gate voltage can be interpreted in the framework of the extended SRH theory, in terms of the interface state density and capture cross sections of the surface defects and the fixed oxide charge density. We find a good agreement between these results and complementary measurements of the oxide charge. In addition to the standard SRH recombination, an added contribution to the effective SRV, modeled as a tunneling shunt current through the surface space charge layer, was necessary to explain the experimental findings. The PL-V method allows for very fast measurements to be carried out independently of the measurement history of the sample and allows for simultaneous measurements of several areas of the wafer. Through this work, we have demonstrated the method as a powerful tool for fundamental investigation of c-Si passivation layers.

ACKNOWLEDGMENTS

This work has been funded by the Research Council of Norway through the project "Thin and highly efficient silicon-based solar cells incorporating nanostructures," NFR Project No. 181884/S1. The authors want to thank Dr. Augustinas Galeckas at the University of Oslo for valuable input on the spectroscopic aspects of the PL measurements.

[1]D. Biro, S. Mack, A. Wolf, A. Lemke, U. Belledin, D. Erath, B. Holzinger, E. A. Wotke, M. Hofmann, L. Gautero, S. Nold, J. Rentsch, and R. Preu, in *Proceedings of the 34th IEEE Photovoltaic Specialists Conference, Philadelphia, PA* (IEEE, 2009), p. 1594.
[2]A. G. Aberle, *Crystalline Silicon Solar Cells—Advanced Surface Passivation and Analysis* (Centre for Photovoltaic engineering, University of New South Wales, 1999), p. 118.
[3]R. B. M. Girisch, R. P. Mertens, and R. F. De Keersmaecker, IEEE Trans. Electron Devices **35**, 203 (1988).
[4]E. Yablonovitch, R. M. Swanson, W. D. Eades, and B. R. Weinberger, Appl. Phys. Lett. **48**, 245 (1986).
[5]M. Schofthaler, R. Brendel, G. Langguth, and J. H. Werner, in *Proceedings of the 1st World Conference on Photovoltaic Energy Conversion, Waikoloa, HI* (IEEE, 1994), p. 1509.
[6]S. W. Glunz, D. Biro, S. Rein, and W. Warta, J. Appl. Phys. **86**, 683 (1999).
[7]H. Haug, Ø. Nordseth, E. V. Monakhov, and E. S. Marstein, Sol. Energy Mater. Sol. Cells **106**, 60 (2012).
[8]T. Trupke, R. A. Bardos, M. C. Schubert, and W. Warta, Appl. Phys. Lett. **89**, 044107 (2006).
[9]M. Wilson, J. D'Amico, A. Savtchouk, P. Edelman, A. Findlay, L. Jastrzebski, J. Lagowski, K. Kis-Szabo, F. Korsos, A. Toth, A. Pap, R. Kopecek, and K. Peter, in *37th IEEE Photovoltaic Specialists Conference, Seattle, USA* (IEEE, 2011), pp. 1748–1753.
[10]W. Kern, J. Electrochem. Soc. **137**, 1887 (1990).
[11]R. A. Sinton, A. Cuevas, and M. Stuckings, in *Proceedings of the 25th IEEE Photovoltaic Specialists Conference, Washington, D.C., USA* (IEEE, New York, 1996), p. 457.
[12]J. Schmidt, IEEE Trans. Electron Devices **46**, 2018 (1999).
[13]M. Wilson, P. Edelman, J. Lagowski, S. Olibet, and V. Mihailetchi, Sol. Energy Mater. Sol. Cells **106**, 66 (2012).
[14]M. Wilson, J. Lagowski, A. Savtchouk, L. Jastrzebski, and J. D'Amico, in *ASTM Conference on Gate Dielectric Oxide Integrity, San Jose, CA, USA, 1999*.
[15]E. Nicollian and J. R. Brews, *MOS (Metal Oxide Semiconductor) Physics and Technology* (John Wiley & Sons, Inc., 2003), p. 423.
[16]A. G. Aberle, S. W. Glunz, A. W. Stephens, and M. A. Green, Prog. Photovoltaics **2**, 265 (1994).
[17]P. Wurfel, J. Phys. C **15**, 3967 (1982).
[18]T. Trupke, M. A. Green, P. Wurfel, P. P. Altermatt, A. Wang, J. Zhao, and R. Corkish, J. Appl. Phys. **94**, 4930 (2003).
[19]J. Müller, K. Bothe, S. Herlufsen, H. Hannebauer, R. Ferré, and R. Brendel, Sol. Energy Mater. Sol. Cells **106**, 76 (2012).
[20]A. B. Sproul, J. Appl. Phys. **76**, 2851 (1994).
[21]M. J. Kerr and A. Cuevas, J. Appl. Phys. **91**, 2473 (2002).
[22]*FlexPDE 6 User* Manual, PDE solutions Inc., 2011, see www.pdesolutions.com.
[23]A. G. Aberle, S. Glunz, and W. Warta, J. Appl. Phys. **71**, 4422 (1992).
[24]W. Shockley and W. T. Read, Jr., Phys. Rev. **87**, 835 (1952).
[25]D. J. Fitzgerald and A. S. Grove, IEEE Trans. Electron. Devices **15**, 426 (1968).
[26]*Optimization Toolbox User's Guide*, Mathworks, 2009, see www.mathworks.se/help/optim/.

III

Investigation of carrier recombination at the SiO_2/c-Si interface by photoluminescence imaging under applied bias

Halvard Haug, Ørnulf Nordseth, Edouard Monakhov and Erik Stensrud Marstein

***Abstract*—A new technique for analyzing the surface recombination for passivated silicon substrates has been employed to study the SiO_2/c-Si interface under various band bending conditions. A photoluminescence imaging setup was used to measure the effective minority carrier lifetime of oxidized Si wafers while applying an external bias over the rear side passivation layer. This method was used to investigate both the effect of substrate doping polarity and post-oxidation forming gas anneal (FGA) upon the surface passivation properties. The measured carrier lifetimes as a function of voltage were interpreted in the framework of the extended Shockley-Read-Hall theory. The calculated oxide charge density was found to decrease from ~7×10^{11} cm^{-2} to ~4×10^{11} cm^{-2} after the FGA treatment for both p-type and n-type substrates, causing a reduction in the field effect passivation. On the contrary, an increased chemical passivation was observed after FGA, shown by a reduction of the effective surface recombination velocity parameters by a factor of 3.8-5.5. In total, a significant increase in the effective carrier lifetime was obtained for both substrate types. Furthermore, the carrier capture efficiency at the surface defects was found to be 2-2.5 times higher for electrons than for holes, regardless of doping polarity and FGA.**

***Index Terms*—Charge carrier lifetime, imaging, photoluminescence, silicon, surfaces**

I. Introduction

In the development of high efficiency solar cells based on thin silicon wafers, reduction of electronic recombination at the wafer surfaces is a topic of high and increasing importance. The surface recombination velocity (SRV) at a silicon surface is proportional to the interface defect density and is limited by the availability of minority charge carriers near the surface. The recombination losses can therefore be reduced by lowering the interface defect density (chemical passivation) or by reducing the concentration of either electrons or holes in the region near the surface with a built-in electric field (field-effect passivation) [1]. Such band bending towards the surface is normally obtained in solar cells by applying a dielectric passivation layer incorporating fixed charges.

The SRV of a passivated Si surface is normally calculated from measurements of the effective minority charge carrier lifetime τ_{eff} (hereafter: lifetime), which contains contributions from recombination in the bulk of the wafer and at the two surfaces [2]. For characterization purposes, modulation of the surface band bending, and thus the SRV, is possible by applying voltage to a gate electrode placed on top of a dielectric passivation layer [3],[4],[5] or by deposition of charged ions on the surface in a corona discharge chamber [6],[7]. The latter method has traditionally been preferred in solar cell research, both because of its non-invasive nature and in order to avoid the necessity for making contacts to the sample. Additionally, the presence of metallic electrodes typically interferes with most of the common carrier lifetime measurements.

Recently we proposed a new technique for analyzing the surface recombination for passivated silicon substrates [8]. The technique is based on measurements of the effective lifetime in a photoluminescence (PL) imaging setup [9] while applying a voltage over the rear side passivation layer (PL-V). In contrast to corona charging techniques, PL imaging under applied bias requires the presence of metal electrodes on the sample surface. However, the method allows for very fast measurements and simultaneous data collection from multiple areas on the sample. The technique also has the advantage of allowing for repeated voltage sweeps between inversion and accumulation, which can be recorded with little or no influence of the measurement history of the sample.

Thermal oxidation is a well-established technology for surface passivation of Si substrates and can be implemented in both lab-scale and industrial solar cell processes [10]. The passivation properties of the c-Si/SiO_2 interface mainly arise from a high degree of chemical passivation, with a reported density of interface states D_{it} as low as 10^9 $cm^{-2}eV^{-1}$ [11]. Thermal SiO_2 layers may also give a moderate field-effect passivation, caused by positive fixed charges located at the interface, with a typical density in the range $1-5\times10^{11}$ cm^{-3} [12]. In this paper we have used measurements of effective lifetime as a function of voltage (PL-V) to investigate the surface passivation properties of SiO_2 layers formed by high temperature dry oxidation. Furthermore, we present an interpretation of the surface passivation properties

This work has been funded by the Research Council of Norway through the project "Thin and highly efficient silicon-based solar cells incorporating nanostructures," NFR Project No. 181884/S1.

H. Haug, Ø. Nordseth and E. S. Marstein are with the Department of Solar Energy, Institute for Energy Technology, Kjeller 2027, Norway, (e-mail: halvard.haug@ife.no; ornulf.nordseth@ife.no; erik.stensrud.marstein@ife.no).

H. Haug, E. Monakhov and E. S. Marstein are with the Department of Physics, University of Oslo, Blindern, Oslo 0316, Norway

in terms of the oxide charge density and the effective surface recombination parameters for electrons and holes.

II. Experimental Details

Samples were made from double side polished and thermally oxidized FZ Si (100) wafers. Both n-type (P-doped) and p-type (B-doped) substrates were used, with doping concentrations of 1.7×10^{15} and 5.0×10^{15} cm^{-3}, and thicknesses of 290 and 280 µm, respectively. The wafers had a high bulk lifetime to ensure that the measured effective lifetime was dominated by recombination at the wafer surfaces.

After a standard RCA (1+2) clean and 30 s immersion in a 5% HF solution, the wafers were loaded into a tube furnace and oxidized in dry O_2 at 1000 °C for 60 min. The resulting thermal SiO_2 layers provide a stable, high quality surface passivation with negligible leakage current, simplifying the interpretation of the results. Subsequently, one wafer of each doping polarity received a post-oxidation forming gas anneal (FGA) with 5% H_2 in N_2 at 400 °C for 30 min. This process is commonly used in the literature to reduce the number of interface states by hydrogen diffusion and passivation of dangling bonds [1]. The oxide thickness was measured by variable-angle spectroscopic ellipsometry and found to be 66-68 nm uniformly across the wafers.

7 mm × 7 mm square electrodes for PL-V measurements and 0.45-2.25 mm diameter circular electrodes for capacitance vs. voltage (C-V) measurements were deposited onto the oxide layers by thermal evaporation of Al through a shadow mask. Finally, low resistivity contacts were made to the Si substrate by grinding down the oxide with P200 sand paper and depositing Ag by thermal evaporation in the region opposite the C-V electrodes.

A schematic overview of the experimental setup for the PL-V method is shown in Fig. 1. Steady state carrier lifetime measurements were carried out with a LIS-R1 PL imaging setup from BT imaging with an excitation wavelength of 808 nm and a constant illumination intensity of 33.4 mW/cm^2. In a PL imaging lifetime measurement, the excess minority carrier concentration (injection level) at each point of the image is calculated from the measured PL intensity. For a p-type sample Δn is given by

$$\Delta n = \sqrt{\left(\frac{N_A}{2}\right)^2 + \frac{I_{PL}}{C_{cal}}} - \frac{N_A}{2}, \qquad (1)$$

where N_A is the acceptor doping concentration, I_{PL} is the measured PL intensity and C_{cal} is an instrument- and sample specific calibration constant, which is determined from a quasi-steady state photoconductance (QSSPC) measurement [13]. For the PL-V measurements, a reference region without metal electrodes was used for this purpose. An external voltage source was connected to the sample as shown in Fig. 1 in order to perform the measurements with an applied bias over the rear side passivating oxide layer. The PL intensity in the region over the Al electrodes is enhanced compared to the reference region due to an increased rear side reflectance, ausing a larger fraction of the emitted PL light to reach the camera. To account for this, I_{PL} in the region above the metal electrodes was divided by an optical enhancement factor of 1.36. This factor is sample specific and was determined experimentally by measuring the enhancement of the PL intensity after placing the sample over an Al mirror made by thermal evaporation of 100 nm Al on a glass substrate. The steady state effective lifetime image was then calculated from the measured injection level averaged over the electrode area as $\tau_{eff} = \Delta n/G$, where G is the excess carrier generation rate per volume. An extensive discussion of the optical corrections and other possible errors in the calculation of τ_{eff} is described elsewhere [14]. A typical PL lifetime image measured while applying voltage over the rear side passivation layer is shown in Fig. 2.

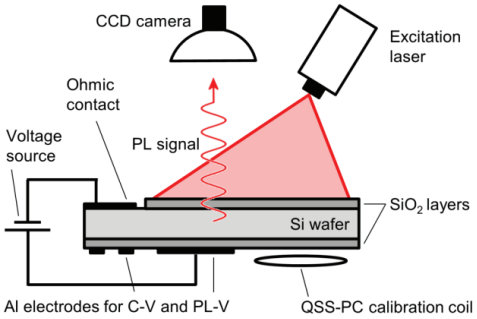

Fig. 1. Schematic overview of the experimental setup for the PL-V method, used to obtain lifetime images while modulating the surface band bending by applying voltage over the rear side passivation layer. Al electrodes for both C-V and PL-V measurements are present on each sample.

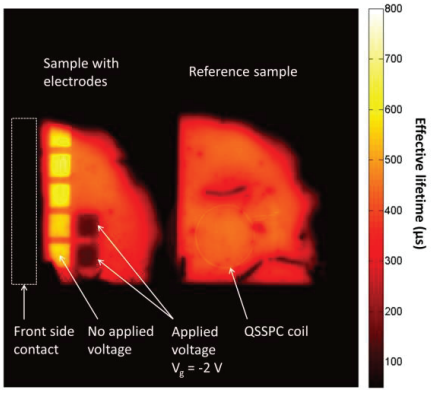

Fig. 2. PL lifetime image measured on the p-type wafer after FGA treatment while applying a voltage of -2 V over two of the rear Al electrodes. In this case a quarter of the wafer (right) is used for lifetime calibration, whereas Al electrodes are deposited on another quarter (left). Note that the PL signal is larger above the Al electrodes not under bias compared to the surrounding areas, due to the built-in voltage from the Al-Si work function difference and an increased rear reflectance. The C-V electrodes are hidden behind the front side contact covering the left hand side of the left quarter (see Fig. 1).

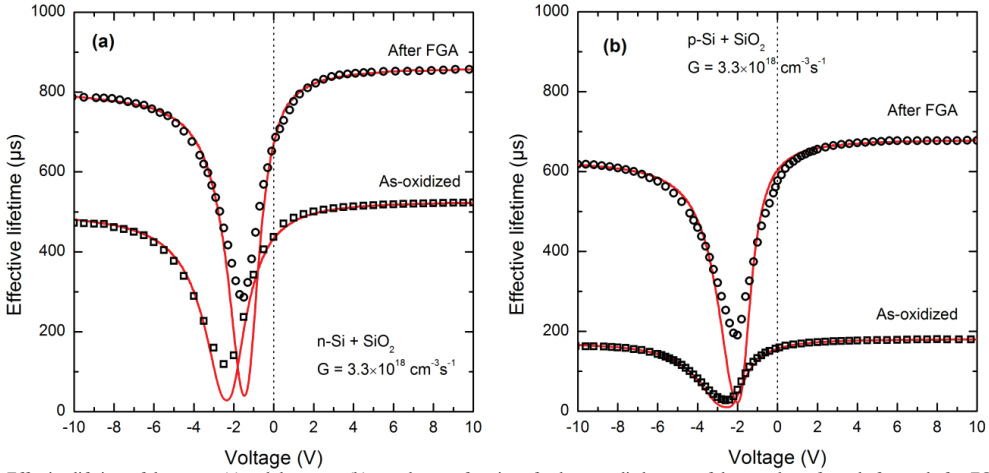

Fig. 3. Effective lifetime of the n-type (a) and the p-type (b) samples as a function of voltage applied to one of the sample surfaces, before and after FGA. The measurements were performed using a constant generation rate of G = 3.3×10^{18} $cm^{-3}s^{-1}$. The experimental data is shown as open symbols, whereas the simulated curves are shown as solid red lines. The simulation details are given in section IV-B and the simulation parameters are given in Table I. The line corresponding to zero applied voltage is indicated by a dotted vertical line for clarity.

The fixed oxide charge density Q_{ox} in the SiO_2 layers was extracted from high frequency (1 MHz) C-V curves measured using a Keithley 4200-SCS semiconductor characterization system. The fixed charge density per cm^2 is calculated as

$$Q_{ox} = C_{ox}(\phi_{ms} - V_{fb})/q, \qquad (2)$$

where C_{ox} is the measured oxide capacitance per unit area, q is the elementary charge, ϕ_{ms} is the metal-semiconductor work function and V_{fb} is the flat band voltage. V_{fb} is the voltage that is needed to obtain zero band bending at the Si surface, and can be extracted from the C-V curve following the procedure described in [15]. For a p-type sample ϕ_{ms} is calculated as

$$\phi_{ms} = F_m - \chi_{Si} - \frac{E_g}{2} - \frac{k_B T}{q}\ln\left(\frac{N_A}{n_i}\right), \qquad (3)$$

where F_m is the metal work function, χ_{Si} is the electron affinity of Si, E_g is the band gap, k_B is the Boltzmann constant, T is the temperature and n_i is the intrinsic carrier concentration. Using an Al work function of 4.1 eV and $\chi_{Si} = 4.05$ eV, ϕ_{ms} was calculated to be -0.84 eV for the p-type samples and -0.2 eV for the n-type samples. Results from between 10 and 15 measurements using different electrode sizes were averaged in the calculation of Q_{ox}.

III. Results

A. Effective lifetime vs. voltage

Fig. 3 shows the effective carrier lifetime of the n-type and p-type samples as a function of the applied gate voltage V_g. For both types of substrate doping the effective lifetime increases after FGA. All the carrier lifetime vs. voltage curves show the same general behavior: When a small negative voltage is applied the effective lifetime decreases as the external bias compensates the effect of the positive oxide charge density. For increasing negative voltages, the lifetime drops to a minimum corresponding to depletion conditions at the surface, before it increases as the surface is driven into inversion (n-type samples) or accumulation (p-type samples). The curves are slightly asymmetric, with a lower effective lifetime for large negative voltage as compared to large positive voltage.

The minimum lifetime in the PL-V curve in the as-oxidized state and after FGA is found to be 119 μs and 286 μs for the n-type sample and 27 μs and 190 μs for the p-type sample, respectively. The highest lifetime was observed in the n-type sample under accumulation conditions; with $\tau_{eff} = 856$ μs. Note that all lifetime images were measured using a constant generation rate, so that the injection level Δn changes with the lifetime in the sample according to the relation $\Delta n = \tau_{eff} G$. For instance, in the n-type sample after FGA the lifetime variation corresponds to injection levels in the range between 9.4×10^{14} cm^{-3} and 2.8×10^{15} cm^{-3}.

B. Capacitance-voltage measurements

Typical C-V curves measured on the p-type sample are shown in Fig. 4. The flat band voltage was observed to decrease after forming gas anneal, indicating a lowering of the oxide charge density. Average Q_{ox} values, calculated from 10-15 measurements on each sample, are presented in Table I.

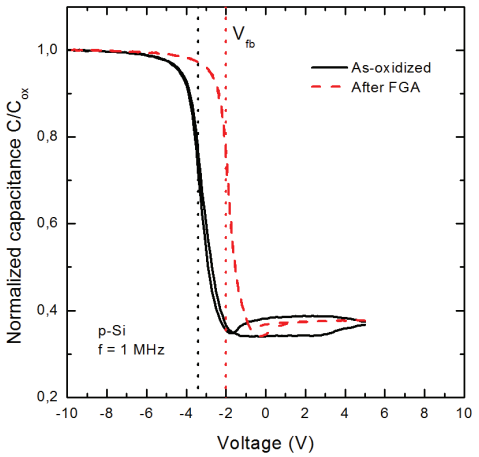

Fig. 4. Normalized C-V curves measured on the p-type sample, before (solid line) and after (dashed line) FGA treatment. The flat band voltage V_{fb} (indicated by dotted lines) is reduced after FGA treatment.

IV. Analysis and Discussion

A. Calculation of experimental SRV values

In order to obtain a more fundamental understanding of the data presented in Fig. 3, front and rear SRVs were calculated from the lifetime measurements in the following manner: The front side SRV S_f was first calculated from the effective lifetime τ_{eff} measured by QSSPC in the reference region, where the front and rear SRVs are assumed to be identical [2]:

$$S_f = \alpha D \tan\left(\frac{\alpha W}{2}\right). \quad (4)$$

Here D is the minority carrier diffusion coefficient, W is the wafer thickness and α is given by

$$\alpha = \sqrt{\frac{1}{D}\left(\frac{1}{\tau_{eff}} - \frac{1}{\tau_{bulk}}\right)}, \quad (5)$$

where τ_{bulk} is the bulk lifetime. It should be noted that the effective lifetime in the reference region does not directly correspond to the lifetime measured at 0 V in the PL-V curves, as the lifetime over the electrodes is also influenced by the change in rear SRV caused by the built-in potential due to ϕ_{ms}. The rear side SRV S_r was then calculated from S_f and the measured lifetime, over the active electrode at each point of the curves shown in Fig. 3 as [2]:

$$S_r = \frac{\tan(\alpha W)\,\alpha^2 D^2 - \alpha D S_f}{\alpha D + \tan(\alpha W)\,S_f}, \quad (6)$$

with α defined as above. FZ wafers with a high bulk lifetime were used in the experimental investigation to ensure that the contribution from bulk recombination is small. Still, the chosen value for τ_{bulk} has some influence on the result. To ensure that the bulk lifetime did not significantly degrade after oxidation a quarter of each wafer was dipped in a 5% HF solution for 1 min to strip off the oxide layers, cleaned by a standard RCA 1+2 clean, dipped in 5% HF solution for 30 s and passivated on both sides with a 40 nm thick layer of hydrogenated amorphous Si (a-Si:H) deposited by plasma enhanced chemical vapor deposition. This surface passivation layer ensures a SRV less than 5 cm/s, and thus the measured effective lifetime of these samples give a good indication of the bulk lifetime. Based on these measurements a constant bulk lifetime of 5 ms was chosen for the calculations, and the error bars on the SRV values were calculated using $\tau_{bulk} = 2.5$ ms and $\tau_{bulk} = \infty$ ms as minimum and maximum values. The calculated values for S_f and S_r as a function of V_g for the p-type sample after FGA treatment is shown in Fig. 5.

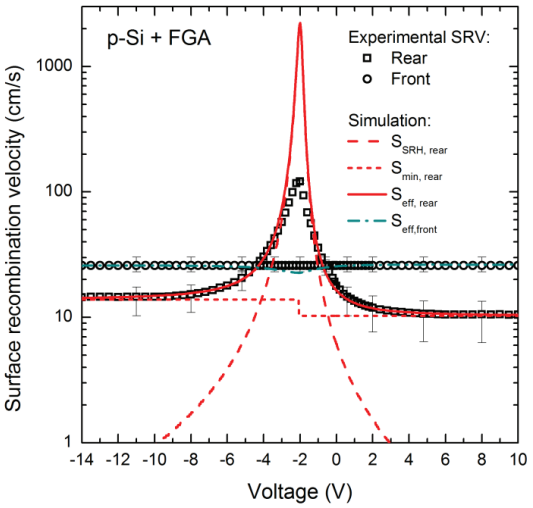

Fig. 5. Front and rear side SRV for the p-type sample after FGA as a function of applied voltage. Experimental values (calculated from the measured carrier lifetime data shown in Fig. 3) are plotted together with the different simulated contributions to the effective SRV. Error bars are calculated from minimum and maximum bulk lifetime values.

B. Simulation of the effective SRV

Measurements of effective lifetime (and thus the SRV) with varying surface potential allow for a fundamental understanding of the surface recombination mechanisms, and are particularly useful for separating the contributions from field-effect and chemical passivation. In order to quantitatively extract fundamental properties of the interface traps responsible for carrier recombination we have fitted the results to an extended Shockley-Read Hall (SRH) recombination model [16]. No measurements of the (energy dependent) interface state density D_{it} or capture cross sections $\sigma_{n/p}$ have been performed for this work. A simplified model including one effective midgap defect level was therefore

chosen, and was found to sufficiently describe the observations. The rear effective SRV is then given from standard SRH theory as

$$S_{SRH} = \frac{1}{\Delta n} \frac{S_{n0} S_{p0} (n_s p_s - n_i^2)}{S_{n0}(n_s + n_i) + S_{p0}(p_s + n_i)}, \quad (7)$$

where n_i is the intrinsic carrier concentration and S_{n0} and S_{p0} are the SRV parameters of electrons and holes, defined as the product of the electron thermal velocity v_{th}, the concentration of surface states per unit area N_{it} and the corresponding capture cross section σ_n or σ_p. The surface concentrations of electrons and holes n_s and p_s are strongly dependent on the surface potential ψ_s. We use the so-called Girisch formalism [3], [16] to numerically find a self-consistent value for ψ_s (and thus n_s and p_s) for any given values for V_g, Q_{ox} and ϕ_{ms}. This method is based upon a numerical solution of the charge balance at the interface, under the assumption of constant quasi Fermi levels throughout the surface space charge region. To simplify the analysis we have assumed that Q_{ox} is constant with all the charges located at the c-Si/SiO_2 interface and that the contribution from the charges in the interface traps Q_{it} can be neglected in the charge balance.

As seen on the experimental SRVs shown in Fig. 5, the SRV could not be enforced arbitrarily low by increasing the voltage, but instead it reaches a minimum value. It was therefore necessary to add a (voltage-independent) contribution to the effective SRV called S_{min} in order to correctly describe the flattening of the lifetime vs. voltage curves under large surface band bending:

$$S_{eff} = S_{SRH} + S_{min}. \quad (8)$$

Note that this effect could not be accounted for by recombination at the front surface or in the bulk of the wafers. A similar approach has also previously been used for such simulations [7],[12]. In these works inclusion of shunt and recombination currents through the space-charge region were used to theoretically describe measurements of the SRV as function of surface charge and injection level.

The measured minimum SRV was found to be different for large negative voltages compared to large positive voltages. S_{min} was therefore modeled as

$$S_{min} = \begin{cases} S_{min,n} \text{ for } \psi_s < 0 \\ S_{min,p} \text{ for } \psi_s > 0. \end{cases} \quad (9)$$

C. Simulation results

The model described above was used to numerically calculate the effective SRV for each value of V_g. A least squares optimization algorithm was then used find a best fit between the model and the front and rear experimental SRVs, with S_{0n}, S_{0p}, Q_{ox}, $S_{min,n}$ and $S_{min,p}$ used as free fitting parameters. When simultaneously fitting the model to both S_r and S_f it is possible to find a relatively unique fit, as each parameter plays a different role in the determination of the curve: S_{n0} and S_{p0} determine the slope of the left and right hand side of the SRV peak, Q_{ox} determines the position of the lifetime minimum along the voltage axis, and $S_{min,n}$ and $S_{min,p}$ determine the minimum SRV at large negative and large positive voltages, respectively. The simulated effective lifetime for each measurement is shown in Fig. 3 and the different SRV contributions are shown in Fig. 5 for the p-type sample after FGA. The best fit parameters for each measurement are given in Table I, together with the average Q_{ox} values calculated from C-V measurements.

From Table I it can be seen that both S_{n0} and S_{p0} are reduced after FGA for both substrate polarities. The ratio between the capture cross sections for electrons and holes σ_n / σ_p (given by S_{n0}/S_{p0}) are however found to approximately constant, and is found to be between 2 and 2.5 for all measurements, regardless of doping polarity and FGA treatment. Knowledge of this ratio is valuable as it can aid in an identification of the type of defect which is dominating the recombination. It is also interesting from a technological point of view, as the ratio between σ_n and σ_p affects the injection level dependence of the SRV, which again is a contributing factor to the fill factor of high-efficiency Si solar cells with passivated rear surfaces.

The minimum SRV values $S_{min,n}$ and $S_{min,p}$ are also observed to decrease after FGA, with $S_{min,n}$ being larger than $S_{min,p}$ for all the curves. This is consistent with σ_n being larger than σ_p at the interface defects.

Furthermore, Q_{ox} is found to decrease from $6 - 7 \times 10^{11}$ to $\sim 4 \times 10^{11}$ cm^{-3} after FGA for both samples, caused by a shift of the lifetime minimum towards lower negative voltages in the PL-V curves. This is in good agreement with the results from the C-V measurements, shown in the lower part of Table I. The observed reduction of both the oxide charge and the effective SRV parameters (and thus D_{it}) is consistent with previous findings in the literature [1, p. 118].

D. Possible errors and deviations

Using the best-fit parameters the model described in section IV-B gives a good simultaneous agreement with the measured front and rear SRVs under most band bending conditions. The SRH model however overestimates the rear SRV in the region of the curve corresponding to depletion conditions (close to V_{fb}) by more than one order of magnitude. In this region the applied voltage counteracts the field-effect passivation from the oxide charges, and the rear SRV goes through a maximum where it is limited by chemical passivation only. This discrepancy suggests that the model described in section IV-B cannot fully describe the surface recombination behavior when the SRV is large. A possible explanation for this may be that the assumption of constant quasi-Fermi levels throughout the surface space region which is used in [3] may not hold for the largest SRVs observed at depletion conditions.

The error bars indicated in Fig. 5 are calculated based on an uncertainty in the bulk lifetime of the samples. This possible

TABLE I
SIMULATION PARAMETERS AND Q_{ox} VALUES CALCULATED FROM THE C-V MEASUREMENTS.

	Parameter	Description	Unit	n-type sample		p-type sample	
				As-oxidized	FGA	As-oxidized	FGA
Fitting parameters for simulations	S_{n0}	SRV parameter for electrons	cm/s	12000	3300	21000	2500
	S_{p0}	SRV parameter for holes	cm/s	5700	1300	8800	990
	$S_{min,\,n}$	Minimum SRV, $\psi_s < 0$	cm/s	21	9.1	61	14
	$S_{min,\,p}$	Minimum SRV, $\psi_s > 0$	cm/s	17	6.6	53	10
	Q_{ox}	Fixed oxide charge	cm^{-2}	6.8×10^{11}	3.7×10^{11}	6.1×10^{11}	4.0×10^{11}
C-V analysis	Q_{ox}	Fixed oxide charge	cm^{-2}	7.3×10^{11}	2.7×10^{11}	6.9×10^{11}	3.5×10^{11}
		Standard deviation	cm^{-2}	0.3×10^{11}	0.5×10^{11}	0.4×10^{11}	0.2×10^{11}

error is however the same for all points along the curve, so the conclusions based on relative differences, e.g. the difference between $S_{min,n}$ and $S_{min,p}$, are still valid. No significant charge build-up was observed during the course of the measurement, meaning that the points along the voltage-lifetime curve could be almost perfectly reproduced when the measurements were repeated without moving the sample. This is consistent with a very small hysteresis in the C-V curves shown in Fig. 3, which implies that Q_{ox} is not changed during the measurement.

V. CONCLUDING REMARKS

The PL-V technique has been shown to give reproducible results which are in agreement with both capacitance-voltage measurements and previous findings in the literature. Analysis of the PL-V curves using an extended SRH model gives valuable information about the passivation mechanisms, and can be used to separate the contributions from field-effect and chemical passivation. The method may be used to determine S_{n0}, S_{p0} and Q_f for a wide range of dielectric passivation layers, and in combination with supplementary measurements of the interface state density D_{it} the method can also be used to determine the absolute values of σ_n and σ_p for the recombination active defects at the interface. The PL-V method allows for very fast measurements to be carried out independently of the measurement history of the sample, and gives the possibility of simultaneous measurements of several areas of the wafer. PL-V measurements can therefore be used as an attractive alternative method for characterization of Si surface passivation layers.

ACKNOWLEDGMENT

The authors wish to thank Tine Uberg Nærland for valuable input and discussion of the manuscript and Marie Syre Wiig for help with the thermal oxidation process and forming gas annealing of the wafers.

REFERENCES

[1] A. G. Aberle, "Crystalline silicon solar cells - Advanced surface passivation and analysis". Centre for Photovoltaic engineering, University of New South Wales, 1999.

[2] A. B. Sproul, "Dimensionless solution of the equation describing the effect of surface recombination on carrier decay in semiconductors," *J. Appl. Phys*, vol. 76, no. 5, pp. 2851–2854, 1994.

[3] R. B. M. Girisch, R. P. Mertens, and R. F. De Keersmaecker, "Determination of Si-SiO_2 interface recombination parameters using a gate-controlled point-junction diode under illumination," *IEEE Trans. Electron. Devices*, vol. 35, no. 2, pp. 203–222, 1988.

[4] E. Yablonovitch, R. M. Swanson, W. D. Eades, and B. R. Weinberger, "Electron-hole recombination at the Si-SiO_2 interface," *Appl. Phys. Lett.*, vol. 48, no. 3, pp. 245–247, 1986.

[5] W. E. Jellett and K. J. Weber, "Accurate measurement of extremely low surface recombination velocities on charged, oxidized silicon surfaces using a simple metal-oxide-semiconductor structure," *Appl. Phys. Lett.*, vol. 90, no. 4, pp. 042104–042104-3, 2007.

[6] M. Schofthaler, R. Brendel, G. Langguth, and J. H. Werner, "High-quality surface passivation by corona-charged oxides for semiconductor surface characterization," in *Proc. 1st World Conf. Photovoltaic Energy Convers.*,Waikoloa, HI 1994, vol. 2, pp. 1509-1512.

[7] S. W. Glunz, D. Biro, S. Rein, and W. Warta, "Field-effect passivation of the SiO_2 Si interface," *J. Appl. Phys*, vol. 86, no. 1, pp. 683-691, 1999.

[8] H. Haug, Ø. Nordseth, E. V. Monakhov, and E. S. Marstein, "Photoluminescence imaging under applied bias for characterization of Si surface passivation layers," *Sol. Energy Mater. Sol. Cells*, vol. 106, pp. 60–65, 2012.

[9] T. Trupke, R. A. Bardos, M. C. Schubert, and W. Warta, "Photoluminescence imaging of silicon wafers," *Appl. Phys. Lett.*, vol. 89, no. 4, pp. 44103–44107, 2006.

[10] D. Biro, S. Mack, A. Wolf, A. Lemke, U. Belledin, D. Erath, B. Holzinger, E. A. Wotke, M. Hofmann, L. Gautero, S. Nold, J. Rentsch, and R. Preu, "Thermal oxidation as a key technology for high efficiency screen printed industrial silicon solar cells," *Proc. 34th IEEE Photovoltaic Spec. Conf.*, Philadelphia, PA, 2009. pp. 1594–1599.

[11] A. G. Aberle, S. W. Glunz, A. W. Stephens, and M. A. Green, "High-eficiency silicon solar cells: Si/SiO_2 interface parameters and their impact on device performance," *Prog. Photovoltaic Res. Appl,*, vol. 2, no. 4, pp. 265–273, 1994.

[12] S. Mack, A. Wolf, C. Brosinsky, S. Schmeisser, A. Kimmerle, P. Saint-Cast, M. Hofmann, and D. Biro, "Silicon Surface Passivation by Thin Thermal Oxide/PECVD Layer Stack Systems,"*IEEE J. Photovoltaics*, vol. 1, no. 2. pp. 135–145, 2011.

[13] R. A. Sinton, A. Cuevas, and M. Stuckings, "Quasi-Steady-State PhotoConductance, A new method for solar cell material and device characterization," in *Proc. 25th IEEE Photovoltaic Spec. Conf.*, Washington, DC, 1996, pp. 457-460.

[14] H. Haug, S. Olibet, Ø. Nordseth, and E. S. Marstein, "Modulating the field-effect passivation at the SiO_2/c-Si interface: Analysis and verification of the photoluminescence imaging under applied bias method," *J. Appl. Phys,* to be published.

[15] D. K. Schroeder, "Semiconductor material and device characterization", 3rd ed. John Wiley & Sons, Inc., Hoboken, New Jersey., 2006, p. 334.

[16] A. G. Aberle, S. Glunz, and W. Warta, "Impact of illumination level and oxide parameters on Shockley--Read--Hall recombination at the $Si-SiO_2$ interface," *J. Appl. Phys*, vol. 71, no. 9, pp. 4422–4431, 1992.

IV

V

VI

Available online at www.sciencedirect.com

Energy Procedia 00 (2013) 000–000

Energy Procedia

www.elsevier.com/locate/procedia

SiliconPV: March 25-27, 2013, Hamelin, Germany

A graphical user interface for multivariable analysis of silicon solar cells using scripted PC1D simulations

Halvard Haug[a]*, Birger R. Olaisen[a,b], Ørnulf Nordseth[a], Erik S. Marstein[a,c]

[a]*Institute for Energy Technology, Instituttveien 18, 2007 Kjeller, Norway*
[b]*Norwegian Defence Research Establishment, Instituttveien 20, 2007 Kjeller, Norway*
[c]*Department of Physics, University of Oslo, 0316 Oslo, Norway*

Abstract

PC1D is an open source computer program for simulation of crystalline semiconductor devices, and is the most commonly used simulation software in the solar cell community today. In this work we present a modified version of PC1D which runs from a command line, thus allowing for scripted simulations using any programming language. In order to increase the accessibility of the new program, we have developed a free-for-use graphical user interface which can be run as a standalone executable. We demonstrate the potential of this program by presenting examples of different simulations. The new features that have been implemented in the new program include multivariable analysis, visualization of three-dimensional data sets, extraction of relevant parameters not directly available in PC1D, utilization of optimization algorithms, fitting to experimental data and implementation of additional features like contact shading, emitter series resistance and passivated rear surfaces with local contacts. Simulations can be performed in a simple and efficient manner, allowing for fast analysis and optimization of cell performance, as well as an enhanced fundamental understanding of the physics of solar cell devices.

Selection and/or peer-review under responsibility of the scientific committee of the SiliconPV 2013 conference

Keywords: Solar cells; simulation; software

1. Introduction

PC1D is one of the most commonly used modelling programs for simulation of crystalline semiconductor solar cells. The program uses a finite-element numerical method for solving the coupled nonlinear equations for carrier generation, recombination and transport in the device and can be used both

* Corresponding author. Tel.: +47 994 86 757.
E-mail address: halvard.haug@ife.no.

for simulation of device performance and as a tool for new users to understand the fundamentals of solar cell physics [1]. The main advantages of PC1D include high calculation speeds, an intuitive user interface and an extensive list of material and physical parameters. By varying the applied bias or the wavelength of the excitation light source, PC1D can calculate both current-voltage characteristics and spectral quantum efficiency of the solar cell, but it also has a large number of other options for output data, both in the spatial domain and in the time domain.

However, PC1D has some limitations in that it is somewhat cumbersome to do parameter variations, and additional calculations cannot be implemented directly by running it from within another program. The source code for the program is however freely available, allowing for user-defined modifications that have the potential to overcome these limitations. In this work we present a new version of the PC1D called *cmd-pc1d* which runs from a command line, thus allowing for scripted simulations using any programming language. In addition, we have also developed a free-for-use program which we have named *PC1D for Matlab*, which has many built-in possibilities for more advanced analysis, using the command line version of PC1D as the basis for the calculations. This program, which is written in Matlab, is modular and easy to use, giving the user the possibility of switching between the original PC1D interface and the new graphical user interface (GUI). The program is available free of charge and can either be run from Matlab or as a standalone executable.

2. Details of the simulation programs

2.1. The cmd-pc1d program

While PC1D is a great tool for users wanting to manually experiment with solar cell simulations, the original GUI makes it difficult to use for automated simulation or integration into other systems. The *cmd-pc1d* program was developed to allow access to all aspects of PC1D without having to launch the PC1D GUI. Since the PC1D source code has been made freely available, it has been possible to create a modified version of the program where all GUI code has been removed, and replaced with a simple command line interface called *cmd-pc1d.exe*. The program can be run in two different modes, (i) with a binary .prm parameter file, in which case the program runs the included simulation, or (ii) with both a .prm file and a batch file, which causes the program to run in batch mode. The simulation results are either written to a output file or directly to the command line window, which allows this version of PC1D to be scripted with common scripting tools like Matlab.

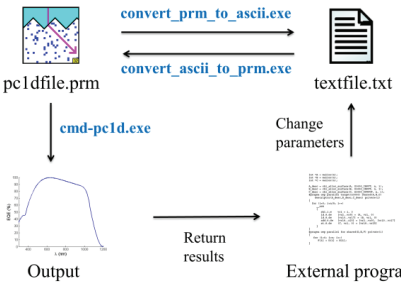

Fig.1. Schematic illustration of a typical workflow using the command-line version of PC1D and the two converter programs (marked in blue text).

In order to control *cmd-pc1d* from another program, the other program needs to create a binary .prm parameter file with specifications and commands that PC1D understands. This can be done with the original PC1D program, but in order to be flexible, two small tools (called *convert_prm_to_ascii.exe* and *convert_ascii_to_prm.exe*) were made to convert the PC1D .prm parameter files between binary format and text format. Fig. 1 shows a typical workflow when using *cmd-pc1d* from an external program. Starting with a base .prm file, which can be made using the original PC1D program, the file is converted to text format. Then individual parameters are modified, as required by the problem to be solved, and the file is converted back again to binary format. Next, *cmd-pc1d* is run with the modified .prm file, and the results are either saved in a text file or output directly into the calling program. Depending on the type of program, the results could be displayed to the user, or a different modification could be done to the parameter file used to run the next iteration.

2.2. The PC1D for Matlab program

Even though many types of calculations are possible with the *cmd-pc1d* program, it requires a high effort for users without knowledge of programming. In order to increase the accessibility of the program to a wider audience, we have created a graphical user interface using the Mathworks Matlab software [2], which in addition to setting up simulations using the *cmd-pc1d* program also implements many of Matlab's features for data analysis, visualization and optimization. The program can be run from Matlab, but has also been compiled as a standalone executable which does not require a Matlab license.

An image of the *PC1D for Matlab* user interface is shown in Fig. 2. A group of menu items and buttons for different actions like loading and saving .prm files, handling simulation results and changing plotting options are placed in the top part of the screen. The user can choose between five different tabs for access to various features of the program, including a complete list of input parameters, single and batch simulation setup, selection of output data, plotting options for batch results and options for importing and fitting simulations to experimental data. In the first tab a subset of the parameters used to define the PC1D prm-file is shown in a scrollable list with descriptive parameters names that can be defined in a separate text file. The user has the option to change to the original PC1D interface at any time. The figure window placed on the right part of screen can be used for plotting PC1D output data, data sets calculated from the output data (e.g. current density vs. applied voltage) or results from batch simulations (e.g. open circuit voltage as a function of bulk carrier lifetime).

The *PC1D for Matlab* program has implemented a range of calculations used both to calculate additional results from PC1D output data and for determining PC1D input parameters based on a list of secondary parameters. A few simulation examples are given in section 3 below, but the rest of calculations are not described in detail in this paper. A list of the different calculations and secondary parameters that are currently included is however shown in Table 1. For a complete and updated description of the different calculations that are included in the program and the necessary settings for each of them, please see the documentation file which is provided at the download page.

In addition to this, the *PC1D for Matlab* program has capabilities for importing external (experimental) data for direct comparison with the simulated results. We have also implemented an Nelder-Mead optimization algorithm available through the *fminsearch()* function in the Mathworks Optimization Toolbox [3], which can be used to fit simulated data to an external curve or to optimize the results with respect to e.g. the cell efficiency. Any set of primary or secondary parameters may be set as fitting variables.

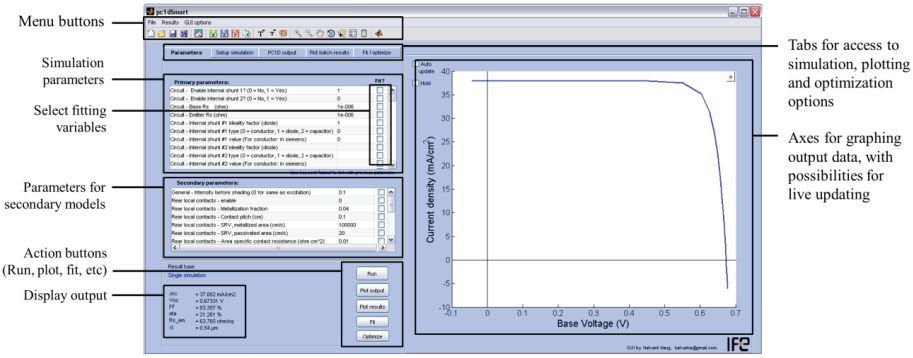

Fig.2. Illustration of the graphical user interface at the time of writing. Several relevant features of the program are indicated.

Table 1. List of different result values that are calculated in the *PC1D for Matlab* program and the parameters of the secondary models used to set input values for PC1D simulations. Note that changes and additions may occur in future updates of the program.

Results calculated from PC1D output data		**Secondary parameters used for**
Scalar values	**Vector data**	**setting PC1D input data**
Short circuit current	Current density	Front side metallization grid:
Open circuit voltage	Power density	Contact finger spacing
Fill factor	Global AM1.5 solar spectrum	Contact finger width
Efficiency	Reflectance times solar spectrum	Contact finger thickness
Emitter sheet resistance	EQE times solar spectrum	Contact finger length
Emitter junction depth	IQE times solar spectrum	Busbar width
Steady state carrier lifetime	Excess minority carrier density	Busbar thickness
Steady state generation rate	QSS carrier lifetime	Busbar length
Steady state injection level	Transient carrier lifetime	Metal resistivity
Generalized lifetime at $\Delta n = 10^{15}$ cm^{-3}	Generalized carrier lifetime	Area specific contact resistance
Sinton optical constant		Local rear contacts:
Integrated weighted reflectance		SRV of metallized area
		SRV of passivated area
		Metallization fraction
		Contact pitch
		Area specific contact resistance

3. Simulation examples

In this section we present different examples of simulations that are possible with the command-line version of PC1D and the accompanying graphical user interface. Note that all these simulations can be performed in a both fast and understandable manner on a standard personal computer. The estimated time used for setting up the simulation in the user interface by a trained user and the approximate simulation time are indicated in the figure captions for each case.

3.1. Optimization of a double layer antireflection coating

In order to illustrate the potential for large scale batch simulations in the *PC1D for Matlab* program, we have simulated a planar Si solar cell while changing the layer thicknesses in a double layer antireflection coating (ARC) placed on a planar Si surface. The two thicknesses were varied between 0 and 150 nm in steps of 2 nm, giving a 76x76 array of result data, with all the characteristics of the I-V curve saved at each point. A constant refractive index of 2.5 and 1.5 was used for the innermost and outermost layer, respectively. Fig. 3 shows a colour map of the short circuit current of the simulated cell, plotted within the *PC1D for Matlab* program. To illustrate the use of the scripted PC1D simulations in an optimization process, we tracked the steps of the optimization algorithm described above and plotted it over the colour map in Fig. 3. The optimization function was used to find the maximum short circuit current with the two layer thicknesses set as free fitting variables.

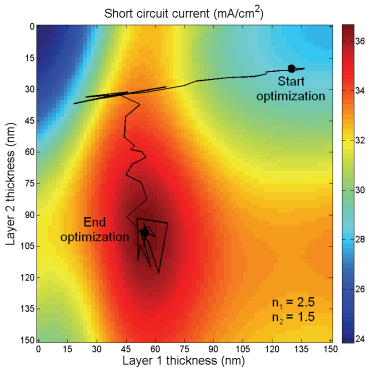

Fig. 3. 2D colour map showing the short circuit current density of a Si solar cell as a function of the two layer thicknesses in a double layer ARC. (5776 points. Setup time: ~30 s. Simulation time: ~10 min). The black lines illustrate the steps of an optimization algorithm used to find the optimal parameters. (Setup time: ~30 s. Simulation time: ~45 s).

3.2. Simulation of a quasi-steady state photoconductance measurement

Quasi-steady state photoconductance (QSS-PC) is a technique commonly used to measure the effective minority carrier lifetime of a Si wafer [4]. The measurement process can be simulated using PC1D by calculating the time dependency of the excess carrier density Δn and optical generation rate G in a passivated Si wafer. For the calculations shown in this paper, the spectral distribution and time-varying intensity of the flash that is mounted in the Sinton WCT-100 measurement setup were used as the

excitation source. The generalized expression for the effective carrier lifetime τ_{eff} can then be calculated as [5]

$$\tau_{\text{eff}} = \frac{\Delta n(t)}{G(t) - \frac{d\Delta n(t)}{dt}}. \quad (1)$$

When the time-dependent cumulative excess conductivity and cumulative photogeneration have been chosen as output values, the program automatically calculates the effective lifetime following both the quasi-steady state, transient and generalized equations described in Ref. [5]. It therafter lets the user plot them as a function of the excess carrier density, resulting in the familiar curves of the effective lifetime vs injection level that are obtained from a QSS-PC measurement. The program will also store the effective lifetime value corresponding to an injection level of $\Delta n = 10^{15}$ cm^{-3}, which can for instance be plotted as a function of one of the variable input parameters in a batch simulation. Fig. 4 (a) shows the effective lifetime vs excess minority carrier density with varying bulk doping concentration N_A.

Because the effective carrier lifetime is calculated from the photogeneration rate in the bulk of the sample, it is important to know the sample thickness and the optical properties of the sample surfaces when performing a QSS-PC measurement. These properties are described in the spreadsheet controlling the measurement as a so-called optical constant, which is defined as the ratio between the photogenerated current in the sample and a reference value of 38 mA/cm^2. This value depends both on the wafer thickness and the front side reflectance integrated over the spectral distribution of the excitation source, and is generally not straight-forward to calculate. The optical constant is another example of a useful additional output value that is automatically calculated in the *PC1D for Matlab* program when the correct output data is chosen. Fig. 4 (b) shows the optical constant for a polished Si wafer as function of the thickness of a coating layer with constant refractive index of 2.1 for different wafer thicknesses. The results where obtained by running a single, two-parameter variation from the user interface.

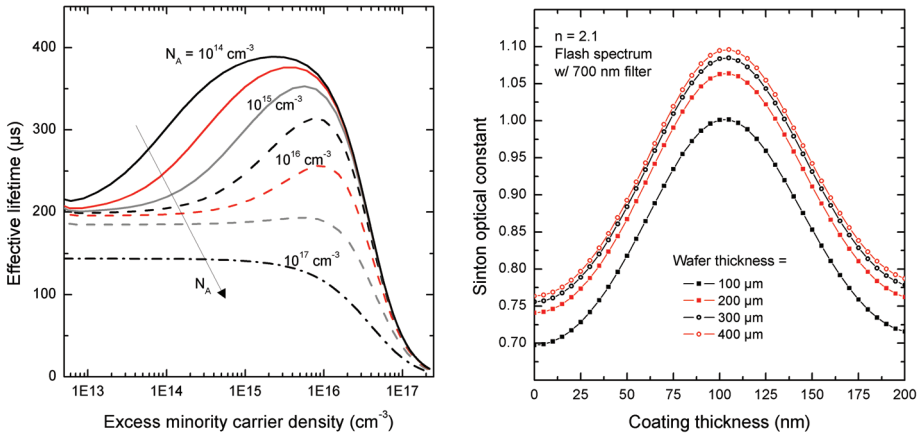

Fig.4.(a) Simulated QSS-PC curves (effective carrier lifetime as a function of excess carrier density) for different acceptor doping levels. Parameters used for the simulations: Bulk lifetime SRH parameters: $\tau_{0n} = \tau_{0p} = 200$ µs, $S_{0n} = S_{0p} = 1$ cm/s on both surfaces, midgap defect levels. The effective lifetime was calculated using the generalized formula described in Ref. [5]. (Setup time: ~30 s. Simulation time: ~30 s). (b) The optical constant (used in a Sinton QSS-PC measurement [3]) for a polished wafer as a function of the thickness of the coating layer for different wafer thicknesses. (Setup time: ~30 s. Simulation time: ~1 min).

3.3. Si solar cell with passivated rear surface and local contacts.

In the last section we showed examples of how additional calculations based on PC1D output data have been implemented into the *PC1D for Matlab* program. Another possibility is to include calculations in the beginning of the process, determining parameters which are then used as input for the PC1D calculations. One example of a case where this approach is relevant is when calculating the rear side surface recombination velocity (SRV) of a passivated Si solar cell with local point contacts. This is normally achieved with Fischer's equation, giving the rear side SRV as [6]

$$S_{eff} = \frac{D}{W}\left(\frac{p}{2W\sqrt{\pi f}}\arctan\left(\frac{2W}{p}\sqrt{\frac{\pi}{f}}\right) - e^{-\frac{W}{p}} + \frac{D}{fWS_{met}}\right)^{-1} + \frac{S_{pass}}{1-f} \qquad (2)$$

where D is the minority carrier diffusion constant, W is the wafer thickness, p is the pitch between the contacts, f is the metallization fraction and S_{met} and S_{pass} are the SRVs of the metallized and passivated regions, respectively. These and other parameters used for such secondary models are shown in a separate list in the GUI (see Fig. 2), and can be edited and used for parameter variations and fitting in the same way as the normal PC1D parameters. The GUI also allows for setting a value for the specific contact resistance, which together with the metallization fraction and the cell area is used to determine the total internal series resistance of the base contact. Fig. 5 shows the simulated cell efficiency of a Si solar cell as a function of the rear side metallization fraction for different values of the SRV of the metallized area. For the lowest metallization fractions the cell efficiency drops quickly because of series resistance in the contacts. The efficiency is also reduced at higher metallization fractions for large values of S_{met} caused by the increase in SRV at the rear surface, resulting in a peak in efficiency at approximately 3 % for this particular case.

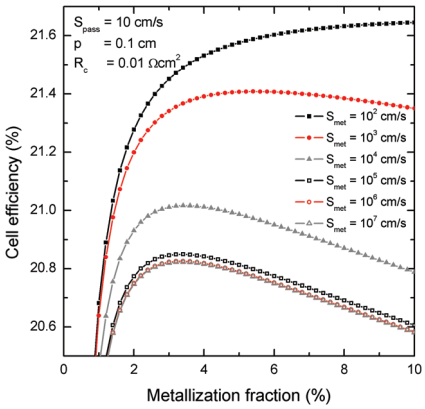

Fig. 5. Simulated cell efficiency of a PERC-type Si solar cell as a function of the rear side metallization fraction for different values of the SRV of the metallized area S_{met}. Values for the SRV of the passivated area S_{pass}, the contact pitch p and the area-specific contact resistance R_c are indicated. (Setup time: ~30 s. Simulation time: ~1 min).

4. Program availability and documentation

The files for the graphical user interface, the command line version of PC1D and the associated conversion programs can be downloaded free of charge from the following URL:

www.ife.no/en/ife/departments/solar_energy/downloads.

The *cmd-pc1d* program runs on 32-bit and 64-bit windows, but versions for the Mac and Linux operating systems may be added in the future. The standalone version of *PC1D for Matlab* program is currently only compiled for 64-bit Windows, and requires the installation of a library of Matlab files called *Matlab Compiler Runtime,* which can be downloaded and installed free of charge (see download page for details).

For more information regarding the various options and calculations implemented in the *PC1D for Matlab* program, readers are referred to the documentation file shown on the download page. New updates will be documented in a separate changelog which can be found at the same location. Please cite this conference paper in addition to the original PC1D publications if you plan to use the software in published material.

5. Summary

In this paper we have presented a modification of PC1D to create a version called *cmd-pc1d* which can be run from a command line. We also present a new graphical user interface for the program, which includes many new features for multivariable analysis, advanced plotting, optimization, fitting to experimental data and implementing additional models and parameters not available in the original PC1D program. The new GUI can be run as a standalone executable without the need for any paid license files, and can be downloaded free of charge.

Acknowledgements

This work has been funded by the Research Council of Norway through the project "Thin and highly efficient silicon-based solar cells incorporating nanostructures," NFR Project No. 181884/S1.

References

[1] D. A. Clugston and P. A. Basore, “PC1D version 5: 32-bit solar cell modeling on personal computers”, Conference Record of the 26th IEEE Photovoltaic Specialists Conference, 207–210, (1997).
[2] The Mathworks, Inc, “MATLAB 2012b”, Natick, Massachusetts, United States.
[3] The Mathworks, Inc, “Optimization Toolbox User’s Guide, 2009”. [Online]. http://www.mathworks.se/help/toolbox/optim/
[4] R. A. Sinton, A. Cuevas, and M. Stuckings, “Quasi-Steady-State PhotoConductance, A new method for solar cell material and device characterization”, Conference Record of the 25th IEEE Photovoltaic Specialists Conference, p. 457 (1996).
[5] H. Nagel, C. Berge, and A. G. Aberle. “Generalized analysis of quasi-steady-state and quasi-transient measurements of carrier lifetimes in semiconductors”, Journal of Applied Physics 86 (11), 6218–6221 (1999).
[6] B. Fischer, “Loss analysis of crystalline silicon solar cells using photoconductance and quantum efficiency measurements”, Dissertation, Universitaät Konstanz, Konstanz, (2003).